UNIVERSITÀ DEGLI STUDI DI PADOVA

FACOLTÀ DI SCIENZE MM.FF.NN.

DIPARTIMENTO DI FISICA

Dottorato di Ricerca in Fisica

XVII Ciclo

The GLAST mission: assessing radiation hardness and performances of GLAST LAT tracker electronics

Coordinatore: Prof. ATTILIO STELLA

Supervisore: Prof. GIOVANNI BUSETTO

Dottorando: RICCARDO RANDO

31 Dicembre 2004

Acknowledgements

I am greatly indebted to Giovanni Busetto, Dario Bisello and Antonio Saggion for giving me the opportunity to carry on this stimulating work and for the support they gave me during this three years we worked together. I am very grateful to all my coworkers at the INFN section of Padova for their help and support. In particular I thank Jeffery Wyss, Maurizio Loreti, Andrea Candelori, Tommaso Dorigo, Nicola Bacchetta, Patrizia Azzi, Denis Bastieri, Alexander Kaminski, Devis Pantano, Mario Tessaro... My gratitude to Silvano Lora and to all the CNR-ISOF group at the national Laboratories of Legnaro for their help.

I wish to express my warmest thanks to the GLAST groups in SLAC and SCIPP for the many chances thay gave me and for the hospitality I received. In particular my thanks to Hartmut F.-W. Sadrozinski, Robert P. Johnson, Leonid Sapozhnikov, Mutsumi Sugizaki, Marcus Ziegler and Wilko Kroeger. Many, many thanks to the SCIPP summer students I worked with, Andrea Bangert and John Wray: I hope you found your stay in Padova as nice and profitable as we did.

If I were to name here all the people of the GLAST Italian collaboration I owe thanks to, the list would cover most of this page. I can only name some of them here, like Francesco Longo, Riccardo Giannitrapani, Alessandro De Angelis, Claudia Cecchi, Monica Brigida, Francesco Giordano, Silvia Rainò, Francesco Gargano...

Special thanks to the friends I met in Pisa, for an extremely profitable yet pleasing experience: Ronaldo Bellazzini, Luca Baldini, Luca Latronico, Nicola Omodei, Carmelo Sgrò, Massimiliano Razzano...

Thanks to my young colleagues in Padova for their friendship and support: Piero Giubilato, Marco Dal Maschio, Giorgio Cortiana, Saverio Da Ronco, Serena Mattiazzo...

To my family and friends, for so much, my love.

Introduction

During the last decade, γ-ray astrophysics has experienced a period of great achievements, with the results of several satellite-borne experiments shedding light on some of the most intriguing mysteries of the high energy universe: the first-ever complete sky survey has been completed by the CGRO observatory, a "standard model" unifies the structure of active galactic nuclei, and the puzzles of the origin of cosmic rays and of gamma-ray bursts are possibly close to being solved. New missions are prompted by this exciting moment, and the GLAST experiment is expected to give a major contribution in this exciting field.

Operation in space forces a certain number of strict requirements on both performances and robustness. The INFN of Padova has a great expertise in characterization and radiation testing of semiconductor devices, and state-of-the-art irradiation facilities are available at the INFN National Laboratories in Legnaro. Our group established an intense collaboration with SLAC and the Santa Cruz Institute of Particle Physics, leading to the results described here.

INFN Pisa has the responsibility of assembling and testing the LAT tracker. I took part in these activities and tested the flight parts that are being used in the construction of the telescope, and I had the opportunity of see the first events ever, taken with a few flight trays put in a stack. A short review of the tests I performed in Pisa is presented.

As the telescope parts are being assembled, the first simulated data are being released and are ready for event analysis. This is the moment to build the expertise that will be needed to handle the real data produced by the telescope; on the other hand it is necessary to make sure the simulated performances are correct. I participate to the activities being carried out in Padova, among which are the validation of the simulated data and the fine tuning of particle ID and background rejection routines. A brief introduction to the work in progress is given.

Introduzione

Durante l'ultimo decennio, l'astrofisica gamma ha vissuto un periodo di grandi successi, e i risultati di diversi esperimenti su satellite hanno fatto luce su alcuni dei più affascinanti misteri dell'universo ad alte energie: il primo catalogo completo delle sorgenti γ celesti è stato completato dall'osservatorio CGRO, un "modello" standard unifica la struttura dei nuclei galattici attivi, e i misteri sull'origine dei raggi cosmici e sui gamma-ray bursts sono forse prossimi ad una soluzione. La preparazione di nuove missioni è stata stimolata da questa favorevole condizione, e l'esperimento GLAST potrà dare un contributo significativo nel campo.

La collocazione nello spazio impone un certo numero di stringenti requisiti su prestazioni e robustezza. Il nostro gruppo dell'INFN sezione di Padova è entrato a far parte della collaborazione GLAST in virtù dell'esperienza che può mettere a disposizione nel campo della caratterizzazione degli effetti della radiazione su dispositivi a semiconduttore, grazie anche alle strutture disponibili presso i Laboratori nazionali di Legnaro. Un'intensa collaborazione con SLAC e il Santa Cruz Institute of Particle Physics ha portato ai risultati qui descritti.

L'INFN sezione di Pisa ha la responsabilità dell'assemblaggio e della caratterizzazione del tracciatore del LAT. Ho potuto prendere parte a queste attività e testare le parti di volo che verranno usate nella costruzione del telescopio; inoltre ho avuto l'opportunità di partecipare alla presa dei primi dati in assoluto, osservati con alcuni tray di volo disposti in configurazione di telescopio. Le attività di test da me svolte a Pisa sono qui riassunte.

In parallelo all'assemblaggio delle prime parti del telescopio, i primi dati simulati sono pronti per l'analisi. Questo è il momento di consolidare l'esperienza che sarà necessaria per trattare i dati delle osservazioni del LAT; d'alto canto, è necessario assicurare che le prestazioni simulate sono corrette. Le attività in corso di svolgimento a Padova, descritte in un capitolo dedicato, includono la validazione dei dati simulati e l'ottimizzazione degli algoritmi di identificazione del segnale e della reiezione del fondo.

1 Energetic astrophysical sources

Before describing in detail the GLAST Large Area Telescope, a brief introduction to the scientific topics it will investigate is necessary. In this chapter astrophysical sources of energetic γ radiation are described. An introduction to physical processes involved in the production of γ rays and a quick summary of the γ interaction processes can be found in App. 1. For each topic the requirements the GLAST mission must meet to provide new insights are detailed; data are taken from [1].

1.1 Gamma pulsars

Periodic electromagnetic signals from collapsed objects are known since 1967, when radio signals were received at the recently built Cambridge radio telescope. The following year such pulsating sources were identified as rotating, magnetized neutron stars [2] [3].

Once the nuclear fuel that sustains their existence is exhausted, lighter stars evolve into a new, stable configuration, in which the burnt, ferrous core is sustained by the pressure of a degenerate electron gas. Massive stars follow a more troubled path: the degenerate electron sea is not able to sustain a core of more than 1.44 solar masses. If the collapsing mass is above this limit but below 3.6 solar masses a neutron core forms when protons and electrons recombine in inverse β-decay, until a stable degenerate Fermi gas of neutrons is formed. If the collapsing mass is above 3.6 solar masses, even the pressure of the degenerate neutron gas is not enough to stop the core collapse, and a *black hole* forms. It must be considered that when a compact core is formed a huge amount of energy is emitted in the form of gravitational waves, plus neutrinos and a detonation front as a consequence of the violent nuclear reactions accompanying the sudden increase in pressure and temperature. Thus, the star outer layers are blown away and a consistent fraction of the stellar mass will not take part in the final collapse: the stars that eventually become neutron stars are thought to start out with about 15 to 30 solar masses. These numbers depend strongly on the parameters used in supernova simulations, but for initial masses much less than 15 solar masses the star becomes a white dwarf, whereas for initial masses much higher than 30 solar masses a black hole is the final result.

Neutron stars have radii of about 10 km and densities of the order of 10^{15} g/cm^3. Conservation of angular momentum leads to an increase in angular speed by a factor 10^{10}, and the conservation of magnetic flux[(1)] increases the typical stellar magnetic field ($\sim 10^2$ G) to values of the order of $\sim 10^{12}$ G. A rotating, magnetized neutron star emits therefore huge amounts of electromagnetic radiation. At the star surface the induced electric fields are by far greater than the gravitational forces, and charges are thus ejected from the surface and fill the star co-rotating magnetosphere. At a distance $r = c/\omega$ from the axis of rotation particles and fields would have to co-rotate with the speed of light: relativistic distortions force open the field lines crossing this region, and particles moving along them

(1) – the interior of a star is a fully conducting medium

are free to escape. For a review of pulsar emission models see [4] [5] [6]. The motion of charged particles along the pulsar magnetic field lines give rise to γ production by means of magnetic bremsstrahlung, and where the fields are more intense, exotic processes like magnetic pair production and photon splitting occur. All these processes present strong tell-tale signs that should be found in the pulsar γ spectrum.

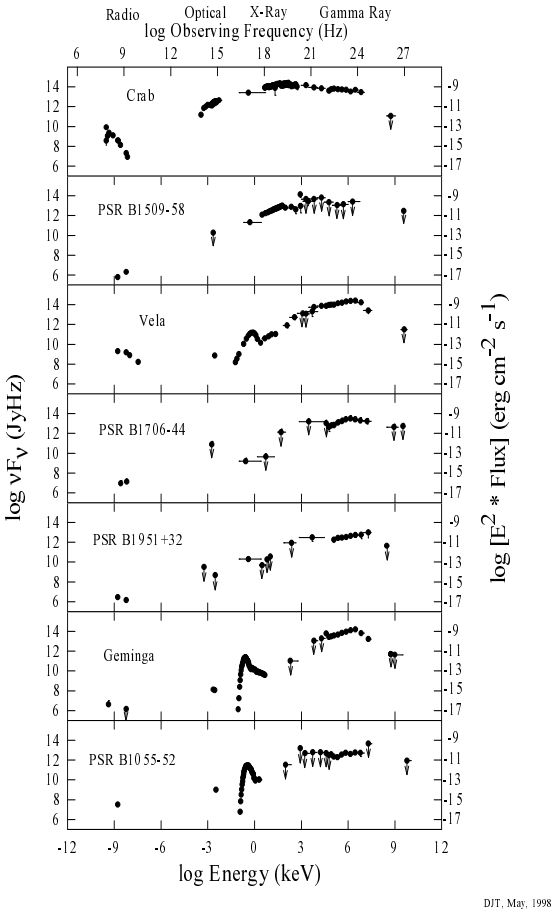

Fig. 1.1 - Multi-wavelength light spectra of known gamma-ray pulsars, from [7].

Before the CGRO mission, only two pulsars were known at γ energies: Crab and Vela, detected by SAS-II and COS-B (see Chap. 2). A third source was found near Crab, but no counterpart at other wavelengths was found. Only joint measurements by CGRO and the X-ray mission ROSAT allowed to establish the existence of a true high-energy pulsar, Geminga, by finding a faint X-ray counterpart. Today more than 30 pulsars are known at γ-ray energies; CGRO has taught the astrophysics community that the familiar pulsar radio emission is a fraction of the bolometric luminosity, as the power spectrum peaks in the GeV range for many young pulsars. An order of magnitude increase in the number of detected γ-ray pulsars is essential for our understanding of the basic structure of pulsar magnetospheres and identify the sites and nature of pulsar particle acceleration.

To identify a γ source as a pulsar, the period must be measured. Periodic searches in the γ regime are possible only if the source is strong (above $\sim$ 100 photons per day); up to now only Geminga was strong enough for this analysis, when viewed by EGRET. Forthcoming observations by new observatories like GLAST are expected to substantially

increase this figure.

In current models for pulsar emission several problems and uncertainties continue to persist. Multi-wavelength analysis is the key instrument to investigate the emission mechanisms. In particular, spectral hardness of the pulsar emission as a function of rotational phase is a strong tool to investigate different models; again the efficiency of this kind of test depends on the number of collected photons and on the energy resolution.

A summary of the requirements for the GLAST pulsar investigation are the following:

- a good effective area is required to have a substantial increase in the number of collected photons;
- a spectral resolution (of $\sim$10%) is needed, especially in the energy range from 100 MeV to 10 GeV where several pulsars exhibit a spectral break of uncertain origin;
- absolute timing knowledge ($\sim \mu$s) and absolute position knowledge are needed to facilitate searches for pulsations from millisecond pulsars and to characterize the pulse profiles of detected pulsars.

1.2 Active Galactic Nuclei (AGNs)

In contrast with the images of normal galaxies, active galaxies show bright, star-like nuclei. Their optical spectra show broadened emission lines instead of absorption lines; luminosity maximums appear in IR, UV, X or γ bands, and are often dominated by non-thermal emission, while for a normal galaxy most of the released energy lies in the optical band, being simply the sum of the light coming from the stars it contains. Active galaxies are extremely variable: their emissions change significantly in timescales of the order of days or faster. Today about 70 AGNs are identified.

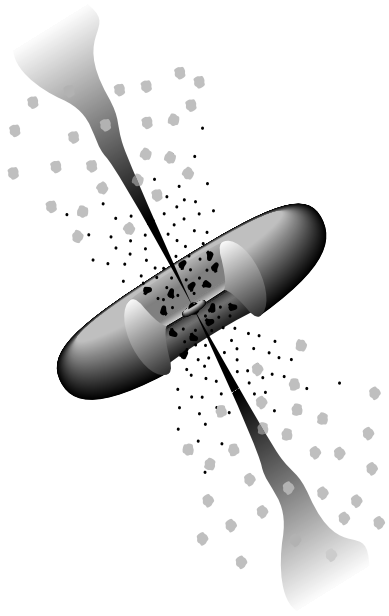

Fig. 1.2 - Artist rendition of an AGN: in the center the black hole, surrounded by the accretion disk, around it the warped torus.

AGNs have been shown to vary on timescales as short as 15-30 minutes (e.g. Mkn 421). This rapid variability places a constraint on the AGN engine: for a typical variation scale of 1 day, the emission region must have roughly the size of the solar system. The emitted

energy can be as high as 10 times the energy output of a bright normal galaxy, that is a luminosity of the order of 10^{12} suns. This scenario requires an extremely effective energy source. The most efficient process known is the release of gravitational energy in a deep gravitational well; supermassive ($> 10^6\ M_\odot$) black holes are postulated, with large mass accretion rates

$$L_{\rm acc} = \epsilon \cdot \frac{dm}{dt} \cdot c^2 \tag{1.2.1}$$

where the efficiency ϵ is about 10% (by comparison, nuclear fusion reaches only $\sim 0.7\%$).

Since their discovery, the origin of AGN emission has been widely discussed. Beamed emission had been proposed to reconcile the γ flux intensity with the source small radius and hence density and optical thickness. Superluminal motion was observed, and in some cases jets can actually be resolved in AGN images.

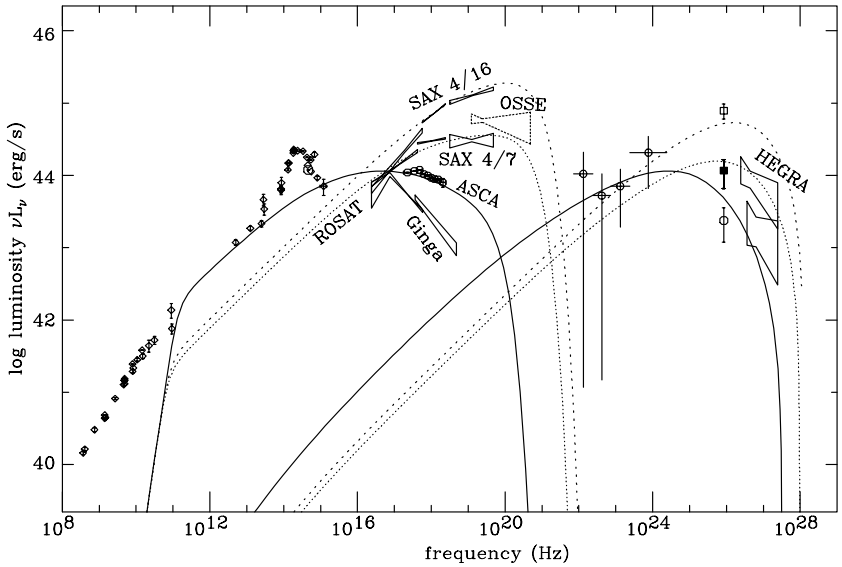

Fig. 1.3 - Multi-wavelength spectrum of Mkr501, from [8].

Detailed models have been formulated to explain the broadband emission, involving synchrotron and inverse-Compton radiation in outflowing plasma blobs or shocked jet regions. To explain the γ-ray emission two models have been proposed, with either leptons or hadrons as the primary accelerated particles. In leptonic models, relativistic leptons scatter soft photons to γ-ray energies via the inverse Compton process. Different explanations of the soft photons origins were made, with strong repercussions on the predicted energy spectra. In hadronic models, protons transfer energy to photons via pion production. Secondary pairs lose energy due to synchrotron emission, and pions decay into γ photons and additional high-energy electrons and positrons, which in turn suffer synchrotron losses.

An increase in energy range and spectral sensitivity is required for further progress in this field. Studies of spectral evolution during gamma-ray flares and measurements of spectral breaks at both low and high energies can give important clues to particle acceleration mechanisms and the location of emission regions. Overlap and good intercalibration with other ground-based, high-energy gamma-ray Čerenkov telescopes (100 GeV- TeV range) will be important for definitive studies of spectral cutoffs.

Requirements for the GLAST AGN investigation are the following:

- a broad energy response (from 20 MeV to at least 300 GeV) to explore the low-energy spectrum where many AGN have peak emission, to measure high-energy cutoffs, and to overlap with ground-based gamma-ray observations;
- required spectral resolution is 10% or better (100 MeV — 10 GeV) to facilitate studies of spectral breaks at both low and high energies;
- a wide effective area (several thousands cm^2) over the central part of the photon energy range allows for variability studies of bright sources down to the sub-day timescales;
- a field of view at least 2 steradians allows for a significant sky coverage to monitor large numbers of AGN and their variability;
- a greatly improved flux sensitivity (better than 10^{-8} cm^{-2} s^{-1}) allows to measure the AGN flux distribution (logN-logS function) including fainter sources;
- a mission life of many years allows long-term studies of AGN variability.

1.3 Gamma Ray Bursts (GRBs)

The first γ-ray bursts [9] were discovered in 1967 when satellites of the Vela series, intended to monitor violations of the nuclear test ban treaty, measured unexplainable increases in the γ count rate. The source was proven to be extra-solar by analyzing the arrival times of the signals to the different satellites. A series of dedicated instruments at the end of the 1970s and at the beginning of the 1980s successfully located many strong GRBs with errors less than 1 arc min, with triangulation techniques. The first image of a single GRB with an accuracy of $\sim 1^\circ$ was obtained from COMPTEL in 1992. CGRO instruments measured more than 2000 events with errors as low as 1° from 1991 to 1998.

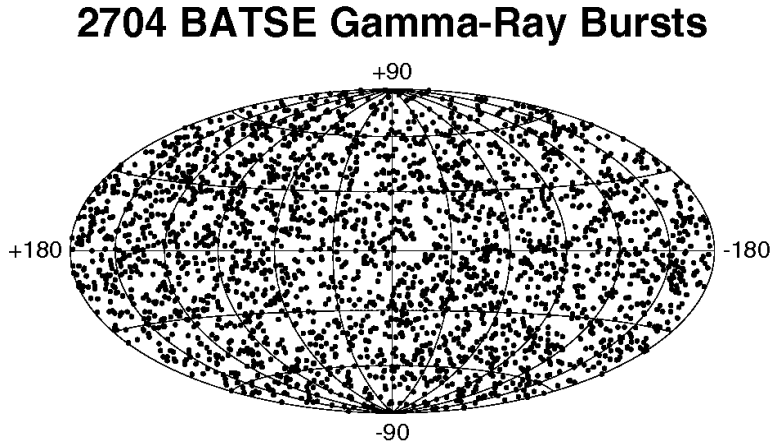

Fig. 1.4 - Sky map in galactic coordinates of all 2704 GRBs detected by BATSE in a 9 year mission aboard CGRO (see Sect. 2.7).

One of the major problems in GRB analysis is given by the variability of their time profiles: while some bursts show spikes lasting less than a ms, others exhibit structures lasting as much as 1000 s. The time evolution of a burst correlates with other features, such as hardness and fluence; in general longer bursts are softer and shorter bursts are harder.

Many models have been proposed to describe GRBs, and each time new data were available some were ruled out and others were proposed. The discovery of their isotropic but inhomogeneous (time-limited) distribution ruled out galactic disk models, while the discovery of optical counterparts with red-shifted absorption lines set them at cosmological distances, ruling out heliocentric and galactic halo models. Currently favored models are *cosmic fireball* models [10] [11] [12]; nonetheless they present many uncertain points and many questions need new insights by next generation observatories.

In this model a blast wave forms and its evolution, rather independent from its origin, gives rise to γ emission. Independently of the specific model, the initial blast wave interacts with other outflowing material, with a previous shell, with the interstellar medium or with the stellar wind, producing γ rays due to synchrotron emission and, to a certain extent, to inverse Compton. In the subsequent cooling phase, the decelerated blast can give rise to the observed afterglows at greater wavelengths.

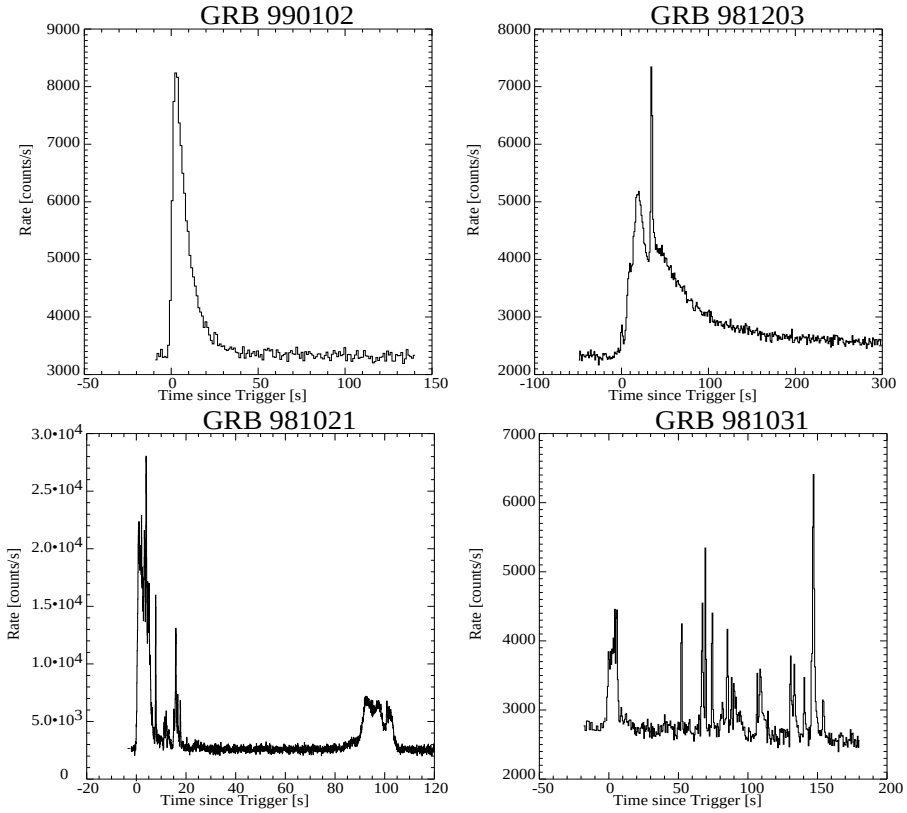

Fig. 1.5 - Different GRB time profiles: smooth single-pulsed, smooth with peaks, multiple and chaotic.

New insights are expected from the next γ observatories that will glimpse at the inner engine providing energy to GRBs. In particular the coordinate multi-wavelength observation of GRBs from space observatories and from ground-based Čerenkov telescopes look extremely promising.

Requirements on the GRB capabilities are split in GLAST between the Glast Burst Monitor (GBM) and the Large Area Telescope (LAT). The burst monitor will be used as a GRB alert:

- a wide field of view (8 sr) is needed to monitor all the sky visible at any time from Earth orbit.

- the energy range must cover the classical gamma-ray band where most of the burst photons are emitted (from 10 keV to several 10s MeV)
- the ability is needed to quickly (< 5 s) recognize and localize GRBs for the purpose of notifying other observers and to re-point the spacecraft, allowing the LAT to work in pointing mode;

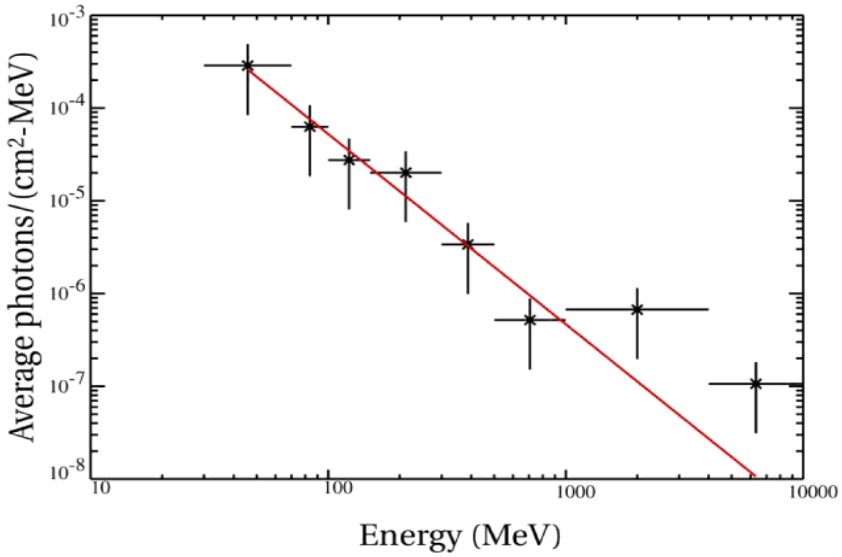

Fig. 1.6 - Average spectrum measured by EGRET for 4 bursts (45 photons above 30 MeV, 4 above 1 GeV), from [13].

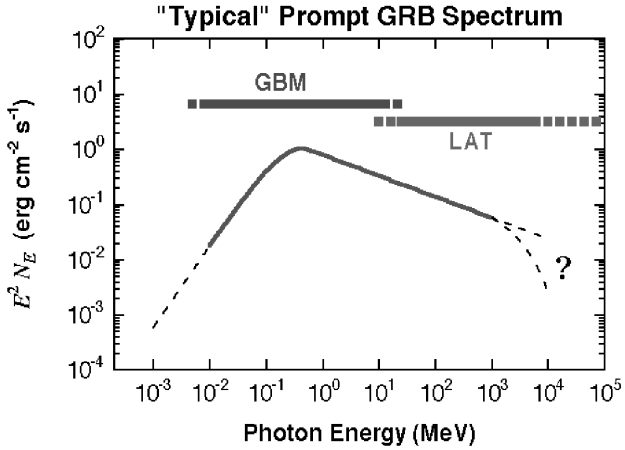

Fig. 1.7 - Energy coverage of GLAST LAT and GBM: the range of sensitivity of each instrument is shown on top of a sample GRB spectrum; a possible spectral break within the LAT range is shown.

When pointing towards a GRB, the LAT can give new insights on GRB mechanisms if the following constraints are met:

- a wide (2 sr) field of view is needed to monitor a substantial fraction of the sky at any time;
- spectral resolution must be better than $\sim$ 20%, especially at energies above 1 GeV, for sensitive spectral studies and searches for spectral breaks;

- the dead time per event must be small (< 100 μs) to determine correlations between low energy and high energy gamma-ray burst time structure;

1.4 Cosmic rays

Cosmic rays were discovered noticing that electroscopes in laboratories steadily measured a deposition of charge. This behavior was explained as due to a flux of ionizing particles coming from the Earth; yet, no amount of shielding seemed enough to stop this radiation from inexorably discharging any electroscope. In 1912 Victor Hess decided to measure the decrease of the radiation density as a function of altitude with a balloon experiment, but he found that above 1 km his electroscopes discharged even more rapidly the more they ascended to great heights, opposite from what was expected. He attributed this to a source of extremely energetic ionizing radiation entering the atmosphere from above, and in 1936 was awarded the Nobel prize for his discovery. For some time it was believed that the radiation was electromagnetic in nature (hence the name cosmic "rays"); however, during the 1930's it was found that most cosmic rays must be electrically charged, as they are affected by the Earth's magnetic field. Cosmic rays include essentially all of the elements in the periodic table; about 89% of the nuclei are hydrogen (protons), 10% helium, and about 1% heavier elements. The common heavier elements (such as carbon, oxygen, magnesium, silicon, and iron) are present in about the same relative abundances as in the solar system, but there are important differences in elemental and isotopic composition that provide information on the origin and history of galactic cosmic rays. For example there is a significant overabundance of the rare elements Li, Be, and B produced when heavier cosmic rays such as carbon, nitrogen, and oxygen fragment into lighter nuclei during collisions with the interstellar gas. The isotope ^{22}Ne is also overabundant, showing that the nucleosynthesis of cosmic rays and solar system material have differed. Electrons constitute about 1% of galactic cosmic rays.

The cosmic ray spectrum is fairly well described by a broken power law. The spectrum steepens around 3×10^6 GeV and flattens around 3×10^9 GeV. Most galactic cosmic rays have energies between 100 MeV and 10 GeV. The number of cosmic rays with energies beyond 1 GeV decreases by about a factor of 50 for every factor of 10 increase in energy; the highest energy cosmic rays measured to date have had more than 10^{11} GeV[(2)]. A successful model must produce the right number of particles as a function of energy; in other words, the spectrum constrains models of cosmic ray production. Only a small fraction (0.1%) of cosmic rays are photons (in the form of gamma-rays). Yet, these γ-ray photons are important when trying to find the origin of cosmic rays since they arrive at the Earth undeflected by the galactic magnetic field.

From the 1930s to the 1950s, before man-made particle accelerators reached very high energies, cosmic rays served as a source of particles for high energy physics investigations, and led to the discovery of subatomic particles that included positrons, muons, pions and kaons. Although these applications continue, since the dawn of the space age the main focus of cosmic ray research has been directed towards astrophysical investigations on the origin of cosmic rays, how they get accelerated to such energies, what role they play in the dynamics of the Galaxy, and on what their composition tells us about matter from

(2) – equivalent to the kinetic energy of a tennis ball traveling at approximately 250 km/h!

outside the solar system.

Particle acceleration at *supernova remnant* (SNR) shock waves is regarded as the most probable mechanism for providing galactic cosmic rays at energies below 10^{15} eV. The recent detections of non-thermal X-ray synchrotron radiation from SN1006 [14] and Cas A [15], among others, support the hypothesis that at least galactic cosmic ray electrons are accelerated predominantly in SNR. To date, there is still no unambiguous proof that cosmic ray nucleons are similarly produced in SNR.

Whatever the nature of their sources, upon escape the cosmic ray nucleons would diffusively propagate through the interstellar medium, where they can be either directly measured or indirectly traced by means of γ ray observations. Recent observations made with the EGRET instrument on the Compton Gamma-Ray Observatory of the diffuse galactic γ ray emission reveal a spectrum which is incompatible with the assumption that the cosmic ray spectra measured locally hold throughout the Galaxy [16]. The spectrum observed with EGRET below 1 GeV is in accord with, and supports, the assumption that the cosmic ray spectra and the electron-to-proton ratio observed locally are uniform, however, the spectrum above 1 GeV, where the emission is supposedly dominated by π_0-decay, is harder than that derived from the local cosmic ray proton spectrum.

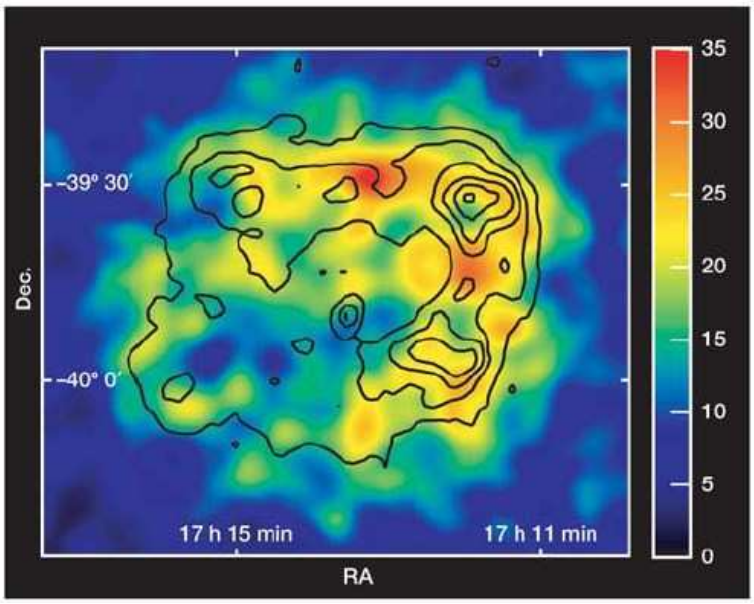

Fig. 1.8 - Gamma ray (>800 GeV) image of the SNR RX J1713.7 – 3946 obtained with HESSE with a partial array during construction; for comparison the superimposed contours show the X-ray surface brightness as seen by ASCA in the 1–3 keV range [14].

In [17] it is demonstrated that if the sources of cosmic rays are discrete, as are SNR, then the spectra of cosmic ray electrons would vary and the locally measured electron spectrum would not be representative for the electron spectra elsewhere in the Galaxy, which could be substantially harder than the local one. In particular the cosmic ray models rely on an electron injection spectrum with index 2.4 (chosen to fit the local electron flux up to 1 TeV), while following [17] an electron injection index of around 2.0 would be consistent with the expected fluctuations in the locally observable electron spectrum due to the Poisson fluctuations in the number of SNRs within a certain volume. Moreover this

would explain the above-mentioned gamma-ray excess above 1 GeV. An electron injection index of around 2 would also correspond to the average radio synchrotron spectrum of individual SNRs.

Recent results demonstrate that very high energy particles are accelerated in SNRs. For example Hesse observation of RX J1713.7 – 3946 [18] in the TeV range show that the spatially resolved remnant has a shell morphology similar to that seen in X-rays: in Fig. 1.8 Hesse image and X-ray observations made with the ASCA X-ray observatory are presented. Moreover, the energy spectrum indicates efficient acceleration of charged particles to energies beyond 100 TeV, consistent with current ideas of particle acceleration in young SNR shocks.

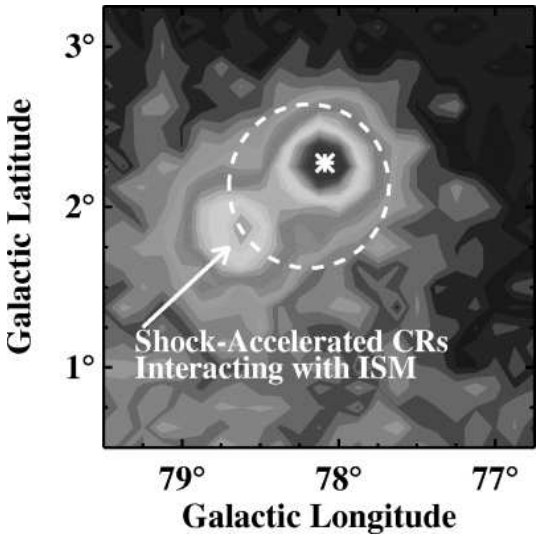

Fig. 1.9 - GLAST LAT simulated observation of γ Cygni [19].

GLAST observations of SNR objects can hopefully shed new light on this problem and solve a puzzle that has troubled the astrophysical community for the last 90 years. Requirements the LAT must meet are the following:

- an angular resolution better than 3.5° at 100 MeV at normal incidence, improving to better than 0.15° at 10 GeV, allows to map diffuse features and extended sources (EGRET resolution was $\sim 6°$ at 100 MeV, $\sim 0.5°$ at 10 GeV);
- a point source localization of less than an arcmin will allow the identification of supernova remnants by separating the emission of the shock wave.

1.5 Dark matter

Many evidences for dark matter come from astrophysical observations. The rotation curve of a typical spiral galaxy flattens or slowly rises beyond the optical radius which includes most of the galaxy luminosity. The flattening of the rotation curves indicates the presence of dark matter at large radii (about a few 10s kpc): a result which is confirmed, up to scales of 30 kpc, by the study of close binary systems.

Most dark matter candidates which arise in the standard model of particle physics are excluded by the present observational constraints, like, for instance, neutrinos. Supersymmetric (SUSY) extensions of the standard model lead to many more new DM candidates; presently, the most plausible SUSY dark matter candidate is the neutralino (χ), which is the lightest supersymmetric particle. The neutralino is stable and hence is a candidate

Big Bang relic. It is an electrically neutral Majorana fermion with a mass that can range from a few GeV to a few hundreds of TeV: a lower limit of about 30 GeV has been set by the LEP accelerator, while an upper limit of 340 TeV is favored theoretically.

Indirect detection experiments search for products of self-annihilation of neutralinos such as energetic leptons, hadrons, and also particles which would emerge in the follow-up hadronization and fragmentation processes. Thus, in addition to γ-ray lines generated through the annihilation channels $\chi\bar{\chi} \rightarrow \gamma\gamma$ and $\chi\bar{\chi} \rightarrow Z_0\gamma$, the annihilation of two neutralinos also produces a γ-ray continuum as a consequence of the neutral pion decay.

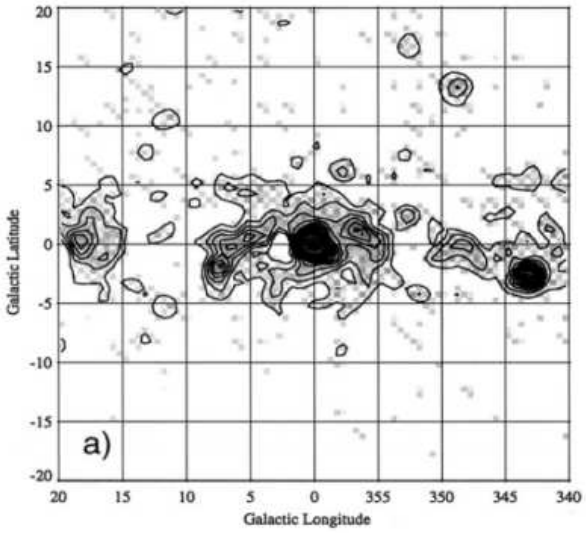

Fig. 1.10 - The galactic center, EGRET residual smoothed count maps and profiles at $E > 1$ GeV after subtraction of the model-predicted diffuse emission background [20].

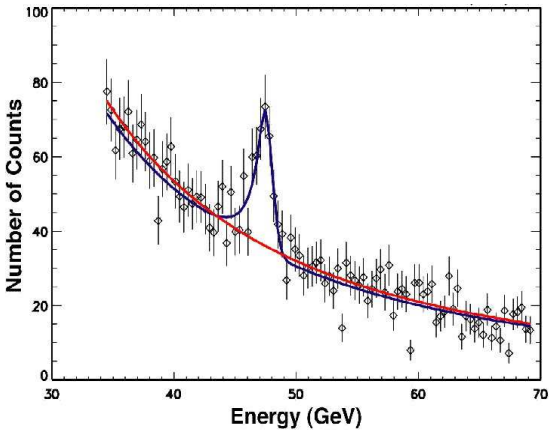

Fig. 1.11 - Gamma spectrum GLAST would observe for a 50 GeV neutralino decay from a 1-sr cone near the galactic center assuming a 1.5 % energy resolution [20].

EGRET has observed a strong excess of emission in the Galactic Center (GC) region, peaking at energies > 500 MeV in an error circle of 0.2° radius including the GC (see Fig. 1.10). The close coincidence of this excess with the GC direction and the fact that it is the strongest emission maximum within 15 degrees from the GC is taken as compelling evidence for the source's location. The angular extent of the excess appears only

marginally compatible with the signature expected for a single compact object. The emission therefore may stem from one or more compact objects [21].

In [20] it is speculated that, among other possible causes, this excess could be due to the continuum γ-ray spectrum from WIMP annihilation. With the dramatically improved angular resolution and effective area of the LAT, if there is an excess in the Galactic Center it should become both more localized and pronounced, while the energy resolution capabilities should allow one to identify the decay of weakly interacting particles [22] (see Fig. 1.11). Moreover, if the neutralino mass is small (less than 300 GeV), GLAST could detect a neutralino signature from other galaxies, like M87, above 1 GeV [23].

Requirements for the GLAST dark matter search are the following:

- broad energy range with response to at least 300 GeV to constrain cold dark matter candidates;
- spectral resolution of 2% at energies above 10 GeV to identify relatively narrow spectral lines.

2 Gamma Detection and Telescopes

In this chapter a short introduction to previous γ ray observatories is given. Before introducing the GLAST experiment and detailing the advancements it should bring in the field of high-energy astrophysics, a brief history of the most important space missions is presented. More specific information on the GLAST Large Area Telescope will be presented later in Chap. 3.

2.1 Gamma rays observation

Astronomy is currently performed over the entire range of the electromagnetic spectrum, covering approximately 20 orders of magnitude in frequency. Each frequency band gives information on the corresponding energy regime, often providing specific information that can hardly be obtained from the other parts of the spectrum.

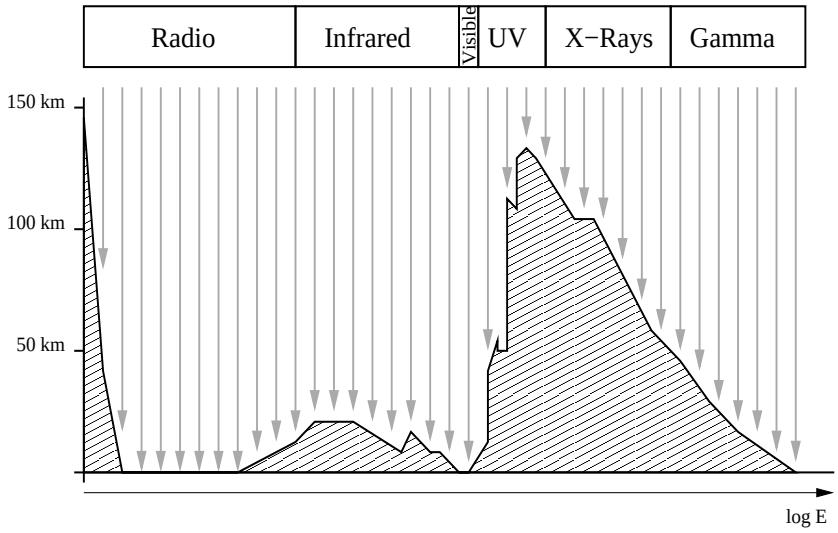

Fig. 2.1 - Schematic representation of Earth's atmospheric transparency as a function of the incoming photon energy. Photons of different energies coming from above the atmosphere can reach different altitudes before being absorbed.

The energy band of γ astronomy currently extends over more than seven orders of magnitude[(1)], from typically several hundreds of keV up to several TeV. It is not surprising therefore that a wide range of objects and phenomena can be studied.

Researchers face a major problem when dealing with detection of astronomical γ rays: although the latter are highly penetrating particles, and although the density of air is rather low (1.293 g/cm^3 at ambient pressure) the atmosphere is opaque in this energy range because its integrated density amounts to 1000 g/cm^3. In Fig. 2.1 a schematic plot of atmospheric stopping power is shown: only radio and visible photons can reach the

(1) – while being, by definition, open ended.

Earth's surface: at lower energies reflection cuts the radio band, while UV photons are absorbed by ozone, oxygen and nitrogen. IR photons are absorbed by CO_2 and H_2O.

For a 1 MeV γ photon the mass-attenuation coefficient for air is 0.00642 cm^2/g (see also Sect. 6.3) and thus the absorption probability is slightly greater than 99.8%. Consequently, γ astronomy below some hundreds GeV can only be performed with balloon- or satellite-borne telescopes.

Above some hundreds of GeV the atmosphere itself becomes the detecting medium, thanks to the possibility of observing the γ rays indirectly through the electromagnetic showers they produce. Great parabolic mirrors collect the Čerenkov light produced in these showers; such detectors are called Atmospheric Čerenkov Telescopes (ACT).

In the rest of this chapter we will focus on the satellite-borne experiments only. For more informations on ACTs see [24], [25].

2.2 Satellite-borne gamma astronomy

In x-ray telescopes the imaging capabilities are defined by the use of passive collimators: arrays of rectangular, hexagonal or circular tubes, whose walls are made by passive absorbers, define for each portion of the sensitive surface a corresponding field of view (usually several square degrees large). These collimators cannot be used in γ-ray telescopes due to the high penetrating power of the photons: too much matter would be required to stop γ photons, and, besides the obvious payload mass limitations, it would create a high particle background, thus reducing the detector signal/noise performance.

Since the early ages of γ-ray astronomy active collimation was employed: the geometrical arrangement of the sensitive components of the instrument defined the angle of acceptance. Inside this field of view (usually several degrees wide) no further spatial information was available. Yet, actively collimated telescopes have been successfully used, like in the case of the OSO-3 observatory.

To improve the point spread function with respect to actively collimated telescopes, pair-tracking telescopes are used. Inside the charged-particle veto, the detecting medium is substituted with a pair-tracking device, commonly a spark chamber. Usually a Čerenkov counter is added, allowing to distinguish between upward- and downward-going electrons and positrons. A calorimeter is often present, to reconstruct the γ energy.

The development of such telescopes was characterized by great difficulties and drawbacks; the major difficulty consisted in the correct shielding of the trigger telescope from the background. The first breakthrough was registered with the SAS-II telescope [26], launched on November 1972: SAS-II proved for the first time that high-energy γ rays could be measured by tracking the secondary electrons. The first clear success in high-energy γ-ray astronomy was obtained with the very effective ESA mission COS-B showing all characteristics of modern pair-tracking telescopes. The EGRET telescope, mounted aboard the Compton Gamma Ray Observer, reached such outstanding results to prompt a new investigation effort in high energy astronomy.

2.3 OSO-3

The Third Orbiting Solar Observatory, OSO-3, was launched on March 1967, into a nearly circular orbit of mean altitude 550 km, inclined at 33° with respect to the equatorial

plane[2]. The satellite hosted a continuously spinning wheel in which the hard X-ray experiment was mounted with a radial view, with a spin-period of ~ 1.7 s; sun and Earth sensors performed attitude measurements, from which the pointing direction could be reconstructed with a precision of $\sim 0.5°$. The attitude control system maintained the scan plane orientation to within a few degrees of the sun. The γ detector allowed for a 1 cm^2/s exposure per revolution to sources on the scan plane; celestial sources near the ecliptic plane such as Sco X-1 transited the instrument scan plane twice a year. Only real-time data were received from the satellite after the last tape recorder failure on 1968 June 27. The last data transmission occurred November 1969; OSO-3 descended into the atmosphere on April 1982.

The γ-ray detector, developed at MIT, was a counter telescope, constituted by a CsI multilayer scintillator, alternating layers of CsI and plastic, a lucite[3] directional Čerenkov counter and a calorimeter, containing several layers of NaI, sandwiched by layers of tungsten [27]. The entire detector was enclosed by plastic scintillator detectors; in Fig. 2.2 a schematic of the instrument is shown.

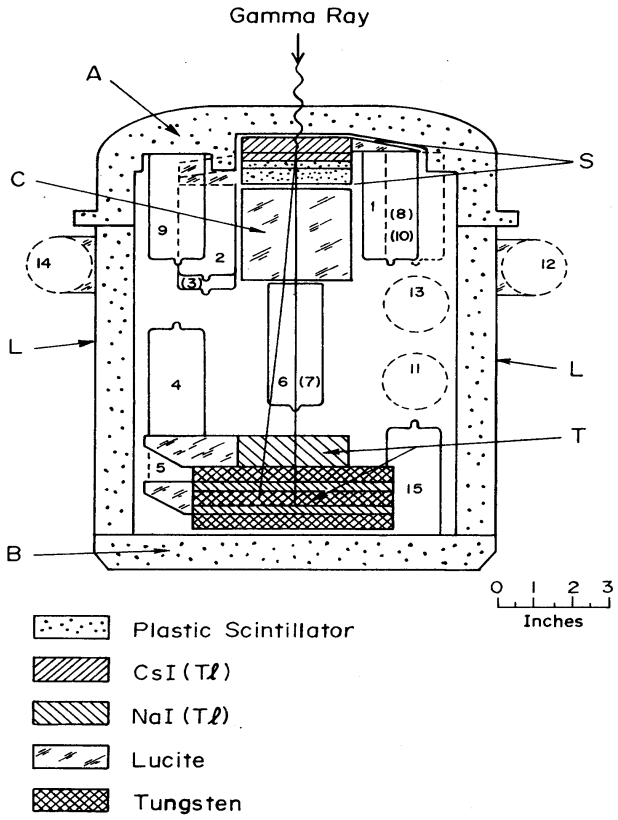

Fig. 2.2 - Diagram of the high energy gamma-ray detector flown on OSO-3 [27].

The γ telescope was sensitive to photons above 50 MeV. Incoming photons would cross the front veto A without triggering it, then they would convert into the front CsI/plastic

[2] – the orbit altitude determines the orbital period, the mission lifetime if altitude corrections are not applied and the radiation exposure, while the inclination defines the sky coverage and the ground stations available for data downlink.

[3] – methyl methacrylate polymer, aka plexiglass.

sandwich S. Secondary electrons and positrons would emit a Čerenkov flash in the lucite counter C, to end in the NaI scintillator T, with no hits recorded on the lateral guard counters L. Hence, the pulse signature was labeled $S\cdot\ C\cdot\ T\cdot\ \bar{A}\cdot\ \bar{L}$.

The FWHM acceptance angle was $\sim 25^\circ$ and the effective area for an axial 100 MeV photon was 2.5 cm^2. In the 16 months before the failure of the tape recorder it registered 621 events; it successfully demonstrated the anisotropy in the γ-ray angular distribution, and unambiguously identified the galactic origin of such anisotropy.

2.4 SAS-2

The NASA *Second Small Astronomy Satellite*, SAS-2, was launched on November 1972. To minimize the background flux from cosmic-rays, SAS-2 was placed in a low Earth equatorial orbit with a 2° orbital inclination. Its apogee and perigee were 610 km and 440 km respectively, with an orbital period of about 95 minutes. The observation program was planned to provide a full sky coverage within 1 year of operation, with early emphasis placed on the galactic plane. On June 1973, a failure of the low-voltage power supply ended the collection of data. During the $\sim$ 6 months the mission lasted, 27 pointed observations (typically a week in duration) were made, resulting in about 55% of the sky being observed, including most of the galactic plane [28].

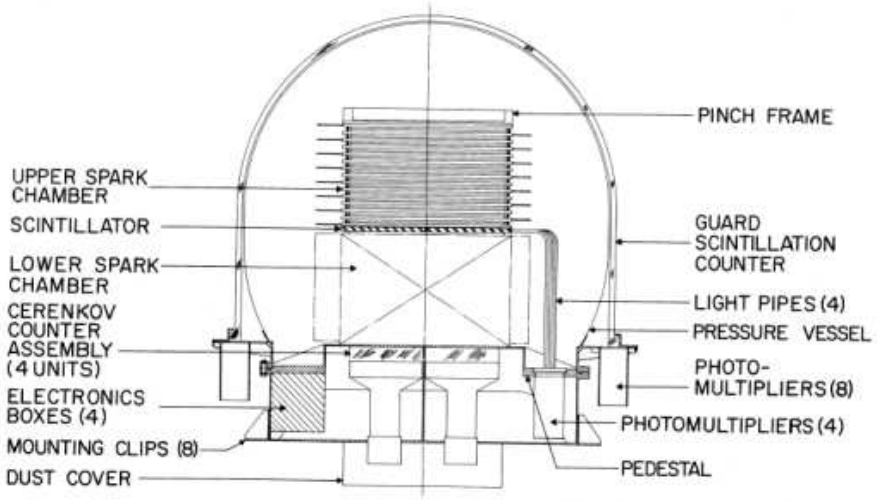

Fig. 2.3 - Schematic diagram of the SAS-2 gamma ray instrument, from [28].

SAS-2 carried a single instrument: a γ-ray telescope with a 32-gap wire spark-chamber. Thin W plates were interleaved between the modules, to convert the γ rays and allowing to determine the energy of secondaries from their multiple Coulomb scattering. The array of plastic scintillator tiles and the directional Čerenkov detectors placed below the spark chamber provided the counter-coincidence system. A plastic scintillator dome encased the whole instrument to discriminate against the charged particle background.

An extensive calibration program was carried out on the γ-ray telescope before SAS-2 was launched. Gamma beams at the National Bureau of Standards (NBS) Synchrotron accelerator (20–114 MeV) and at DESY (200–1000 MeV) were used.

The telescope covered the energy range 20 MeV – 1 GeV with an effective area of almost 120 cm^2 for on-axis photons above 300 MeV; the use of Coulomb scattering limited the

interval of a consistent energy determination in the range 20 MeV – 200 MeV. Angular resolution, about 5° at 35 MeV, improved up to $\sim$ 1.5° at 1000 MeV, normal incidence; angular resolution degraded by 25–30% for photons impinging between 15° and 30° from the vertical. During the short mission lifetime there was some noticeable decrease in sensitivity due to deterioration of the spark-chamber gas.

It is generally acknowledged that SAS-2 provided the first detailed information about the gamma ray sky and demonstrated the ultimate promise of γ-ray astronomy. SAS-2 revealed that the galactic plane γ radiation was strongly correlated with galactic structural features, especially once the known strong discrete sources were subtracted from the total observed radiation. The SAS-2 results clearly established the presence of a high energy ($>$ 35 MeV) component to the diffuse celestial radiation. High-energy γ-ray emission was also observed for discrete sources such as the Crab and Vela pulsars.

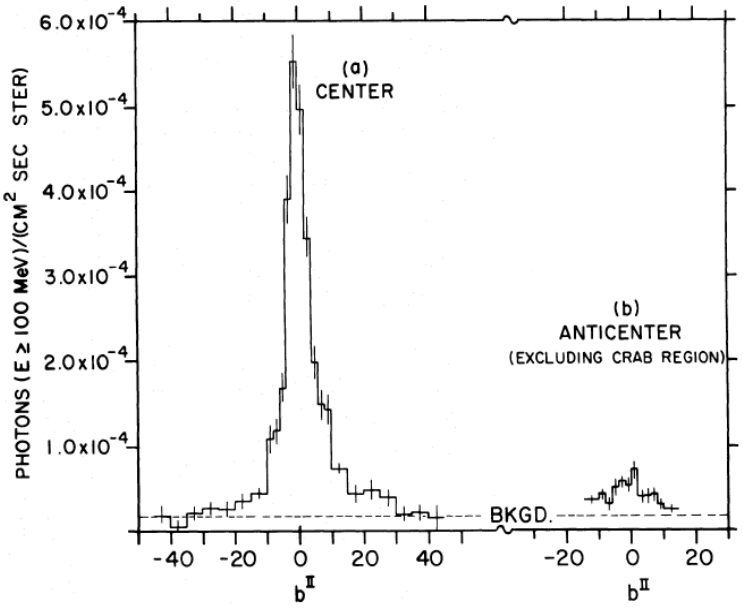

Fig. 2.4 - Distributions of gamma rays above 100 MeV at the galactic center and around the galactic anticenter; diffuse background is shown by the dashed line (from [28]).

2.5 COS-B

Launched on August 1975, the ESA satellite COS-B was originally projected to last two years, but it operated successfully for 6 years and 8 months. This telescope was intended to study in detail the sources of extraterrestrial gamma radiation at energies above $\sim$ 30 MeV [29].

COS-B operated in pointing mode with its axis directed towards fixed points in the sky. Its operative time period was about 25 hours during a 37-hour orbit, inclined at roughly 90° to the Earth's equator at 100,000 km above sea level. About one quarter of the observations were performed at higher galactic latitudes, especially in regions expected to contain extragalactic sources. Pointing periods lasted four to five weeks during the early part of the mission and up to 3 months during the later observations. A broad portion of the galactic equator was studied deeply by means of repeatedly overlapping observations. Nearly half of the celestial sphere was viewed by COS-B.

COS-B carried a single large experiment, the *Gamma-Ray Telescope*, which performed well throughout the mission, the only complication being the occasional erratic performance of the spark-chamber and the inevitable reduction in performance as the spark chamber gas aged. This aging was minimized, however, by means of a gas-replenishment system that permitted to empty and refill the spark chamber. As the rate of gas deterioration decreased with time, it became possible to increase the interval between flushing from the initial value of once every 6 weeks to about once every 36 weeks before the final flushing on November 1981. The spark chamber was still performing creditably at the end of the mission on April 1982.

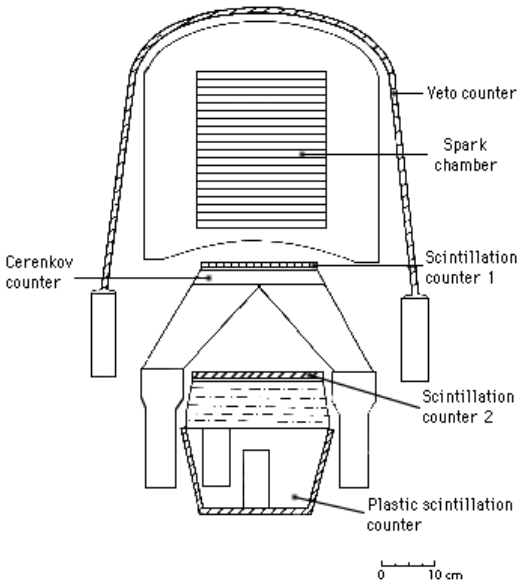

Fig. 2.5 - Diagram of the gamma-ray detector on COS-B.

The Gamma-Ray Telescope consisted of a magnetic-core, wire-matrix spark chamber with an effective area of 576 cm^2. Each sensitive layer was constituted by two parallel wire systems to reconstruct both X and Y coordinates; each wire plane contained 192 wires spaced by 1.25 mm. Between each wire system a W plate was placed, for a total of ~ 0.4 X_0; below the spark chamber 4 additional Mo plates, for an additional ~ 0.5 X_0 were placed. Below these a three-element Čerenkov counter was placed to serve as trigger. A plastic scintillator guard counter surrounding the active units served as an anti-coincidence detector to reject triggers due to incident charged particles.

Beneath the telescope was a CsI calorimeter, 4.7 X_0 thick, which absorbed and measured the secondary particles produced by the incident photons; the yield of the calorimetric system was about 150 photoelectrons/MeV. A 1 cm thick plastic scintillator was placed below the calorimeter to measure the leakage rate of γ rays with energies above $\sim$ 300 MeV.

COS-B was sensitive to γ rays in the energy range from $\sim$ 30 MeV to several GeV over a field of view of $\sim$ 2 sr. The energy resolution had its best value ($\sim$ 40% FWHM) at about 100 MeV and was better than 100% up to at least 5 GeV. The instrument sensitive area had its maximum of $\sim$ 50 cm^2 at several hundred MeV, falling rapidly to zero at an angle of about 30°. The angular resolution, $\sim 3.5°$ at 100 MeV, dropped at $\sim 1°$ above $\sim$ 300 MeV.

The key results of the COS-B mission are resumed in [30]. First of all the 2CG catalogue

[31] was drawn up, containing about 25 γ-ray sources out of 30 observations made during the first three years and a complete gamma-ray map of the disc of the Milky Way, based on about 200,000 events. COS-B devoted a great part of its lifetime to the search for γ-ray emissions from the Cygnus X-3 X-ray pulsar. Despite devoting to this task about 10% of the entire mission, it did not detect gamma variability although the X-ray variability was clearly seen by the on-board X-ray monitor. Crab and Vela pulsars were observed several times, and variations in the light curves of the former have been documented. A later maximum likelihood analysis [32] has shown that changes in the intensity of Vela and a spectral dependency of the light curve can be desumed from COS-B data in the high-energy regime (50 MeV – 5 GeV).

COS-B raw data, plus several sky maps obtained from the 65 observations made during the entire mission are available on-line [33]. As an example in Fig. 2.6 the Vela pulsar is shown in a contour plot, using $\sim 14,000$ events in the full 50 MeV – 5 GeV range.

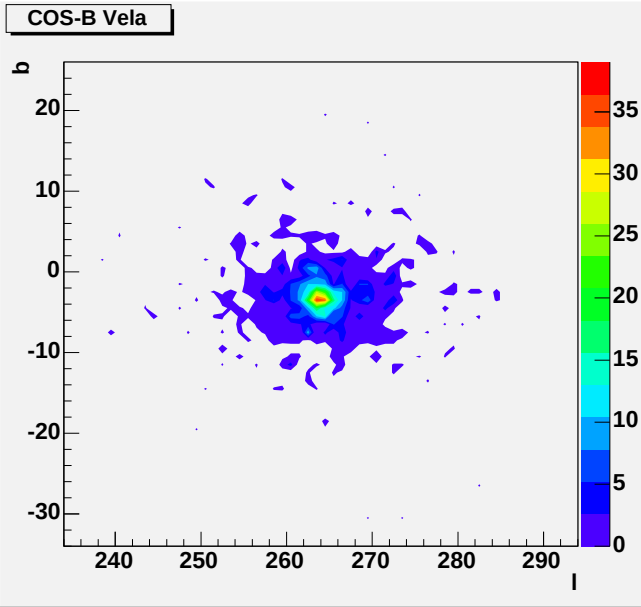

Fig. 2.6 - The Vela pulsar, as seen by COS-B; events taken in about 18 days, from [33].

2.6 EGRET

The *Energetic Gamma Ray Experiment Telescope* (EGRET) [34] was the high-energy γ instrument aboard the *Compton Gamma Ray Observatory* (CGRO)[(4)]. Its main purpose was to make a major advance in high energy γ-ray astrophysics using a telescope with more than one order of magnitude greater sensitivity and better angular and energy resolution than those previously flown.

Launched on April 1991 aboard the space shuttle Atlantis, CGRO was safely deorbited and re-entered the Earth's atmosphere on June 4, 2000. To maximize the spectral energy coverage it carried four different instruments: the *Burst And Transient Source Experiment* (BATSE, 10 keV – 100 MeV), the *Oriented Scintillation Spectrometer Experiment* (OSSE,

(4) – the name of the Observatory was chosen in honor of Dr. Arthur Holly Compton, Nobel prize in 1927.

50 keV – 10 MeV), the *Imaging Compton Telescope* (COMPTEL, 0.8 – 30 MeV), and EGRET (20 MeV – 30 GeV).

EGRET used a multilevel thin-plate spark chamber system, placed on top of a NaI(Tl) calorimeter. The upper spark chamber assembly consisted of 28 spark chamber modules interleaved with 27 plates (0.02 X_0 each) in which the γ ray could convert. The lower spark chamber assembly, between the two time-of-flight plastic scintillator planes, allowed the pair trajectories to be followed, providing further information on the energy of tracked particles and showing their entry points into the calorimeter. The 7.7 X_0 calorimeter placed beneath the instrument provided good energy resolution over a wide dynamic range. The active elements were covered by a plastic scintillator anticoincidence dome to prevent triggering on events not associated with γ rays.

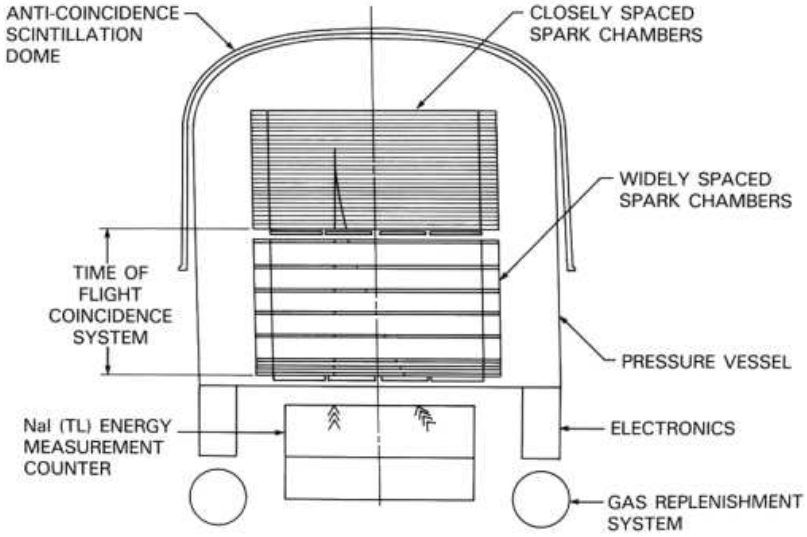

Fig. 2.7 - Diagram of the EGRET instrument [35].

EGRET had an energy resolution of 20-25% FWHM. Its angular resolution improved from 10° at 60 MeV to 0.5° at 10 GeV, and the effective area reached ~ 1500 cm^2 at several hundred MeV for on-axis photons. Point source sensitivity varied with the spectrum and location of the source and the observing time; under optimum conditions, well off the galactic plane, the 3σ sensitivity reached $\sim 6 \cdot 10^{-8}$cm^{-2}s^{-1} for energies above 100 MeV and for a full two week exposure, an order of magnitude better than what obtained by COS-B. A summary of EGRET performances is shown in Tab. 2.2.

EGRET major results are:

- the drawing up of the 3EG source catalogue, with 271 entries above 100 MeV [36];
- the finding of a new class of objects — high energy gamma-ray emitting *blazars*;
- the emission of high energy γ rays from a gamma ray burst for over an hour, with some gamma rays having energies over a GeV and two having energies over 10 GeV;
- the observation of an increased fraction of pulsar electromagnetic radiation going into gamma rays as the age of the pulsar increases to a million years;
- the determination with high certainty that the origin of cosmic rays is galactic;

- the detailed mapping of the galactic diffuse radiation and the measurement of the pion bump in the high energy gamma-ray spectrum;
- a measurement of the diffuse, presumably extragalactic, high energy gamma ray spectrum.

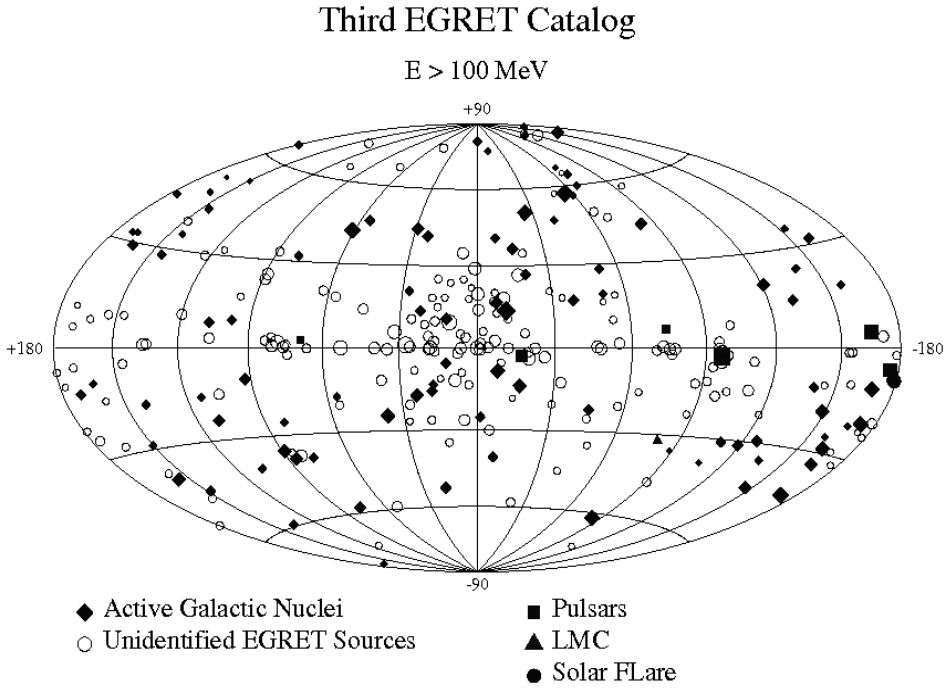

Fig. 2.8 - The third EGRET catalog, from [36].

2.7 BATSE

The *Burst And Transient Source Experiment* (BATSE) consisted of eight uncollimated detector modules arranged on the corners of the CGRO observatory: this placement provided the maximum unobstructed view of the celestial sphere. Each detector module contained two NaI(Tl) scintillation detectors: a *Large Area Detector* (LAD) optimized for sensitivity and directional response, and a *Spectroscopy Detector* (SD) optimized for energy coverage and energy resolution.

The LAD detector was a disk of NaI(Tl) scintillator 20 inches in diameter and one-half inch thick, mounted on a three-quarters inch layer of quartz. A light collector housing on each detector brought the scintillation light into three 5-inch diameter photomultiplier tubes. The signals from the three tubes were summed at the detector. A quarter-inch plastic scintillation detector in front of the LAD was used as an anticoincidence shield to reduce the background due to charged particles. A thin Pb and Sn shield inside the light collector housing reduced the amount of background and scattered radiation entering the back side.

The spectroscopy detector was an uncollimated NaI(Tl) scintillation detector 5 inches in diameter and 3 inches thick. A single 5 inch photomultiplier tube was directly coupled to the scintillation detector window. The housing of the PMT had a passive Pb/Sn shield similar to that of the LADs. The crystal housing had a 3-inch diameter 50-mil thickness

Be window on its front face in order to provide high efficiency down to 10 keV.

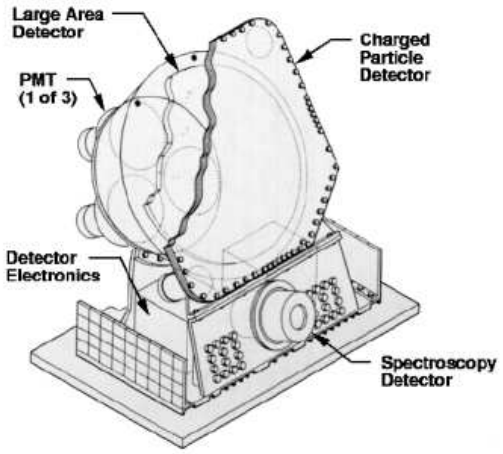

Fig. 2.9 - One of the 8 identical BATSE modules.

BATSE detected bursts on-board by examining the count rates of each of the eight LADs for a statistically significant increase above background on each of three time scales: 64 ms, 256 ms, and 1024 ms; the background rate was determined for each detector over an adjustable time interval. At least two detectors should exceed the threshold for a burst trigger to occur. As an additional requirement for burst triggering, the detector with the greatest increase in count rate should have an increase in the charged particle rate below a specified fraction of the increase in the neutral rate. This in order to avoid triggering on charged-particle event encounters, such as those produced by spacecraft containing nuclear reactor power sources.

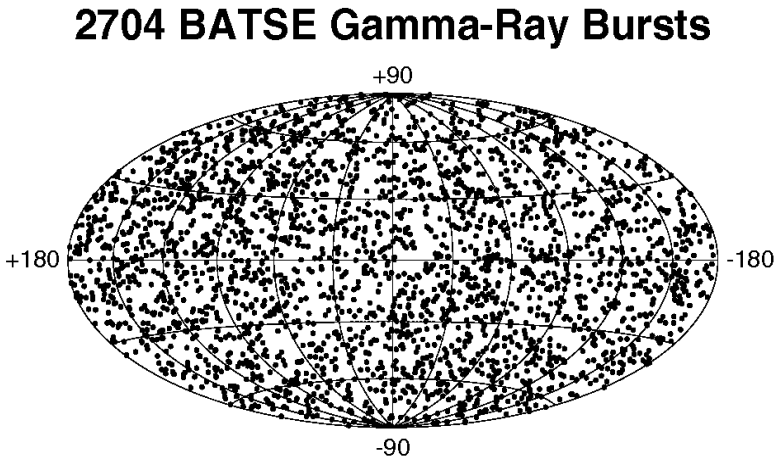

Fig. 2.10 - The bursts observed by BATSE, in galactic coordinates.

BATSE had an effective area of 2025 cm^2 per LAD and 127 cm^2 per SD. Its energy range was 20 keV – 1.9 MeV for LAD and 10 keV – 100 MeV for SD detectors. Its flux sensitivity for a 1 s burst was 3×10^{-8} ergs/cm^2, while time resolution was 2 s minimum. A summary of BATSE characteristics is shown in Tab. 2.1.

At the time of its removal from orbit, after $\sim$ 9 years, BATSE had collected 8021 triggers. Of these, 2704 were identified with GRBs, 185 as γ repeaters, 1192 as solar flares, 1717 magnetospheric events and 2003 as transient sources. A skymap of all detected GRBs is shown in Fig. 2.10.

2.8 The GLAST Mission

In 1995, NASA formed the *Gamma-Ray Astronomy Program Working Group* to formulate recommendations for future directions in NASA's gamma-ray astronomy program. This working group met four times over the next 2 years, after which it presented a summary [37] of the findings and gave detailed recommendations for future NASA projects. The highest priority recommendation was GLAST, a next-generation 10 MeV to 100 GeV gamma-ray mission expected to improve sensitivity by one or two orders of magnitude with respect to the CGRO EGRET project.

On August 1999 the NASA Office for Space Science (OSS) released a GLAST Announcement of Opportunity [38], a solicitation to domestic and foreign organizations to contribute proposals for scientific investigations with the suggested spacecraft. In response to this, on November 1999 a Flight Investigation Document [39] was submitted to NASA, addressing the instrument design, its capabilities and the scientific goals it would achieve. The overall structure of the GLAST instruments was defined and their capabilities assessed.

In the next Sections a description of the GLAST instruments and their characteristics will be presented; for each high-energy astrophysical phenomenon a description of GLAST required capabilities in the field was given in Chap. 1.

The GLAST satellite will be placed in an unattended orbit at an altitude of 565 km with 28.5° inclination. GLAST operation will be split in two phases, one devoted to obtain a uniform sky map, the other dedicated to a detailed study of single sources. After orbit deployment, instrument checkout and calibration, GLAST will perform a one-year all-sky survey. During this period the spacecraft will be oriented in rocking zenith mode to point the LAT instrument in a general zenith direction with some rocking motion around the orbit to improve the uniformity of the sky coverage. There may be occasional interruptions of the survey for pointed observations of particular transient sources. The pointed mode has the LAT instrument oriented toward a position of interest to within 30° while it is above the Earth's disk. After the one-year survey, the mission will have a mixture of rocking zenith and pointed mode observations. In sky survey mode the GLAST system is intended to obtain 100% sky coverage every 3 orbits with an observing efficiency greater than 70%; in pointed observation mode, it is expected to achieve $> 50\%$ observing efficiency.

The basic instrument requirements are defined in a two step process. First, major science themes are identified. These themes are largely based upon the scientific goals for a high-energy gamma-ray mission as outlined by the GRAPWG group [40]. The second step in the requirement definition process is, for each of the major science themes, an estimate of the basic telescope properties that are most relevant to reaching the scientific goals. In many cases, it is natural to make direct comparisons with the EGRET instrument, the most recent and successful experiment for high energy gamma-ray astronomy, and the BATSE instrument for gamma-ray bursts.

2.9 The GLAST Burst Monitor

The *GLAST Burst Monitor* (GBM) was selected as a complementary instrument for the GLAST mission and will be sensitive to X rays and γ rays with energies between 5 keV and 25 MeV. The combination of the GBM and the LAT provides a powerful tool

for studying gamma-ray bursts, particularly for time-resolved spectral studies over a very large energy band.

GBM will be composed by 12 *Low Energy Detectors* (LED): NaI scintillators, each 5 inches in diameter. Additionally, there will be two *High Energy Detectors* (HED): BGO detectors, each 5 inches in diameter by 5 inches thick. The NaI detectors cover the lower part of the energy range, from a few keV to about 1 MeV, and provide burst triggers and locations: burst locations are determined from the relative count rates (as was done on BATSE). The BGO detectors cover the energy range 10 keV – 25 MeV, providing good overlap with the NaI at the low end, and with the LAT at the high end.

The GBM field of view will be greater than 8 steradians. It will have an effective area of 126 cm^2 per detector, and 2 μs time resolution. It will require 1.8 s to locate a GRB within 15°; its dead time will be < 2 μsec/count. Its energy resolution will be better than 20% FWHM at 511 keV, up to $\sim 7\%$ at 2 MeV. A summary of the design requirement for the GBM and a comparison with BATSE capabilities is shown in Tab. 2.1.

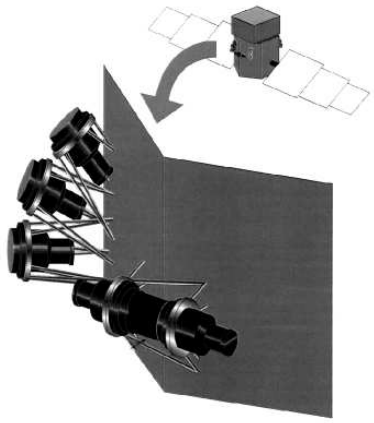

Fig. 2.11 - The GBM: arrangement of 3 NaI detectors and 1 BGO detector on the GLAST spacecraft [41].

Parameter	GBM requirement	BATSE
Energy range	8 keV - 1 MeV (LED) 150 keV - 30 MeV (HED)	10 keV - 1.8 MeV (LAD) 15 keV - >30 MeV (SD)
Energy resolution	20% FWHM at 511 keV	~20% FWHM at 511 keV
Time resolution	10 μs	2 μs
On-board GRB locations	20° accuracy (1σ) within 2 s	none
Rapid ground GRB locations	5° accuracy (1σ) within 5 s	10° within 5 s 3° within 5 min
GRB sensitivity	0.5 ph/(cm^2s) (peak flux, 50-300 keV)	0.1 ph/(cm^2s) (peak flux, 50 300 keV)
Field of view	8 srad	4π srad
Deadtime	<10 μs/count	~10 μs/count

Tab. 2.1 - Comparison of GBM design requirements and BATSE perofrmances.

For the 150 GRBs which are expected to trigger the GBM each year there will be a

three-stage location refinement: onboard, ground-automated, and ground-manual.

- The onboard location is the least accurate and is used to re-point the spacecraft to allow the LAT to detect delayed high-energy emission from GRBs which occurred outside its field of view. This crude location will be obtained within seconds of the trigger, and needs to be accurate only to about 20° to insure coverage by the LAT after repointing.
- The ground-based automated response occurs in near real-time and is based on the Global Coordinates Network system. This location will be accurate to a few degrees (depending on burst intensity) and will provide coordinates for rapid follow-up by ground-based instruments.
- The ground-based manual location will be provided days after the trigger, with a human operator performing a detailed analysis and the best possible burst location to be entered in the burst catalog. An accurate spectral model will be obtained, and the consequent careful generation of error boxes will reduce the systematic error associated with these locations to about 1.5°.

2.10 The LAT Instrument

LAT is a high-energy pair conversion telescope. The design is based on experience with EGRET, and on proven technologies with either flight heritage or comprehensive experience derived from widespread and documented performance in high-energy physics experiments.

Quantity	**LAT Spec.**	**EGRET**
Energy Range	20 MeV - 300 GeV	20 MeV - 30 GeV
Peak Effective Area	> 8000 cm^2	1500 cm^2
Field of View	> 2 sr	0.5 sr
Angular Resolution (100 MeV)	< 3.5°	5.8°
Angular Resolution (10 GeV)	< 0.15°	
Energy Resolution	< 10%	10%
Dead Time	< 100 μs	100 ms
Source Location Determination	< 0.5′	1.5′
Point Source Sensitivity	$< 6 \times 10^{-9} cm^{-2} s^{-1}$	$\approx 10^{-7} cm^{-2} s^{-1}$

Tab. 2.2 - GLAST LAT Specifications Compared with EGRET [1].

The tracking stacks, in contrast to spark chambers, will be made of silicon strip detectors. The tracker will be followed by a CsI calorimeter, to which a precise energy reconstruction is entrusted. The overall scheme is thus the one employed in the tracking cores of modern high-energy physics collider experiments. This choice will ensure much higher efficiency over a wider angle of incidence, better precision and stability and no need of consumables. The absence of a time-of-flight measurement greatly increases the field of view over that of EGRET, allowing for a wider photon acceptance cone. A detailed analysis of the LAT is given in the next Chapter.

The main requirements for the LAT are summarized in Tab. 2.2; a comparison with EGRET performances is presented. It must be considered that, beside the parameters

dictated by scientific requirements, space operation forces a large series of constraints on the instrument characteristics. Small lateral dimensions (< 1.8 m) restrict the geometrical area, while the low mass (< 3000 kg) primarily put a (small) upper limit on the calorimeter thickness and therefore on the energy reach. Often different requirements clash: the limited available power (< 650 W) limits the number of readout channels and the capabilities of the electronics, while the data downlink, limited to 300 kbps, requires the LAT to have good background rejection capabilities. Another key issue is the instrument sensitivity to failures: as repairing damaged components is not possible, robust and redundant design is the key aspect in determining the mission lifetime.

3 The GLAST LAT

In this chapter we describe the main GLAST instrument, the LAT. In particular, tracker ASICs are described in great detail, as Chap. 7 deals almost entirely with the radiation testing of tracker space parts. The DAQ ASICs are addressed in some detail, as we took part in their radiation testing too.

3.1 The LAT

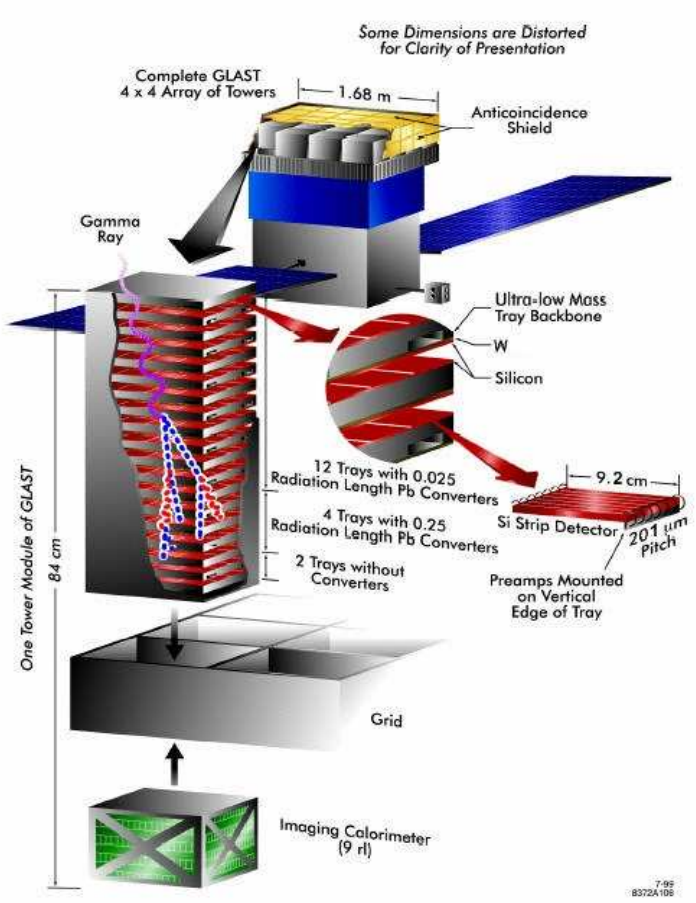

Fig. 3.1 - LAT schematic representation.

Fig. 3.1 shows a schematic representation of the GLAST LAT. An *Anticoincidence Detector* (ACD) surrounds the whole instrument, vetoing charged particles, five orders of magnitude more abundant than gamma rays in the GLAST orbit. Inside the ACD sixteen identical towers are placed in a 4×4 grid. Each tower is composed of a *Tracker* module (TKR) on top of the corresponding *Calorimeter* element (CAL). On the bottom the *Tower Electronics Module* (TEM) with the *Data Acquisition* electronics (DAQ) are located. The towers are inserted in an aluminum grid, constituting the structural backbone of the LAT and serving as a thermal path to conduct the heat produced by the active elements to the radiators. A foam thermal blanket encloses everything, providing both a light-tight cover

and a micro-meteor shield. In the next sections we will describe in detail the various LAT subsystems, with emphasis on the scientific capabilities ensured by the careful design[(1)].

3.2 ACD

The AntiCoincidence Detector is composed by 89 tiles of plastic scintillator, 25 on the LAT top and 16 on each of the four sides, for a total surface of ~ 8.6 m^2 [42]. Each tile is read by means of two wavelength-shifting fibers (WSF) interleaved in it by two photomultiplier tubes (PMT). To ensure maximum coverage the ACD tiles overlap in one direction, while 8 scintillating fiber ribbons seal the gaps in the other, with two PMTs per ribbon. Each tile is enclosed in its own light-tight envelope to limit the impact of micrometeoric punctures. PMTs are Hamamatsu head-on tubes with a maximum gain of $\sim 10^6$; the gain is set to $\sim 4 \times 10^5$ but can be adjusted as required during the operation of the instrument by varying the high voltage bias.

The nominal photoelectron production in the scintillating tiles is 20 photoelectrons per MIP, providing a nominal 10 photoelectrons/MIP at the photocathode of each tube. The design requirement calls for handling a signal range from 0.1 MIP to 1000 MIPs; the charge input to the front-end ASICs therefore ranges from 0.064 pC to 640 pC.

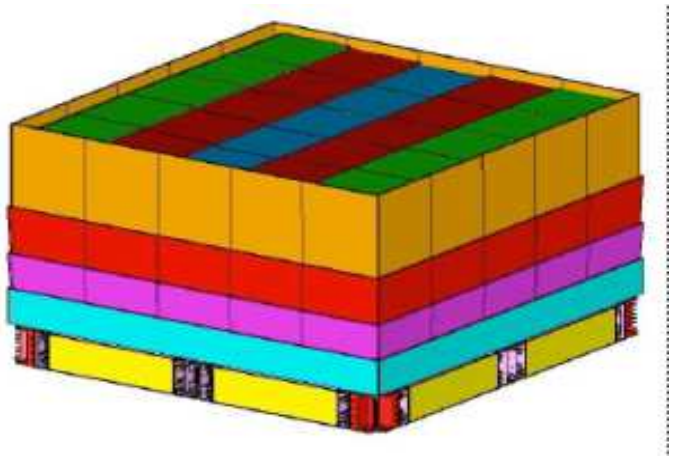

Fig. 3.2 - A schematic of the ACD tiles disposition around the LAT.

12 ACD Front-End Electronics (FREE) circuit cards are arranged around the Base Electronics Assembly (BEA). The BEA has eight bays, two on each side: each bay can house up two FREE cards, four *High Voltage Bias Supplies* (HVBS), and 36 PMTs. The total power dissipated by the ACD electronics is constrained to be less than 37 watts. Each FREE board hosts 18 *GLAST ACD Front-End* (GAFE) ASICs and one *GLAST ACD Readout Control* ASIC. The GARC interfaces the FREE board with the *ACD Electronic Module* (AEM). The primary purpose of the ACD front-end electronics is to receive the PMT signals and process them after suitable amplification, generate fast triggers or discriminator outputs and shape and hold the signal for Pulse Height Analysis (PHA).

The ACD is designed to reject charged particles with an efficiency of at least $3 \times 10^3 : 1$ for a MIP ($10^3 : 1$ for bottom rows only) [43]. This can constitute a problem when EM

(1) – Foldout D of [39] details the derivation of LAT design and instrument constraints from the scientific program requirements.

showers develop in the calorimeter: a low energy photon (0.2–2 MeV) loses in an ACD tile an amount on energy roughly comparable with a MIP due to Compton scattering. This *calorimeter backsplash* led to a 50% effective area loss in EGRET for 10 GeV incident photons relative to that at 1 GeV [44]. In GLAST the same *self-veto* is reduced to $< 20\%$ of all events at 300 GeV thanks to the segmentation, requiring that the direction of the recostructed incident particle cross the ACD tile registering a pulse.

3.3 CAL

Similarly to EGRET, the LAT calorimeter is composed of CsI(Tl) crystals read by photodiodes. As the energy resolution strongly depends on depth, sampling, and longitudinal segmentation, each CAL module is finely segmented both in depth and lateral directions: each tower will contain 8 CAL layers, each constituted by 12 crystals ($27 \times 20 \times 326$ mm^3) wrapped in reflective foil, for a total of $\sim 8.5\ X_0$. As with TKR silicon detectors (see Sect. 3.5), each layer will be at 90° with respect to the previous one, to achieve x-y imaging capabilities (*hodoscopic configuration*). Lateral segmentation will provide the necessary imaging capability to correlate events in the TKR with energy depositions in the CAL; the imaging capability can also be used to measure the direction of high-energy photons that do not convert in the TKR, with a resolution at the level of a few degrees. The longitudinal segmentation enables energy measurements up to a TeV: it is possible to derive an unbiased estimate of the initial electron energy from the longitudinal shower profile by fitting the measurements to an analytical description of the energy-dependent mean longitudinal profile. Moreover, one side of each crystal is carefully scratched to allow for a small loss when light travels along it (*light tapering*): thanks to this it is possible to reconstruct the point along the crystal where the energy was released from the asymmetry in the light yield at the two ends.

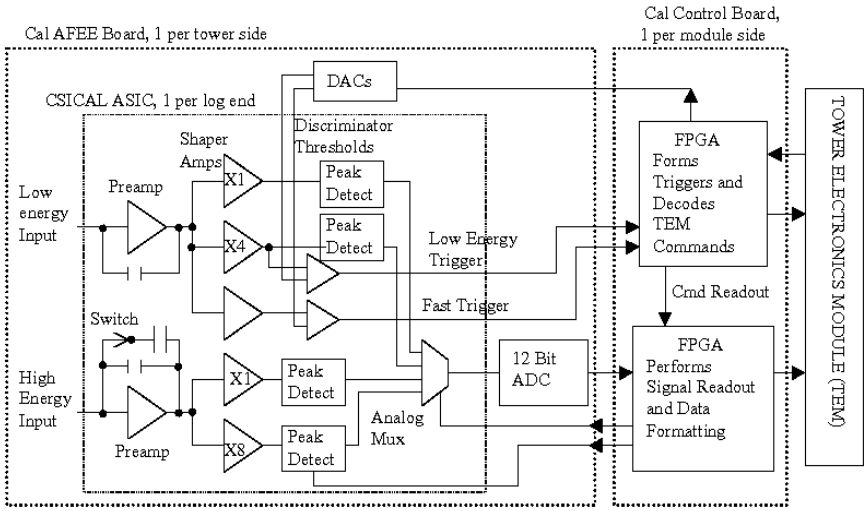

Fig. 3.3 - Block diagram for the organization of the CAL electronics, from [45].

The calorimeter electronics has to perform spectroscopic measurements over a dynamic range of 5×10^5, while keeping power consumption as low as ~ 20 mW per crystal edge.

Moreover, the deadtime in processing each event must not exceed ~ 20 μs per event. The CAL electronics divides the dynamic range into two independent signal chains; similarly each CsI(Tl) crystal will be read from both ends with a sensor constituted by two PIN photodiodes, a small one (24 mm^2) called *High Energy PIN Diode* (HEPD) and a bigger one (96 mm^2) called *Low Energy PIN Diode* (LEPD). A LEPD can measure energies in the range 2 – 800 MeV, while for a HEPD the range is 100 MeV – 100 GeV.

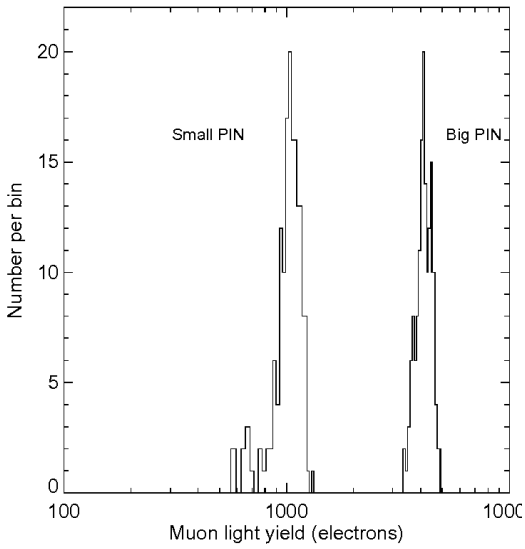

Fig. 3.4 - Light yield for impinging muons on 80 crystals from the BTEM calorimeter, from [45].

The analog ASIC for the calorimeter, CSICAL, supports the two PIN photodiodes on one CsI crystal end. It has two preamplifiers, 1 for each diode. Each preamplifier has three shapers - full range at 3.5 μs shaping, 1/4 range (or 1/8 range for the HEPD channel) at 3.5 μs, and an auxiliary full range at 0.5 μs. The ASIC processes signals from one crystal end - one low energy diode and one high-energy diode. Each PIN diode injects charge to a charge sensitive preamplifier; the sensitivity for the low and high energy channels are different. The signal from each preamplifier is then further divided into two shapers with a peaking time of ~ 3.5 μs. These two shaping amplifiers have gains that differ by a factor 4 in the low energy chain (8 in the high energy chain) so that one processes the full dynamic range for that PIN diode, while the other processes only the lowest 1/4th of the range (1/8th in the high energy chain). The two shapers are followed by peak-detectors with track-and-hold, which capture the peak amplitude of the pulse and stretch it for subsequent digitization by the analog to digital converter. Reference discriminators on the shapers are used by the control electronics to identify the initiation of an event (lower level threshold discriminator) and to identify range overflow. An additional, faster shaping amplifier with peaking time of 0.5 μs with associated discriminator is used for calorimeter triggering of the full GLAST instrument. There are 4 peak-detecting track-and-hold's, one for each 3.5 μs shaper; an analog multiplexer on the output of the four track-and-hold's selects the energy range that will be digitized. Digital control signals provide the timing and sequencing for the capture of the event and the subsequent timing for the interface to the ADCs. A second ASIC, VICAL, converts CMOS voltage control

signals into the required current controls. It also converts CSICAL discriminator outputs, i.e. current signals into CMOS voltage signals.

A prototype CsI hodoscopic calorimeter was assembled for the Beam Test Engineering Module (BTEM), a full size prototype of one of the 16 towers of the GLAST LAT [45]. The BTEM calorimeter is comprised of 80 CsI crystals organized in a hodoscopic arrangement with 8 layers of 10 crystals. The major design goals included the demonstration of a mechanical design to survive launch into space with minimal passive material, low power electronics with adequate dynamic range and digital data acquisition with less than 20 μs dead time per event. Absolute light yield for the CsI cristals was measured with cosmic muons. For a typical angle-of-incidence of 20°, a muon typically deposits 13 MeV across the 23 mm thick crystal; the yield is $\sim$ 4200 e/MeV in the LEPD and $\sim$ 1000 e/MeV in the HEPD. Fig. 3.4 shows the distribution of muon light yields in the two PIN diodes for the 80 crystals chosen for the BTEM calorimeter: the light yield rms for the large PIN is $\sim$ 4%.

Asymmetry in the signal from the two readout faces given by the optical tapering was measured and the position reconstructed with the telescope configuration using 2 GeV electrons at SLAC. In Fig. 3.5 the results are shown: for most of the length of a crystal the asymmetry is linearly related to the position of interaction and, therefore, it is the slope of the asymmetry (expressed e.g. in % per cm) that determines the position resolution of the crystal assembly. The typical position resolution ranges from a few mm for energy depositions around $\sim$ 10 MeV, while it improves to a fraction of a millimeter for depositions above 1 GeV.

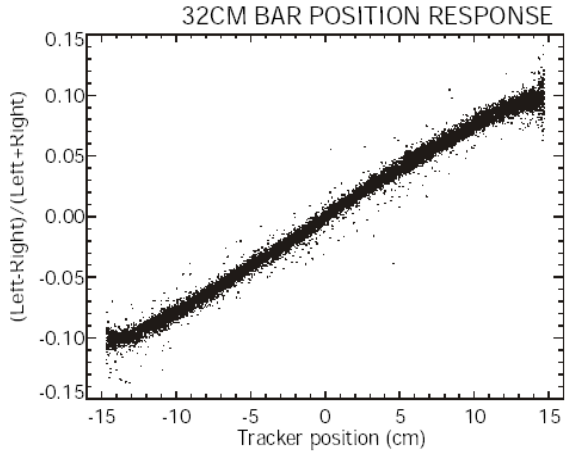

Fig. 3.5 - Left/right signal asymmetry in CAL crystals due to tapering for 2 GeV electrons ($\sim$ 130 MeV deposited), from [45].

3.4 DAQ and triggering

The primary functions of the DAQ are to trigger the LAT (the *Level-1 Trigger*, or L1T), read out the event data into its own memory and process them into a downlink stream. It also performs the functions of instrument control and monitoring. The DAQ hardware performs the L1T and read out functions without the direct participation of the data processor. The first processing level is the Level-2 Trigger (L2T) and is performed locally at the tower level. Events passing L2T are transmitted to a processor located

in the Spacecraft Interface Unit (SIU) for additional filtering (the Level-3 Trigger or L3T). Events passing L3T are sent to the Spacecraft Solid State Recorder (SSR) for later downlink.

The total DAQ processing power is 720 Mips, calculated as 40 Mips of available processing power for each of the 18 CPUs (16 TEM + AEM + SIU-TEM) (36 MIPs are required at the peak cosmic ray trigger rate of 9 kHz). When CPUs are not active, they can be put in sleep mode to reduce power consumption.

At the highest level, the *GLAST Gobal Trigger* (GLT) accepts a number of input signals and, in real time, decides whether to issue a L1T signal, latching the front-end signals. An *Algorithm Engine* combines the input signals, called *trigger primitives*, to form specific *named triggers*. Each of the 16 towers and the ACD contributes a number of trigger primitives from which a trigger decision is made. These trigger primitives then are transmitted to the GLT where they are combined and reduced to a more manageable number; the named triggers, in turn, are transformed into a L1T Request.

A tower contributes 3 signals for a total of 48 for the 16 towers to the GLT: a TKR 3-in-a-row signal, a CAL LO discriminator signal and a CAL HI discriminator signal. The ACD contributes as much as 33 primitives: indications of signals from the tiles, HI and LO discriminators, etc. As an example of L1T, let us consider a trigger primitive be issued from the TKR-CAL assembly, e.g. because three consecutive x-y planes fired simultaneously, or the calorimeter registeed an energy deposition above a set threshold. A veto is then applied if an ACD tile associated with a TKR hit fires, or if more than three ACD tiles fire. Each ACD tile produces a LO and HI discriminator signal (thresholds are $\sim$ 1 GeV and $\sim$ 10 GeV respectively). The LO discriminator signals the passage of a minimum ionizing particle, while the HI discriminator signals the passage of a heavy nucleus, a so-called CNO. Notice that a HI signal is generally used to generate a trigger accept, as contrasted with the LO discriminator which is typically used as a veto, this to avoid the self-vetoing (see Sect. 3.2). The trigger primitives above are then processed into named triggers, as "3-in-a-row", "3-in-a-row with ACD Veto", "High Energy CAL", "Lo Energy CAL" and others. The estimate for L1T rates are 6 kHz for average conditions, with peaks around 9 kHz.

L2T, still a tower-level function, implements the ACD veto more rigorously than L1T. It rejects obvious background events efficiently and quickly with loose cuts, thereby avoiding unnecessary computing loads on L3 processing. It is able to remove any residual TKR triggers due to stochastic noise. A fast, efficient track finding algorithm is used to extrapolate track candidates and intersect them with ACD tiles to search for vetoes. Events with a high-energy CAL signature are not vetoed. Current estimates for the L2T rate are 1 kHz average, 2 kHz peak.

L3T occurs in the SIU where it carries out a full instrument-wide event reconstruction with feedback from the attitude control system. Based on current estimates of the event size, the background trigger rate should drop to less than 15 Hz.

3.5 TKR

Silicon strip detectors have a firmly established role in large particle-physics and space-based experiments. The segmentation they allow easily permits one to achieve the resolution required for GLAST. With their primary signal of tens of thousands of electrons, they

can operate at essentially 100% efficiency with very low noise occupancy and little risk of system degradation. They are readily integrated into large systems using standard VLSI technology and commercialized electronics assembly methods and the absence of consumables makes them the perfect candidate for space applications. The main challenge was given by the power consumption required by the readout electronics, given the amount of channels involved (almost 10^6); the GLAST R&D program successfully demonstrated the possibility to have readout electronics requiring only ~ 250 μW per channel, thus fitting inside the power budget of the GLAST mission.

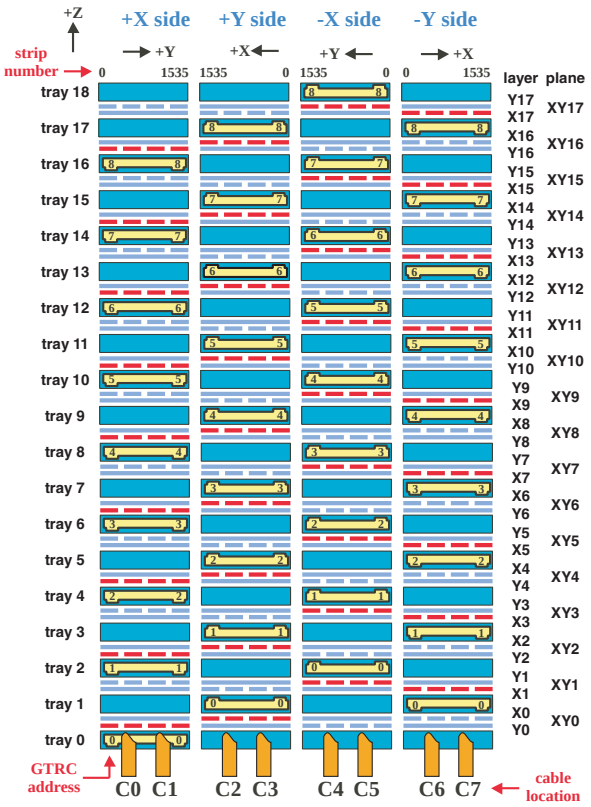

Fig. 3.6 - Schematic of a TKR tower setup; the MCMs are shown attached on the TKR trays, see also Fig. 3.7.

The tracker module contained in each tower is composed of 19 tracking *trays*, containing the Tungsten converter plate and the silicon planes. Each tray contains the silicon planes composed of two single-sided silicon strip detector (SSD) planes, one on top and one on the bottom, with the strips oriented in the same directions. So, each tray will be placed at 90° with respect to the previous ones and thus creating x-y planes. Between the silicon planes is inserted a W foil (see Fig. 3.7 for the schematic representation of a TKR tray).

Each SSD plane is in turn constituted by four adjacent ladders, each made up by four square SSD detectors: a schematic is shown in Fig 3.7. Each TKR tower contains 19 trays: 12 with a 0.03 X_0 W foil (*front trays*), 4 with a 0.18 X_0 W foil (*back trays*) and 3 with no converter foil, for a total thickness of 1.08 X_0. The *top tray* has no upper silicon plane, while the *bottom tray* has no lower SSD plane, for a total of 18 coupled x-y silicon planes. Taking into account all support materials we reach a TKR thickness of about 1.5–1.6 X_0.

The choice of the W plane thickness is crucial in order to ensure a good efficiency while minimizing the impact of multiple scattering and therefore on resolution. A compromise solution is obtained by two TKR sections, front and back. The front section is designed to exceed the angular resolution requirements, whereas the back section is designed to exceed the effective area requirement, improving the sensitivity at the high-energy end of the spectrum.

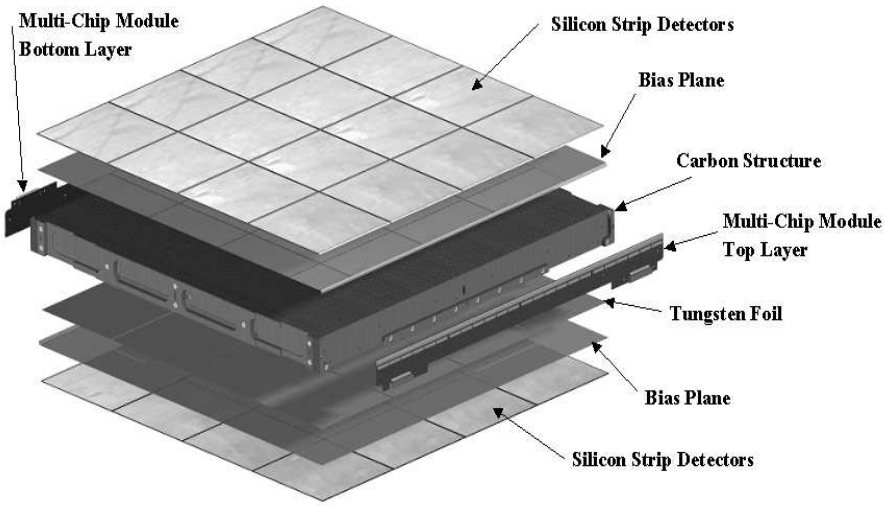

Fig. 3.7 - Schematic representation of a TKR tray assembly.

Each SSD sensor has 384 strips on a single side, with a pitch of 228 μm. Given the number of ladders, trays and towers in the TKR we obtain a total of $\sim 885,000$ channels.

3.6 The silicon sensors

LAT silicon SSD must be high-quality sensors, with a bad channel rate as low as possible and must be manufactured in huge quantities and delivered on a reliable schedule.

Parameter	**Specification**
Thickness	400 μm
Outer size	8.95×8.95 cm^2
Active area	8.76×8.76 cm^2
Strips per detector	384
Strip pitch	228 μm
R_{bias}	>20, <80 MΩ
$C_{interstrip}$ at 150 V, 1 MHz	<1.5 pF/cm
$C_{coupling}$	> 500 pF
Depletion voltage	< 120 V
Breakdown voltage	> 175 V
I_{leak} at 200 V	< 600 nA
Bad strips	<0.2%

Tab. 3.1 - GLAST LAT TKR SSD characteristics, from specifications [46].

The LAT TKR will employ $\sim 10,000$ SSD, for a total silicon surface of ~ 80 m^2. The

main requirements are listed in Table 3.1: sensors (and thus ladders) have 384 strips, meaning that in a TKR silicon plane there are 1536 strips, in a tower there are $\sim 55,000$ strips and the whole TKR will have $\sim 885,000$ channels. It is easily understood that quality and yield are crucial in an instrument of this size.

SSD were produced by Hamamatsu Photonics, a company used in dealing with devices for collider High Energy Physics experiments like CMS, and also SSD prototyping took place in HEP institutes. By the end of 2003, when 9452 sensors had already been delivered to the INFN for testing in Pisa, the rejection rate was only $\sim 0.6\%$, meaning that only 44 sensors were considered unacceptable, mostly due to high current (35%) or low breakdown voltage (39%) [47]. Ladder building and storage, entrusted to italian industrial partners (Mipot, G&A Engineering) proved similarly efficient: out of 513 tested ladders, only 12 were rejected ($\sim 2\%$), half of which due to high currents and the others due to structural damage, with an overall bad channel rate of $\sim 0.03\%$ [47].

3.7 TKR Front End ASIC

The TKR front-end employs a custom ASIC called GTFE (*GLAST LAT TKR Front End*) [48] [49]; this is a 64-channel amplifier-shaper, with single-threshold discrimination. The amplifier stage architecture was roughly modeled after the front-end amplifiers of the BaBar SVT readout chip [50]; however, to save power and match the GLAST bandwidth requirements, the active cascodes were replaced by simple cascodes and the number of the amplifying stages was limited to two.

Signals from the SSD strips are converted into voltages by charge-sensitive preamplifiers. This first stage integrates the charge with a time constant determined by the input impedance requirements and kept short relative to that of the second stage. Given the ~ 40 pF detector capacitance, about half of which is between strips, the input impedance of the preamplifier must be more than ~ 5 kΩ to avoid cross talk and the consequent loss of charge collection. This translates into a rise time of ~ 200 ns for the preamplifier output. Gain is determined by the 0.13 pF feedback capacitor, providing 37 mV per MIP, corresponding to a gain requirement of ~ 20 for the second stage and a gain-bandwidth product requirement of about 230 MHz for the preamplifier. The latter was achieved with a dominant pole at 150 kHz and a trasconductance for the input MOSFET of about 700 μS.

The amplifier is composed of a folded cascode amplifier, followed by a source-follower output stage; the schematic in Fig. 3.8, taken from [49], refers to the prototype amplifier stage developed at UCSC, later implemented in the GTFE ASIC. The first cascode with the input MOS is folded, i.e. the input transistor is a p-MOS instead of a n-MOS: this minimizes the power dissipation by allowing the input transistor to be biased with as little as 2 V, while the remaining part of the circuit is operated on a 5 V power supply. The bias current for the input MOSFET is set by an external resistor.

The amplifier must operate asynchronously, so a continuous baseline restoration is necessary. To this purpose the DC feedback network provides a current of up to about 100 pA to the slow differential amplifier in the input stage. The current source was not set to lower values to avoid excess sensitivity to process variations as observed in simulated circuits, and tests on early prototypes have been satisfactory. The noise induced by this small current is negligible when compared with the contributions from the input transistor

and the detector leakage current: detailed simulations indicate that the noise induced by the feedback network is 9% of that due to the input transistor alone.

A 46 pF capacitor allows charge injection for calibration purposes when charged by the CALIB_DAC signal, a digital step 512 clock cycles long[(2)]. Charge injection is enabled for the channels set in the CALIBRATION_MASK register.

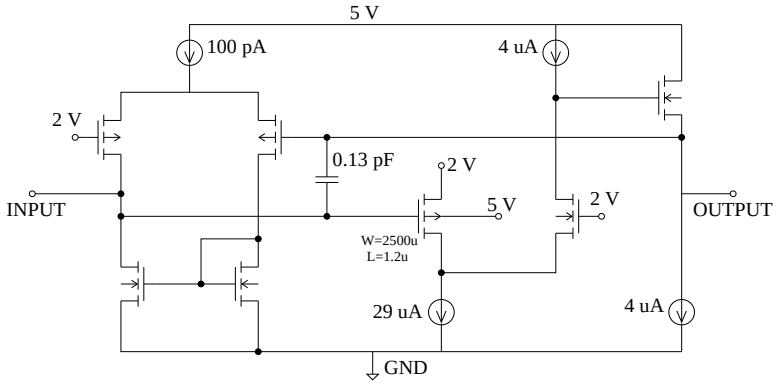

Fig. 3.8 - Design of the GTFE preamplifier stage; the 0.13 pF gain capacitor is easily seen in the center of the schematic, to its right the input MOSFET.

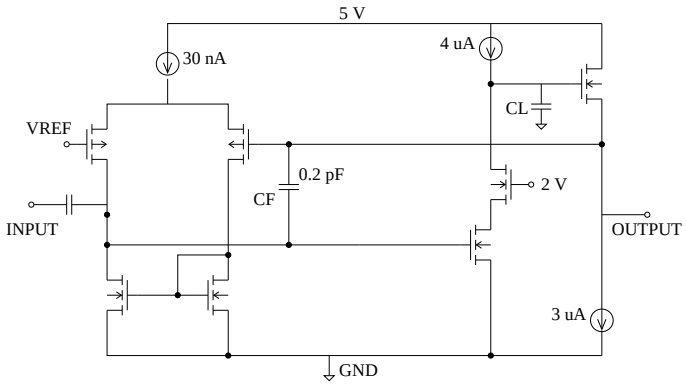

Fig. 3.9 - Design of the GTFE shaper; the signal from the preamplifier comes from the left through an input capacitance.

The preamplifier stage is AC coupled to the shaping amplifier, which is a cascode amplifier with a source-follower output, as shown in Fig. 3.9. The shaper is a simple RC-CR[(3)], with a gain–bandwidth product of 18 MHz and the principal pole at 20 kHz, adjusted to give a rise time of about 1.5 μs. The feedback scheme is modeled on that used in previous front-end chips, as SVX-II [51]. The differential amplifier, on the left side of Fig. 3.9, is used to adjust the operational point of the input transistor so that the output baseline remains fixed at the reference voltage: this is necessary as the shaper output is DC connected to the input of the threshold comparator.

The two-stage comparator is simply a differential amplifier followed by an inverting

(2) – the falling edge injects a pulse of the wrong polarity; hence the step length.

(3) – for pulse heights less than 1 fC; above this level the baseline restoration fails to give an exponential decay due to current limitations.

amplifier, where the threshold is generated by the threshold DAC, THRESH_DAC. The outputs of the two voltage generators are controlled by the DAC register: a bit sets the operational range (LOW or HIGH) for both and other 6 bits regulate the output; allowed values are reported in Table 3.2.

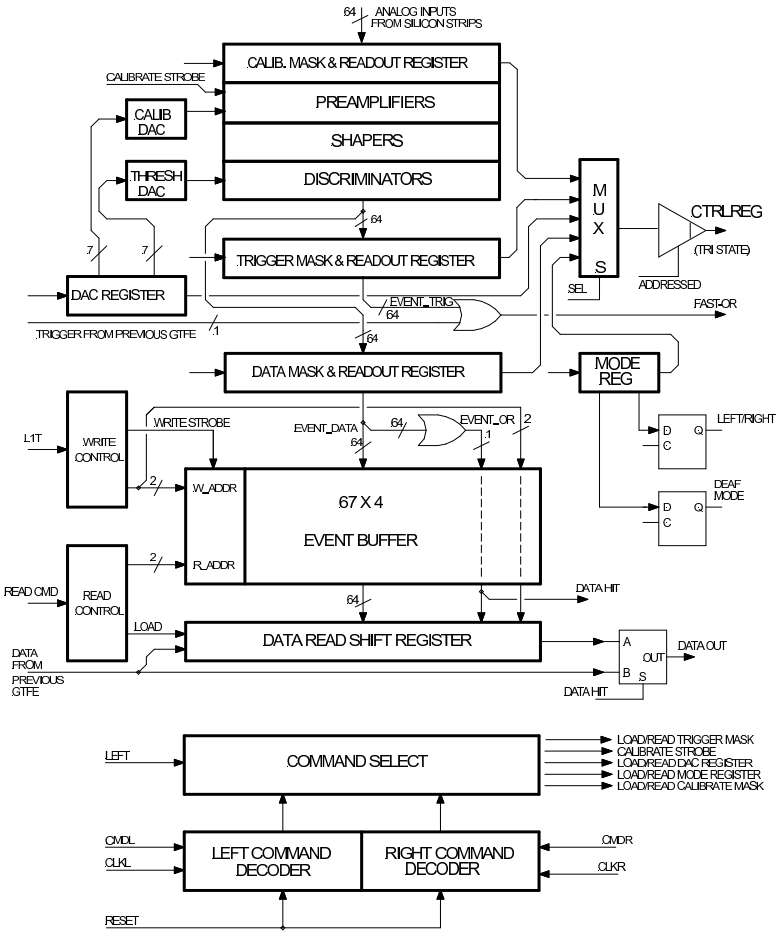

Fig. 3.10 - Block diagram of a GTFE ASIC [48]; this schematic refers to the prototype ASIC developed at UCSC.

To clarify the GTFE digital operations a functional block schematic of the ASIC is more useful, like the one shown on Fig. 3.10. The output of the discriminators is AND'ed with the contents of a TRIGGER_MASK to suppress the channels that are not allowed to take part in the trigger formation. The enabled channels are then OR'ed together and with the corresponding signal coming from the previous GTFE (if any) to form the FAST_OR signal, that is passed to the next GTFE (or to the GTRC if the GTFE is the last one). This way a fast, clock-independent, layer trigger is generated from the strip hits, having excluded the noisy channels in the TRIGGER_MASK.

The output of each channel from the discriminator is again AND'ed with the corresponding bit in the DATA_MASK register, used to suppress data generation for noisy channels. All channels are then OR'ed and if the result is a logical **1** all GTFE channels are read when a corresponding request comes from the GTRC.

When a L1T (TACK signal from the TEM) is received, event data are stored in the

four-deep event buffer; on the trigger line the buffer address is provided as two additional bytes after the trigger proper. Event data signals are not held if L1T is not issued; hence the trigger must be received before the shaper output falls.

CALIB_DAC	
Range (B6)	DAC_V (B0-B5)
0	$mV_{out} = 1.57 + 1.54 \times DAC\_V$
1	$mV_{out} = 15.0 + 14.6 \times DAC\_V$
THRESH_DAC	
Range (B13)	DAC_V (B7-B12)
0	$mV_{out} = 4.5 + 4.5 \times DAC\_V$
1	$mV_{out} = 12.9 + 12.9 \times DAC\_V$

Tab. 3.2 - GTFE DAC register bits and output voltages.

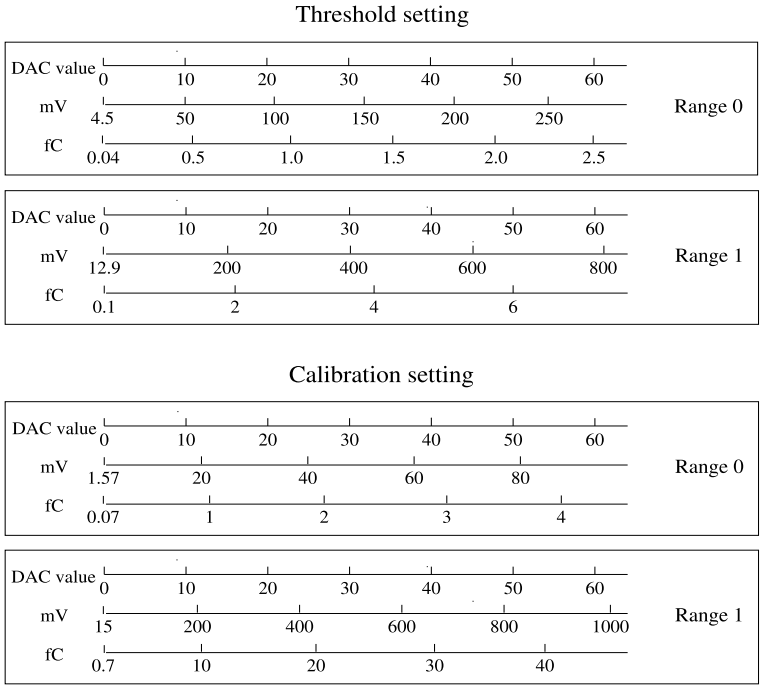

Fig. 3.11 - Conversion of threshold and calibration DACs into charge and voltage.

When a READ_CMND is received from the GTRC, event data are downloaded from the event buffer in a temporary holding register. If the OR of the channel data returns a **1** then event data are shifted out serially, otherwise data coming from the previous GTFE are forwarded.

Two shift registers and two command decoders are present, allowing operation from the left or right GTRC, thus providing redundancy and fault tolerance in the GTFE. The MODE bit in the two-bit MODE register selects leftward or rightward operation disabling one command decoder, while the DEAF bit disables reception of event data and trigger from the adjacent GTFE. A summary of the GTFE registers is shown in Table 3.3. Mask registers, listed as 64 bit long, are actually 68 bit-registers: every 16 bits a fixed **1** is present to ensure that no sequence of 32 **0**'s is issued, as the readout system recognizes

such a sequence as a data transfer terminator. In addition to the listed registers, 3 additional registers are present; they are used for reading out the corresponding mask register (CALIBRATION,TRIGGER,DATA).

Register ID	Depth (bits)
CALIBRATION_MASK	64
TRIGGER_MASK	64
DATA_MASK	64
DAC	14
MODE	2

Tab. 3.3 - Internal GTFE registers and their bit depth.

3.8 GLAST TKR Readout Controller ASIC

The *GLAST TKR Readout Controller* (GTRC) takes care of the intercommunications between GTFEs and the TEM.

GTRC Control Register Format			
Bit	Name	Definition	Default
33	LD_FT	Enable loading FORCE and TOT bits	
32	LD_DELAY	Enable loading READ_DELAY	
31	LD_STRETCH	Enable loading STRETCH	
30	LD_CNT	Enable loading GTFE_CNT	
29	LD_SIZE	Enable loading SIZE	
28	SUM_ERR	Read only Logical OR of TAG, TRIG, DAT and CMD errors	
27	CMD_ERR	Read only Sum Cmd Parity Error	
26	DAT_ERR	Read only Sum Data Parity Error	
25	TRIG_ERR	Read only Sum Trigger Parity Error	
24	TOK_ERR	Read only Sum Token Parity Error	
23	TAG_ERR	Read only Sum Tag Error	
22	SHIFT_MODE	Read only. Bonded pad to determine side	
21	TOT_EN	1 => Enable TOT Delay	1
20	FORCE_NO_ERR	0 => Normal operation 1 => Forces Normal Event readout	0
[19..17]	READ_DELAY	Delay from Read Event to start of Read Command in 6.4us steps	0
[16..12]	OR_STRETCH	Fast-OR Stretch in 50ns steps.	10
[11..07]	GTFE_CNT	Number of GTFE chips to read	12
[06..00]	SIZE	Number to set maximum number of hits from GTFE	64

Tab. 3.4 - GTRC configuration register contents, from [52]; bits are ordered MSB first, as they appear in the data field in GTRC commands.

Two configuration registers are present: the 5 bit SYNC register stores a number controlling the synchronization between GTRC and GTFEs, while the CTRL register contains several parameters controlling GTRC configuration, error bits and control bits, as shown in Tab. 3.4. The first 22 bits are used to store the configuration: they specify the number

of GTFE present in the MCM, the maximum number of hits the GTRC can receive and other operational details. As they are the only bits that can modify the chip functionalities and are writable, they are the ones relevant for functionality tests; this part of the CTRL register is treated in the rest of this work as if it were a register in itself, labeled CONF. The next bit (#22) determines the GTRC side (left=1). The next five bits are read only error bits, that are set to 1 whenever the corresponding error arises and are reset to 0 after this CTRL register is read. The following bit, #28, is the logical OR of all error bits: it is set to 1 whenever any error arises. The last 5 bits are used to make writable specific bits of the configuration part. In GTRC version 6 and later other 4 read only bits are present, where the ASIC version number is stored.

Register ID	Depth (bits)
CONF	22*
SYNC	8

Tab. 3.5 - Internal GTRC registers and their bit depth. *These are the bits where the configuration is stored, special bits are not included; more details in Sect. 3.8.

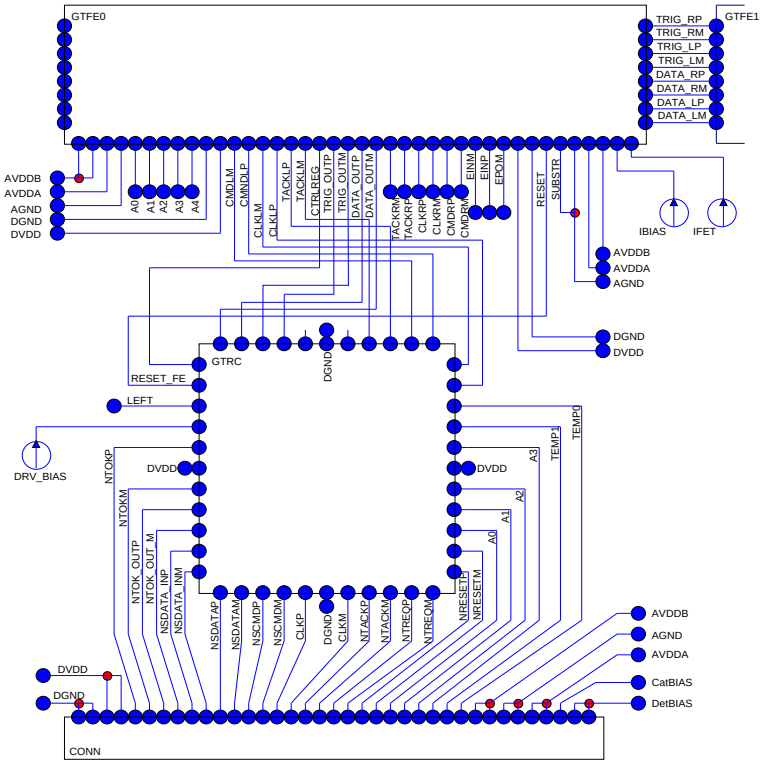

Fig. 3.12 - A schematic of MCM connections between the left GTRC and GTFE #0 and #1.

A simplified block schematic is shown on Fig. 3.13. The IO control decodes commands received from the TEM and send them (when appropriate) to the GTFEs. Furthermore, it synchronizes data transfer with the other layers.

When a READ_EVT signal is received, the contents of a data buffer are downloaded from the selected GTFE and stored into one of the two GTRC event buffers. Each GTRC

can store a maximum of 64 channels: a greater strip multiplicity in a single event is not expected. When a TOKEN signal is received, the event data from the selected buffer are sent serially to the TEM, and the TOKEN is forwarded to the GTRC of the next layer.

When enabled by the corresponding bit in the CTRL register, the 10 bit Time-over-Threshold (TOT) counter measures the time that the GTFE layer OR remains set (i.e. the time that at least one channel in the plane is above threshold). It is started by the L1T trigger acknowledge signal (TACK) from the TEM. The time the amplified signal remains over a set threshold is proportional to the charge injected into the preamplifier: this allows for a reconstruction of the energy released in the SSD without the need for an analog readout.

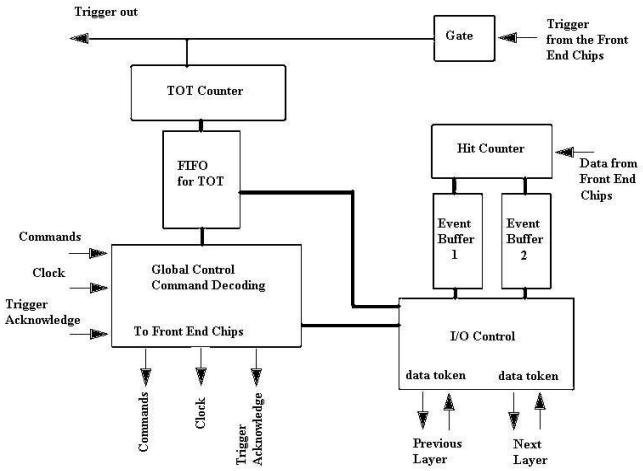

Fig. 3.13 - Simplified functional block diagram of a GTRC.

Fig. 3.14 - Picture of a mini-MCM (see Chap. 7) during assembly; only the left GTRC and the first two GTFEs are in place.

3.9 GLAST TKR Multi-Chip Module

The TKR ASICs are placed on a Multi-Chip Module (MCM), an 8-layer Aramid PWB with Nanonics cable connectors and with the necessary discrete electronics. Each MCM carries 24 GTFE's connected in daisy-chain, and two GTRC, one for each side. A schematic representation of an MCM is shown in Fig. 3.12; the most relevant connections are shown, together with the outgoing left connector. The GTFE pads labeled A0-A4 are used to encode the chip ID from 0 to 23. The corresponding pads on the GTRC (A0-A2)

are routed to the outgoing connector: the GTRC ID (*layer ID*) are hardcoded into the flex cables: the layer closest to the TEM is always labeled 0, the farthest is always the 9.

The MCM provides the necessary bias currents for current mirrors (I_BIAS), for input transistors (I_FET), and for LVDS drivers (DRV_BIAS). Power is supplied by the cable connection: required power lines are the DVDD (2.5 V) for digital operation, and AVDDA (1.5 V) and AVDDB (2.5 V) for analog functionalities.

TKR MCMs are attached to the tower sides and GTFEs are bonded to the SSD planes with the help of a quarter-cylinder "pitch adapter" (1-layer flex circuit), as shown on Fig. 3.15.

Smaller versions, called miniMCMs and hosting a maximum of 7 GTFEs, have been developed to be used as test boards; a photograph of one of these during assembly is shown in Fig. 3.14. We employed such simplified modules for the radiation tests described in Chap. 7.

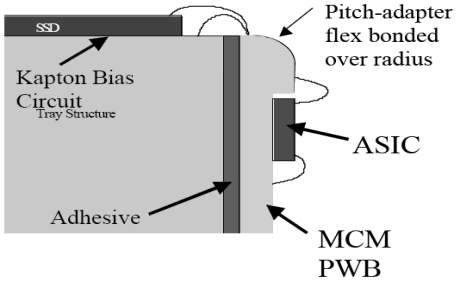

Fig. 3.15 - Lateral view of a MCM on the side of a TKR tray; the wire bonds between a GTFE and the SSD are shown.

3.10 GLAST Cable Controllers

The *GLAST Tracker Cable Controller* (GTCC) and the *Calorimeter Cable Controller* (GCCC) are the two custom ASICs present in the TEM [53] [54]. Their basic function is the interface between the common logic of the TEM and the TKR and CAL electronics. GTCC and GCCC are digital chips with Low Voltage Differential Signaling (LVDS) inputs and outputs interfacing to the TKR and CAL readout controllers and 3.3 V CMOS interfacing to the logic on the TEM. The ASICs are fabricated using the 0.5 μm Agilent CMOS process.

Name	Width	Access	Description
CONFIGURATION	32	R/W	Configuration and setup
INPUT_MASK	32	R/W	Input masking
FIFO_STATUS	32	R	Latched FIFO signals
LATCHED_STATUS	32	R/W	CSR latched values
EVENT_TIMOUTS	32	R/W	Event timeouts
TRG_ALIGNMENT	32	R/W	Trigger input alignments and delays

Tab. 3.6 - GTCC registers, their size and a short description, as found in [53].

Two GTCCs and a GCCC are placed on each of the 4 sides of the TEM, where the two

flex Kapton cables are connected. Each GTCC manages the 9 TKR layers connected to the cable it accesses (see Fig. 3.6 for a schematic); in a similar fashion each GCCC serves the four layers of one CAL side.

The internal structure of registers and FIFOs and the ASIC functionalities are rather complicated, and well beyond the scope of this section. To our purposes it suffices to say that a cable controller is a big FSM[4] managing event readout, data buffering, data flow, and trigger propagation between CAL and TKR readout controllers and the TEM. Several registers and FIFOs are contained in each, although not all bits can be used and/or written. We here summarize the storage capabilities of each ASIC, as the number of bits it contains is proportional to its susceptibility to radiation effects affecting the digital operations during space operations (see Chap. 5).

The GTCC passes commands from the TEM Common Controller to the GTRC ASICs connected to the cable it serves. It contains six 32-bit registers, shown in Tab. 3.6, and five FIFOs used to store diagnostics, errors and data, as shown in Tab. 3.7. More details can be found in [53].

Name	Width	Containts
Summary FIFO	64x16	Summary of event
Data FIFO 1	128x16	Event data
Data FIFO 2	128x16	Event TOT
Error FIFO	128x16	Error flags
Diagnostic FIFO	64x16	Trigger diagnostics

Tab. 3.7 - GTCC FIFOs, their size and a short description, as found in [53].

The GCCC passes commands from the TEM Common Controller to the GCRC ASICs connected to its CAL cable. It contains seven 32-bit registers, shown in Tab. 3.8, and five FIFOs similar to those the GTCCs employ described above. More details can be found in [54].

Name	Width	Access	Description
CONFIGURATION	32	R/W	Configuration and setup
LAYER_MASK_0	32	R/W	Layer mask (low-order numbered layer)
LAYER_MASK_1	32	R/W	Layer mask (high-order numbered layer)
FIFO_STATUS	32	R	Latched FIFO signals
LATCHED_STATUS	32	R/W	CSR latched values
EVENT_TIMOUTS	32	R/W	Event timeouts
TRG_ALIGNMENT	32	R/W	Trigger input alignments and delays

Tab. 3.8 - GCCC registers, their size and a short description, as found in [54].

[4] – FSM: Finite State Machine, a digital system with actions associated with states and transitions between states.

3.11 GLAST LVDS Translator Chips

The *GLAST LVDS Translator Chip* (GLTC3) is part of the Global Trigger (GLT) subsystem. It serves as an interface between the ACD and the GLT subsystem. It converts the LVDS trigger outputs of the ACD into CMOS signals that can be used by the GLT. An additional masking step allows to turn off the CMOS output; the mask data is provided by the GLT. The LVDS to CMOS conversion takes place via the 18 LVDS receivers. The LVDS input is active low (LVDS standard); the mask bit enable must be high to enable the output to change with the input.

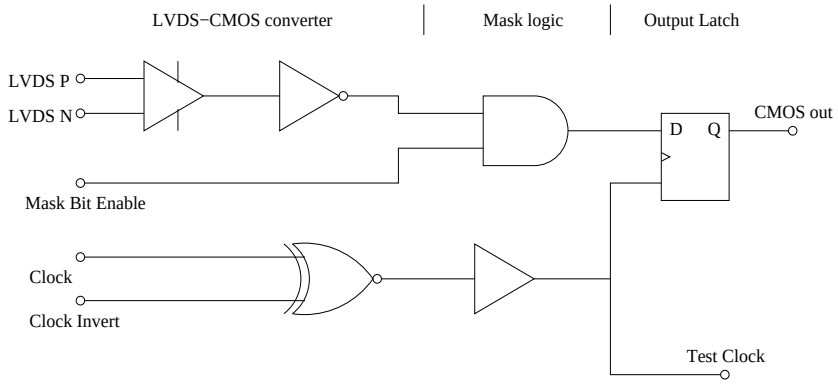

Fig. 3.16 - GLAST GLTC level conversion circuit, from [55].

4 Radiation Environment

Before investigating the radiation-induced effects the LAT electronics will be exposed to, in this chapter an overview of the space radiation environment is given; in particular the more specific characteristics along the GLAST orbit are given. More details are available, for example, in [56], [57] and references therein.

4.1 The space radiation environment

Our planet is surrounded by a radiation rich environment, consisting of mainly energetic charged particles (electrons, protons, heavy ions). They can either be trapped particles, bound to trajectories dictated by the earth's magnetic field, or free, transiting particles.

Particle Type	Maximum Energy
Trapped Electrons	10s of MeV
Trapped Protons & Heavy Ions	100s of MeV
Solar Protons	GeV
Solar Heavy Ions	GeV
Galactic Cosmic Rays	TeV

Tab. 4.1 - Maximum energies of particles in the space radiation environment, from [57].

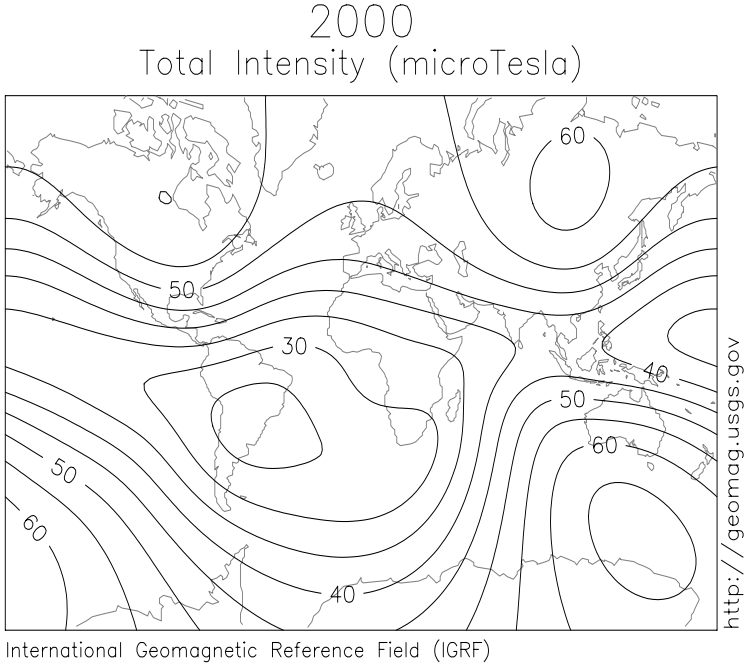

Fig. 4.1 - Earth magnetic field intensity, year 2000 at sea level; the inclination and the location of the South Atlantic Anomaly are clearly visible.

Most of the particles in interplanetary space come from the sun in the form of a hot ionized gas called the *solar wind*; it flows radially from the sun with a speed that in

proximity of the Earth varies from about 300 to 1000 km/s, and represents a solar mass loss of about 10^{14} kilograms per day. The origin of cosmic rays coming from outside the solar system, the hardest component of the space radiation spectrum, is controversial. Particles from outside the solar system are affected by the solar wind: cosmic rays are scattered by the "magnetic scattering centers", i.e. by the charged particles carried along by the radially moving solar wind. The cosmic ray spectra in interstellar space can be modeled in terms on the particle rigidity as

$$f(E_k) = A \times R(E_k)^{-a}. \tag{4.1.1}$$

The magnetic rigidity R depends on the ion kinetic energy E_k and on its charge Q (in terms of the proton charge) as

$$R(E_k) = (A/Q)\sqrt{E_k^2 + 2ME_k} \tag{4.1.2}$$

where M is the atomic mass unit.

This spectrum expression, valid in interstellar space, is modulated by the solar activity: this corresponds to a shift in energies depending on the intensity of the solar wind. In [58] this is modeled as

$$f^\star(E_k) = f(E_k) \times \frac{(E_k + Mc^2)^2 - (Mc^2)^2}{(E_k + Mc^2 + Ze\phi)^2 - (Mc^2)^2}$$

where Z is the particle atomic number and the parameter ϕ represent the solar modulation as a critical rigidity, ranging from $\sim$ 550 MV[(1)] (solar minimum) to $\sim$ 1100 MV (solar maximum).

Earth's magnetic field, generated by the convective motions in the molten nickel-iron core, can be approximated to that of a dipole: earth's magnetic dipole is about 320 km from the center of the planet, inclined at an 11.5° angle from the planet's rotational axis. Due to the dipole geometry, the magnetic field intensity is lowest over Brazil, and in this region, *South Atlantic Anomaly* (SAA), $\sim$ 300 to $\sim$ 1200 km wide, the concentration of charged particles is highest (see Fig. 4.1). A slow movement of the south Atlantic anomaly as a result of shifts in the geomagnetic field has been observed. This shift is essentially westward at a rate of 0.3° per year and it must be taken into account when planning operations in low Earth orbits lasting a considerable amount of time (several years).

A cosmic ray will be deflected by the earth's magnetic field if its magnetic rigidity is small enough. At a given altitude and latitude there is a minimum rigidity which a cosmic ray must have to reach that point and avoid being deflected: this is called the *geomagnetic*

(1) – rigidity, being the particle energy divided by its charge, is measured in megavolts (MV) and gigavolts (GV).

cutoff value. Assuming a dipolar shape, the cutoff rigidity is a function of the altitude h and of the geomagnetic latitude θ_M:

$$R_{\text{cut}} = 14.9 \times \left(1 + \frac{h}{R_\oplus}\right)^{-2} (\cos\theta_M)^2 \quad \text{GV} \tag{4.1.3}$$

where $R_\oplus$ is the Earth radius [59].

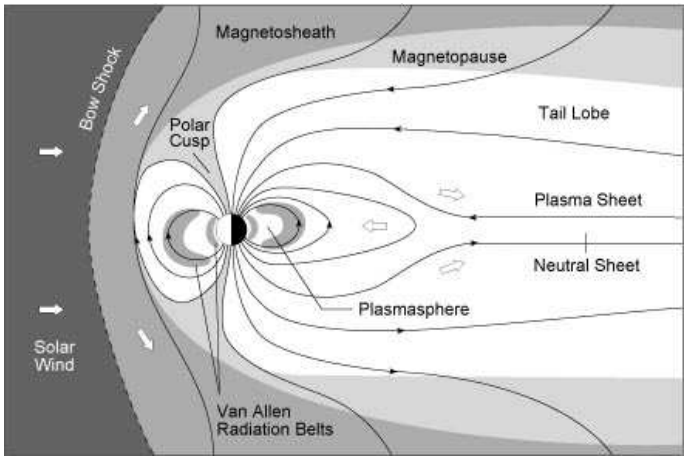

Fig. 4.2 - Interactions between Earth magnetosphere and the solar wind, from [60].

4.2 Trapped particles

The sun heavily distorts the magnetosphere at distances larger than ~ 5 earth radii: the effect is similar to that of the hydrodynamic shock-wave of a spherical body moving through a fluid: the magnetic field lines on the dayside are heavily compressed and a bow shock forms, while they disperse in the nightside, where a plasma tail elongates (see Fig. 4.2). Charged particles (protons, electrons) gyrate around field lines at an appropriate Larmor frequency as shown in Fig. 4.3; in addition gyrating particles experience an overall Lorentz force that makes proton drift westward, while electrons drift eastward. If the mirror points, where the closing in of the field lines repels the particles, are high enough, the particles remain inside the region known as *Van Allen belts*; otherwise they hit the atmosphere and are lost. The altitude of the Van Allen belts is not constant due to the dipole field anomalies: the lowest altitude is ~ 200 km above sea level (asl) on the SAA, then altitude rapidly increases up to ~ 1000 km asl.

The electron environment consists of particles up to 7 MeV, and shows two flux maximums, referred as the *inner* and *outer zone*. The inner zone is located at about $15,000$ km asl and the outer zone extends from $\sim 18,000$ to $\sim 76,000$ km asl; in the outer zone the most energetic electrons are contained [56].

The proton flux varies with distance from earth inversely with energy, the outer boundary being at $\sim 24,000$ km asl.

Trapped particle fluxes are extremely sensitive to the changes in the geomagnetic field induced by solar activity. Satellite measurements have shown that the main periodic

fluctuations are the day-night cycle and the 11-year solar activity cycle. An important solar-induced modulation, particularly relevant in the case of protons, occurs during the active phase of the solar cycle, when the increased energy carried by the solar wind causes the Earth's atmosphere to expand, so that between 200 and 1000 km its density increases. This increase depletes belts for which mirror points are normally above the critical height, reducing significantly the exposure of satellites orbiting at lower altitudes.

Most of the scientific instruments flown in the late 1950s and early 1960s were designed to detect energetic protons and electrons. A general understanding of the near-Earth radiation environment was obtained but differences up to a factor of 10 appeared when making quantitative comparisons between different experiments. Quantitative models of inner-zone protons and electrons, designated P1, P2, etc. and E1, E2, etc. were developed by the NASA's Space Flight Center.

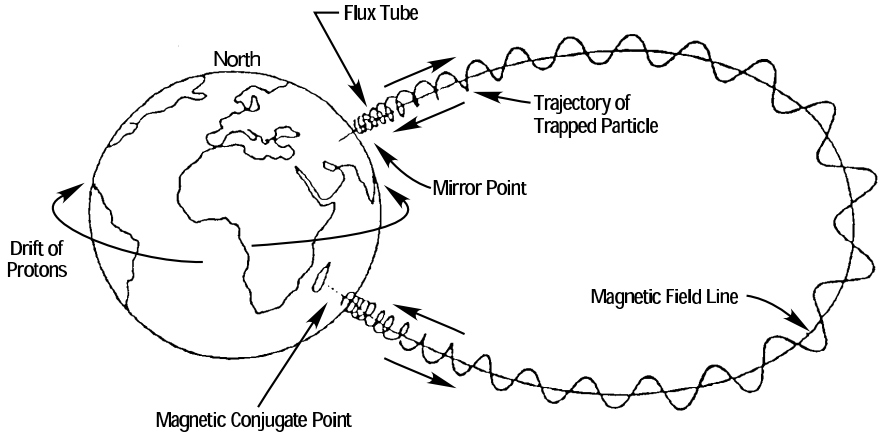

Fig. 4.3 - Motion of trapped particles along field magnetic lines [61].

New models were presented at the 1965 NSREC conference [62] called AE-1 and AP-1 respectively, taking advantage of the results of several groups actively involved in trapped particle measurements. A major problem of such models was the scarce knowledge of the natural condition of the inner electron zone, as the 1962 Starfish Prime US nuclear test, which resulted in a 1.4 megaton detonation at $\sim$ 400 km, released 10^{29} fission electrons with energies up to 7 MeV into the magnetosphere: fluxes in the inner Van Allen belt increased at least by a factor of 100[(2)]. The Starfish electrons dominated the inner zone environment for five years; effects were observed out to 5 Earth radii.

Eight trapped proton models, eight trapped electron models and a Starfish decay model were released in the next 27 years. The AP-8 model [63], released in 1976, includes all previous models under a common approach. Similarly, the AE-8 model [64], extending the picture to electrons, was completed in 1983. The AP-8 and AE-8 models include data from 43 satellites, 55 sets of data from space instruments, and 1630 channel-months of data.

In March 1991 the *Combined Release and Radiation Effects Satellite Program* (CRRES) mission observed the largest magnetic event ever recorded. CRRES observations include

(2) – the enhanced radiation levels and the consequent failures of seven satellite-borne missions in the months following the Starfish detonation strongly prompted the study of radiation hardening techniques beyond simple redundancy

large redistributions of protons after the 1991 event, involving the creation of a new proton storm belt [65].

Analysis of the CRRES data show that AP-8 and AE-8 models, with their four to six year averages, are inadequate to account for events characterized by short duration, and in any case anomalous events like the one of March 1991 are impossible to predict or quantify. Several models exist or are being developed, featuring an improved time resolution (see [57] for a review); it must be considered that setting space mission requirements involves uncertainties that are hard to assess, especially for short term effects, such as interference and data corruption.

4.3 Solar Cosmic Rays

Solar cosmic rays originate in solar particle events (SPE), usually associated with solar flares [56]. During energetic events on the sun, large fluxes of energetic particles are produced which can reach the Earth. Large events are confined to a 7-year period defined as *solar maximum*. Although large events are absent during the remaining 4 *solar minimum* years of the 11-year solar cycle the occasional small event can still occur.

SPE bursts are composed mainly of protons, with a minor contribution of α particles, heavy ions and electrons. The particles arrive at the earth in times ranging from tens of minutes up to several hours, depending on their energy and the point of origin on the sun surface, peaking within two hours to one day; the most energetic protons arrive in 10—30 minutes. During major solar events the flux of heavy ions, usually well below the galactic background, can rise above it and have significant impact on radiation damage calculations.

The August 1972 event produced a peak flux near the Earth in excess of 10^6 protons $\mathrm{cm}^{-2}\mathrm{s}^{-1}$ with energy above 10 MeV, while the October 1989 event produced a peak flux of about 10^5 protons $\mathrm{cm}^{-2}\mathrm{s}^{-1}$. A fluence spectrum which is often used to represent a worst-case flare, classified as "anomalously large" is based on the very large August 1972 event [66]:

$$J(E) = 7.9 \times 10^9 \exp\left(\frac{30 - E}{26.5}\right) \tag{4.3.1}$$

where E is the proton energy in MeV and J the fluence in protons/cm^2. The October 1989 event was the largest seen since August 1972 but had lower fluences at the medium energies. A fit to its *differential* fluence spectrum is given by a three-part power law [66]:

$$j(E) = \begin{cases} 1.2 \times 10^{11} \cdot E^{-1.7} & \text{for } E < 30 \text{ MeV} \\ 4.5 \times 10^{12} \cdot E^{-2.8} & \text{for } 30 \text{ MeV} < E < 150 \text{ MeV} \\ 5.5 \times 10^{9} \cdot E^{-1.45} & \text{for } E > 150 \text{ MeV} \end{cases} \tag{4.3.2}$$

where E is in MeV and j is in protons cm^{-2} MeV^{-1}.

As can be seen from the expressions above, flare spectra are variable, and therefore the worst-case event at one energy is not necessarily worst-case at another. While the August 1972 event gave worst-case doses at medium energies, the October 1989 flare was more

severe at lower and higher energies. The latter are more important for nuclear interactions giving rise to certain types of background and single-event radiation effects (see Chap. 5), so the term "worst-case" is application dependent.

For analyzing ion-induced single-event rates during SPEs, the CREME96 model [67] is used. It can also be used for other applications where data on severe SPE conditions are needed, such as background estimation. CREME96 contains models based on the October 1989 event. It provides models of energy spectrum, composition and ionizing capabilities for the worst week, worst day and peak 5 minutes. The older CREME model provided more choice of peak environments; however, some of the more severe options were unrealistic. Fluxes and fluences of solar energetic particles are assumed to be isotropic in interplanetary space. This may not be true in near-Earth space due to geomagnetic shielding.

4.4 Galactic Cosmic Rays

Galactic cosmic rays (GCRs) come from the diffuse radiation background that uniformly fills the galaxy around the solar system [56]. They consists of $\sim 85\%$ protons, about 14% α particles and $\sim 1\%$ heavier nuclei. GCRs reach energies above 10 GeV/amu; towards lower energies their flux is decreased due to the influence of the solar wind and the geomagnetic field.

Cosmic-Ray environment and effects models were originally created under the name CREME [68]. They provided a comprehensive set of cosmic ray and flare ion energy spectra, including treatment of geomagnetic shielding and material shielding. CREME also included upset rate computation based on the path-length distribution in a sensitive volume and also treated in a simple manner trapped proton-induced single-event effects. CREME has been superseded by CREME96 [67]. The major differences are the inclusion of a model of the cosmic ray environment and its solar-cycle modulation, improved geomagnetic shielding calculation, improved material shielding calculation and more realistic SPE ion environments. Cosmic ray fluxes are anti-correlated with solar activity so the highest cosmic ray fluxes occur at solar minimum. CREME96 is the standard model for cosmic ray environment assessment. It is also the standard tool for evaluation of SEE from cosmic rays, from solar energetic particles and from energetic protons.

4.5 Neutrons

A low-level flux of neutrons of between 0.5 $\mathrm{cm^{-2}s^{-1}}$ and 4 $\mathrm{cm^{-2}s^{-1}}$ is present at lower altitudes due to cosmic ray interactions with the atmosphere. Neutrons are also generated by energetic particles undergoing strong interactions with the material of the spacecraft. While these neutrons are particularly relevant for manned missions due to radioprotection issues, they also play a role in generating background in sensitive detector systems.

4.6 GLAST environment

GLAST will be in a circular low earth orbit (LEO), at an altitude of 565 km and an inclination of 28.5° [69], corresponding to an orbital period of ~ 1.6 hrs. The instrumentation will be shielded from a large portion of the space radiation. The orbit will, however, intersect the South Atlantic Anomaly (SAA) which will give the most important contribution to total dose. The vertical cutoff in the GLAST orbit varies from ~ 15 GV down

to around 4 GV at +28° latitude and 285° longitude. This implies a minimum cutoff of 3.17 GeV for protons and 1.27 GeV/amu for nuclei with A/Z=2.

In order to assess particle fluxes and Linear Energy Transfer (LET) spectra during the LAT lifetime, simulations have been performed by the investigators for the experiment proposal [39] (see Sect. 5.2 for the methods of describing the energy deposition due to ionizing radiation). The spectra of cosmic ray nuclei from free space are well represented by the CREME96 model. Charged albedo particles near the Earth secondary products made in collisions of cosmic rays with the upper atmosphere were considered: this important component is not included in the CREME model. Nonetheless, the fluxes are known from the early days of space observations [70], and have been explained by theoretical modeling [71]. Recent measurements made by AMS give a detailed characterization as a function of latitude [72]. These fluxes are all built into a simulation package needed for the LAT for background rejection.

Electrons are not included in the CREME model. Although 100 times less abundant than protons, a simplified model based on balloon observations [73] was included in the simulations.

Charged particle radiation estimates were first summarized in [74]. Those estimates were used to calculate the expected radiation fluxes and the dose levels the LAT will withstand. The outer silicon elements of the tracker are expected to receive a maximum total dose of ~ 0.8 krd in a 5-year mission. For single-event effects issues we will consider GCR and SPE, taking into account the LET at the surface of silicon. For GCR we can estimate an upper energy cutoff at around 28 MeV$\times$cm^2/mg, while for SPE the limit is about 100 MeV$\times$cm^2/mg. Above 8 MeV$\times$cm^2/mg, the relevant threshold LET for single-event validation [69], we estimate a worst case scenario by multiplying the maximum possible particle flux in the planned 5 years of operation by the total mission time, obtaining $\sim$0.2 ions/cm^2 due to GCR and < 0.1 ions/cm^2 due to SPE in 5 years.

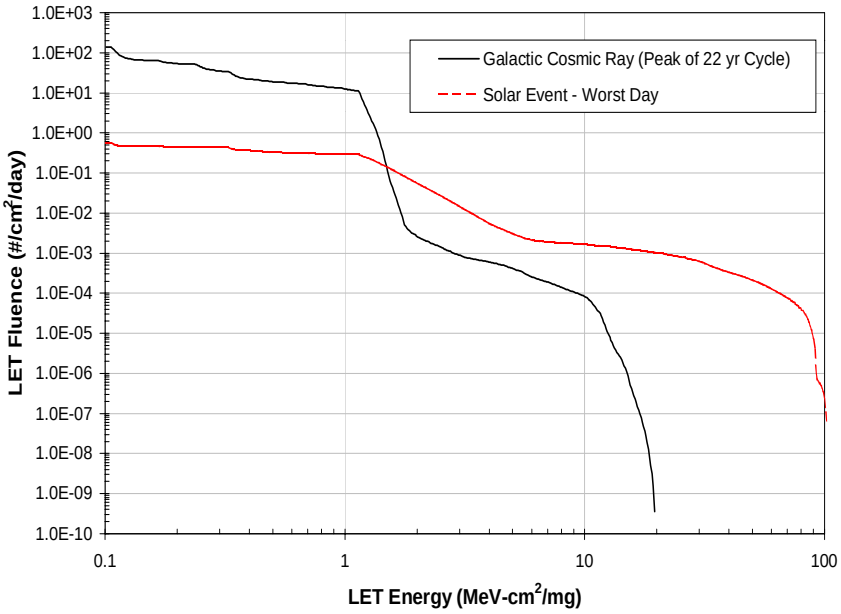

Fig. 4.4 - Integral LET spectrum in silicon, CREME96 simulation for GLAST orbit, 5 year mission and 100 mils Al shielding, from [74].

5 Radiation Damage and Tolerance

Having seen in Chap. 4 the characteristics of the environment GLAST will operate in, in this chapter an overview of the effects of ionizing radiation on integrated circuits (IC) is given, with special attention to MOS structures like those employed in LAT electronics. A summary of the effects more dangerous for the GLAST operation is presented, and mitigation techniques are addressed.

The physical interactions and processes that radiation induces in matter may lead to the modification of electrical properties and degradation of the electronic performance of an exposed device. The main effects are due to charge deposition in the form of ionization [75], even though in some cases atomic displacement plays a role. Ionizing effects can be subdivided further into *Single Event Effects* (SEE) and *Total Ionizing Dose Effects* (TID). As TID radiation validation is much less straightforward that SEE validation, Chap. 6 will deal with greater detail with the procedures involved.

5.1 Displacement Damage

Displacement damage is relevant for bipolar transistors and silicon rectifiers that require a high (and stable) minority-carrier lifetime for efficient operation; majority-carrier devices like FETs are less sensitive to such parameters. The damage process is characterized in the first place by the displacement of a *primary knock-on atom*, giving rise to a interstitial silicon and a vacancy (a *Frenkel pair*). The silicon displacement requires about 25 eV [76]; considering an elastic scattering, the maximum kinetic energy of the recoiling silicon ion is given by

$$E_{R,max} = 4E_I \frac{m_I m_{Si}}{(m_I + m_{Si})^2} \tag{5.1.1}$$

where m_I is the mass of the impinging particle and E_I is its kinetic energy. Hence, the minimum energy necessary to create a Frenkel pair is 185 eV for neutrons and 255 keV for electrons (for which the relativistic correction of Eq. 5.1.1 is used). The recoil silicon atom itself can displace other atoms and give rise to regions with a high concentration of defects, called *clusters*; the threshold for cluster generation is 35 keV for neutrons and about 8 MeV for electrons[(1)] [76].

Frenkel pairs are intrinsically unstable: the silicon atom falls easily into the vacancy potential well and recombines. Numerical simulations [77] show that 60% of Frenkel pairs recombine in the first 10^{-10} s, with peaks of 90% recombinations in clusters. Remaining vacancies and interstitials separate due to their different mobilities and, interacting with themselves and with impurities normally present in the silicon bulk, form stable defects that act as electrical active centers, interfering with carrier mobilities.

Due to the particular structure of VLSI electronics, where a thin active layer (~ 1 μm) is placed on top of a high-purity layer grown on a thick substrate with little or no influence

(1) – the recoil Si atoms must gain enough energy in the collision to produce further displacement.

on device operation, displacement damage is usually secondary and has little relevance in space operating electronics. The biggest impact is on SSD sensors, where *leakage current*, operating voltage and therefore power consumption are strictly dependent on the bulk defects. The fluxes of particles giving rise to displacement damage are rather low for the GLAST TKR and no problems are foreseen [78].

5.2 Radiation and Energy Deposition

Energy deposition in a medium by radiation can be quantified in different ways, depending on the effects one is interested in.

Deposited energy depends strongly on the energy of the passing particle. It is described by the *Linear Energy Transfer* (LET) defined as the energy deposited per unit length along the particle track and has dimensions of MeV mg^{-1} cm^2. Energy can be converted into deposited charge once the ionization potential for a given material is known: in Silicon the conversion is particularly easy: a LET of ~ 100 MeV mg^{-1} cm^2 corresponds to a charge deposition of 1 pC/μm[(2)], while a MIP deposits ~ 0.01 fC/μm.

LET is extremely useful in describing heavy ions that leave behind a heavily ionized column as they cross a material medium, a process described by Eq. *A*1.17 in App. *A*1. If the particle energy is not high enough so that the energy deposition is uniform through the hit device, one must keep in mind that LET is a function of the particle momentum and it varies as the particle loses energy according to an effective Bethe-Bloch: for heavy particles (such as protons, alphas, heavy ions, not electrons) stopping inside a material, the LET profile versus depth presents a Bragg peak at the maximum achievable depth (Fig. *A*1.3); i.e. such particles have a well defined range of penetration. An useful rule of thumb is that the maximum LET (in MeV mg^{-1} cm^2) measured in correspondence of the Bragg peak is roughly equal to the ion atomic number Z. On the other hand, the LET in the surface layers of a medium, such as in the relatively shallow electronically active volumes of CMOS devices, can be selected by carefully choosing an ion species and its energy.

When the energy deposition is uniform, or it can be considered uniform in the volumes under study within appropriate time scales, it is customary to speak of *dose*, defined as the amount of energy released per unit of mass. The *Gray*, defined as

$$1 \text{ Gy} = 1 \frac{\text{J}}{\text{kg}} \tag{5.2.1}$$

is the SI unit for dose, but in many application the *Röntgen absorbed dose* (rad) is used, where 1 Gy = 100 rd. Radiation effects are described in terms of absorbed dose for example in the case of silicon oxide degradation, as the small oxide dimensions ensure that passing particles release energy uniformily.

Assuming an uniform irradiation of a planar target and measuring the angle θ of incidence of the beam from the normal to the surface, we can derive the expression of the

(2) – more precisely: 97 MeV mg^{-1} cm^2 = 1 pC/μm.

surface dose as a function of the particle fluence Φ:

$$D(\text{krd}) = 1.6 \cdot 10^{-8} \times \text{LET}\left(\text{MeV cm}^2/\text{mg}\right) \times \Phi\left(\text{cm}^{-2}\right) \times \frac{1}{\cos(\theta)} \tag{5.2.2}$$

5.3 Ionizing Damage: Total Dose Effects

The undesirable effects of ionization arise when charge is produced in a dielectric, a medium that is supposed to block charge transport. While charge motion persists only for a short time (usually while the excitation lasts), *long lived effects* resulting from charge displacement can give rise to charge buildup and/or chemical alteration of sensitive structures, like semiconductor/conductor interfaces in MOS structures.

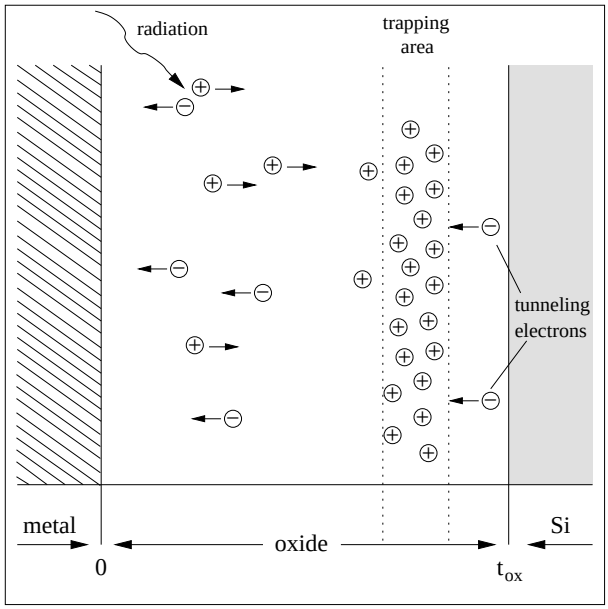

Fig. 5.1 - Radiation-induced holes are trapped at the silicon-silicon oxide interface.

The energetic cost to generate an electron-hole pair in silicon oxide is 17 ± 1 eV [79]; this allows us to calculate the charge pair density per rad generated by ionizing radiation, $g_0 = 8.1 \times 10^{12}$ pairs/(cm^3 rad). At room temperature electron mobility is ~ 20 cm^2/Vs; hole mobility depends strongly on small temperature fluctuations and electric fields, while remaining usually below 10^{-4} cm^2/Vs. This huge difference in mobility implies that only a fraction of produced pairs recombine, as for oxide thickness smaller than 1 μm all generated electrons leave the oxide in about 10^{-12} s. Holes migrate towards the silicon-silicon oxide interface in a stochastic non-Gaussian process: while most holes require a long time to cover the distance ($\sim$ 1 s for a thickness of $\sim$ 100 nm), a fraction moves significantly faster [80] [81]. Holes slow down and gather in regions where the material shows an increased tendency to bind them. The interface between silicon and its oxide is characterized by strains in the chemical bonds due to the abrupt change in the medium composition. Holes can combine with these fragile bonds producing vacancies, freeing

the oxygen atom from the SiO_2 molecule. The vacancy-rich layer is located at $2 \div 5$ nm from the interface, as in the first few nanometers electrons tunneling from the silicon bulk recombine with holes neutralizing them. At the very interface oxygen is present with density smaller than what is required by a correct stoichiometry, and as a consequence incomplete chemical bonds are present there in a concentration bigger by almost an order of magnitude than what is found at greater depths. Ionizing radiation increases further the number of such dangling bonds with an efficiency strongly related to the quality of the oxidation process.

The major electrical consequences of radiation-induced changes in MOS electronics are shifts in thresholds and in the flat band voltage, affecting simple MOS capacitors as well as the operation of CMOS logic and analog devices.

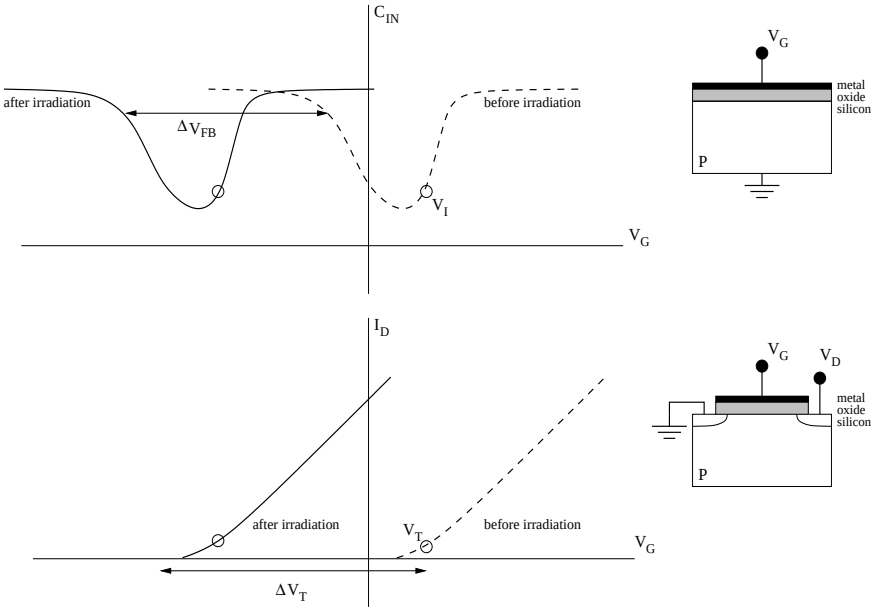

Fig. 5.2 - Radiation-induced changes in n-channel MOS characteristics: shifts in flat-band and threshold voltafe.

The gate capacitance versus gate voltage for a p-substrate, n-channel MOS is shown in Fig. 5.2: the characteristic accumulation-depletion-inversion sequence is clearly seen. The threshold current, determined by measuring the drain current I_D as a function of the gate voltage V_G at a constant V_D, and the characteristic curve for a p-type substrate MOS is shown on the bottom of Fig. 5.3. If we ignore the charge trapped at the Si-SiO_2 and the distorting effects it introduces, then $\Delta V_{FB} \sim \Delta V_T$; this approach is justified as most modern technologies have reduced as much as possible the impact of interface-trapped charge on MOS characteristics(3). For low doses [75]

$$-\Delta V \propto \frac{1}{\epsilon_{ox}} \cdot d_{ox}^2 \cdot D \tag{5.3.1}$$

where ϵ_{ox} is the oxide permittivity, d_{ox} the oxide thickness and D the delivered dose. This

(3) – an exception is heavily radiation-hardened MOS, in which the effects of oxide-trapped charge are so suppressed that interface-trapped charge dominates.

is valid for $d_{ox} > 30$ nm.

For n-substrate, p-channel devices, V_T does not change sign due to the different drain characteristic, but higher and higher gate voltages are required to turn on the device, inverting the channel region, thus possibly disabling the device (see Fig. 5.3).

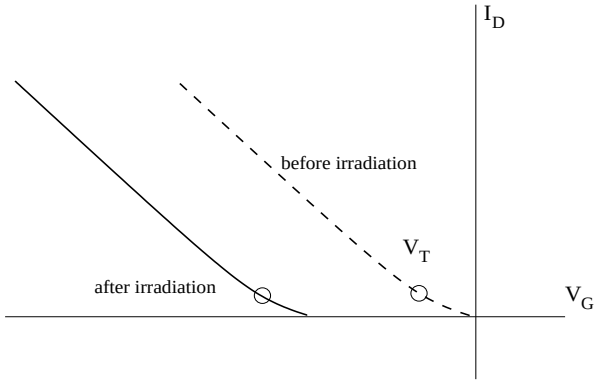

Fig. 5.3 - Radiation-induced changes in p-channel MOS characteristics.

5.4 Single Event Effects

TID effects are due to the cumulative action of a prolonged exposure to an ionizing particle flux, and therefore the damage depends on the total energy released in the electronics active area rather than on the characteristics of the incoming radiation (kind of particles, spectra, etc...). On the contrary, Single-Event Effects (SEE) are related to a single impinging particle depositing an amount of charge, and therefore depend strongly on the physical processes happening while the particle interacts with electronics. Many different failures can arise (upsets, latchups, burn-outs, ...) depending on the characteristics on the irradiated device; some of these will be described in detail in the next sections.

Given their stochastic nature, SEE effects are usually described in terms of a *cross section*, σ_{SEE} so that the number of expected events is

$$N_{SEE} = \sigma_{SEE} \times \Phi \tag{5.4.1}$$

To describe the failure rate in a population of identical components, each of which is independent from the others, the Weibull distribution is used [82], in its integral form and as a function of LET:

$$f(L) = 1 - \exp\left(-\left[\frac{L - L_0}{W}\right]^s\right) \tag{5.4.2}$$

where L_0 is the process threshold and W is the distribution width. The shape parameter s depends on the failure distribution: in most cases experimental data can be fitted with $f(L; s = 1)$.

Then, for the SEE cross section we have

$$\sigma_{SEE}(L) = S_0 \cdot \left[1 - \exp\left(-\frac{L - L_0}{W}\right)\right] \tag{5.4.3}$$

and the reliability of electronic devices for SEE can be described simply in terms of the saturation cross section S_0, of L_0 and of W.

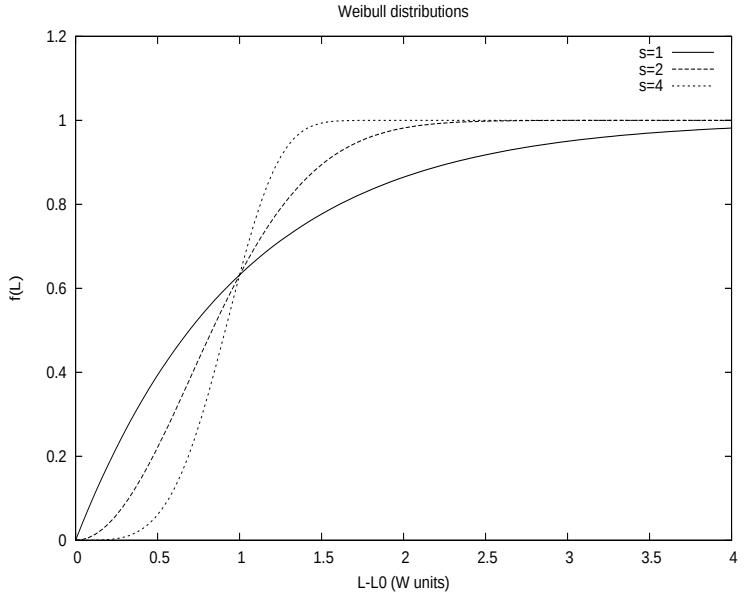

Fig. 5.4 - Weibull distribution functions for various shape parameters.

Every device family is particularly sensitive to some kind of SEE, while practically immune to others: for example Single Event Gate Ruptures (SEGR) and Single Event Burnouts (SEB) are particularly relevant for power MOSFETs, while for conventional CMOS logic the most important SEEs are *upsets* and *latchups*. In the next two sections we will describe these two effects and the design strategies employed to minimize their impact.

5.5 Single Event Upset (SEU)

An energetic particle impacting in the proximity of a bistable element may cause a change of state, called a SEU. In Fig. 5.5 a typical SRAM memory element in CMOS logic is shown: data are accessed through a buffer on each side, a clock-controlled pass-transistor regulates the access to the inner cross-coupled inverters where data are stored. The sensitive junctions in Fig. 5.5 are the four drains in the inner latch: radiation induced charge, collected by the "off" transistor junction, results in a transient current. As this current flows through the hit transistor, the restoring transistor, now "on", provides current in an attempt to balance the particle-induced current. Unfortunately, the restoring transistor has a finite current drive and a finite channel conductivity. Hence, current flow through the restoring transistor causes a voltage drop at its drain. Therefore, this induced *voltage* transient, similar to a "write" pulse, causes the so-called *bit-flip* [83].

SEUs are non-destructive errors, as if a new value is forced on the hit element it is correctly retained; they lead to data corruption or changes in the device configuration.

Several ways exist to harden a circuit against SEU occurrences. A careful choice of the fabrication technology can strongly mitigate the incidence of upsets: reducing the charge collection volumes at the sensitive nodes requires a higher charge deposition to trigger a bit flip. Extra doping layers are extremely useful, as the well-substrate junction provides

a potential barrier that prevents charge deposited outside the layer from diffusing back to a sensitive region [84]. Retrograde wells and buried layers can also be used to create internal electric fields that oppose charge diffusion.

The use of SOI substrates reduces the active volume by fabricating the device in a thin silicon layer electrically insulated from the substrate [85]. In a typical SOI device, source and drain penetrate all the way to the buried insulating layer: the reverse-biased drain junction is limited to the region between the drain and the body of the transistor, thus the SEU sensitive area is reduced.

In 1988 a SEU-hardened CMOS latch design was developed [86], as shown in Fig. 5.6. Transistors P2 and P5 are state-redundant devices that prevent the high side of the latch from discharging low during disturbances. When a write operation begins the state-redundant devices are disabled by the control logic P1,P3,P4 and P6. Consequently the latch does not suffer from excessive delays as may happen when resistors are added in the latch to decouple the inner inverter: in [86] the write response increases from 1 ns to 1.7 ns after hardening. The effective increase in the layout area is small: using the same rule set the latch area increases by $\sim 40\%$.

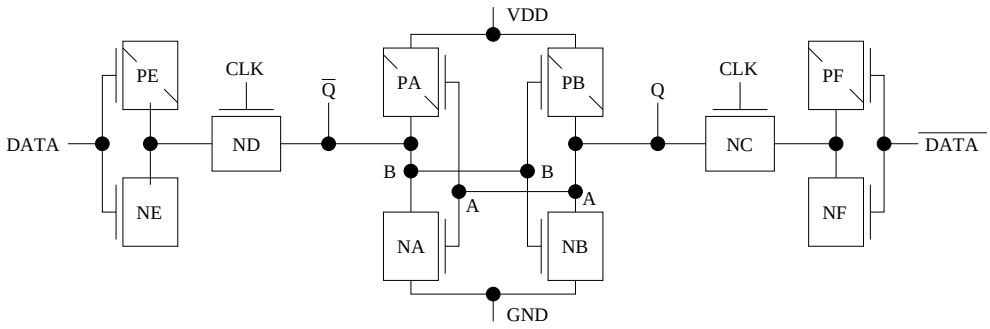

Fig. 5.5 - Unhardened CMOS Data Latch; P's are p-MOS in VDD-biased n-well, N's are n-MOS in grounded p-substrate. Redrawn from [86].

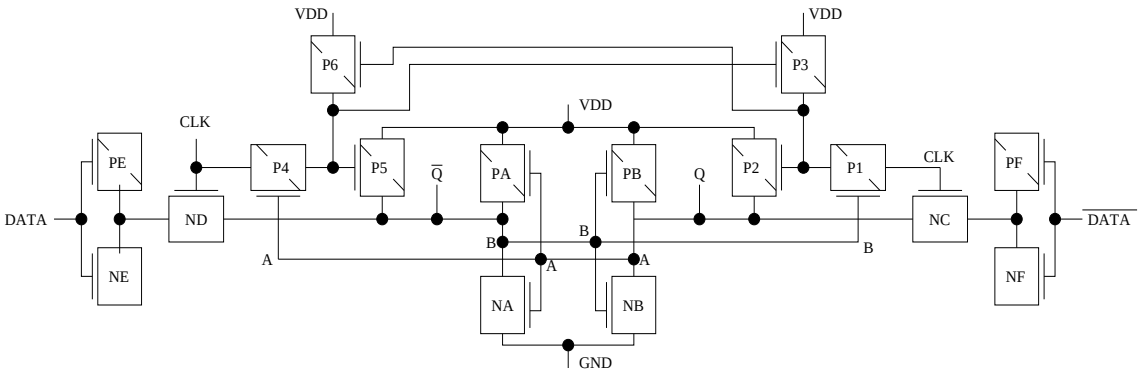

Fig. 5.6 - SEU-hardened CMOS Data Latch; two clock-controlled nodes are added at the sides on the latch core. Redrawn from [86].

Another way to reduce the SEU cross section involves limiting the charge injected by a passing particle. The charge collected by the junction is not given simply by the portion generated within the depletion layer around implants: along the particle track the electric fields are deeply disturbed and a *funnel* forms, channeling charge into the junction from

a considerable depth. The charge-collection volume can be limited by the use of a thin epitaxial layer on top of a heavily doped substrate: the funnel is truncated when it reaches the quasi-metallic bulk and charge is collected only from the epi-layer.

5.6 Single Event Functional Interrupts

When an ion hit triggers an IC into entering a test mode, a reset mode, or any other undesired mode that causes a temporary loss of functionalities, a *Single Event Functional Interrupt* (SEFI) develops [87]. SEFI sensitivity is a function of the device complexity, as more complex microcircuits have several built-in diagnostic or reset modes that remap functions and communication parameters, putting the chip in a mute or idle state.

SEFIs have serious consequences on system operation and often require a full device reset to clear the unwanted condition.

5.7 Single Event Latchup (SEL)

CMOS structures contain parasitic bipolar transistors like those represented in Fig. 5.7; the equivalent circuit is shown on the right. Such a configuration is called Silicon-Controlled Rectifier (SCR). By applying a small voltage between gate and cathode, the lower transistor will be forced on by the resulting base current, which will cause the upper transistor to conduct, which then supplies the lower transistor's base with current so that it no longer needs to be activated by a gate voltage. The necessary gate current to initiate latch-up, of course, will be much lower than the current through the SCR from cathode to anode, so the SCR does achieve a degree of amplification. In the parasitic SCR the gate contact is not present, but charge can be injected in the lower transistor's base by an ionizing particle, thus opening a low-resistance path between V_{DD} and ground. In particular, tests performed with heavy ions, Cf-252 and pulsed laser [88] showed that SEL in CMOS ICs is triggered by charge deposition in the well area of the vertical bipolar transistor: this is typically the transistor with the highest gain and has the largest sensitive area. Ion hitting far from the well contact experience the largest lateral resistance and consequently are the first to turn on the bipolar transistor.

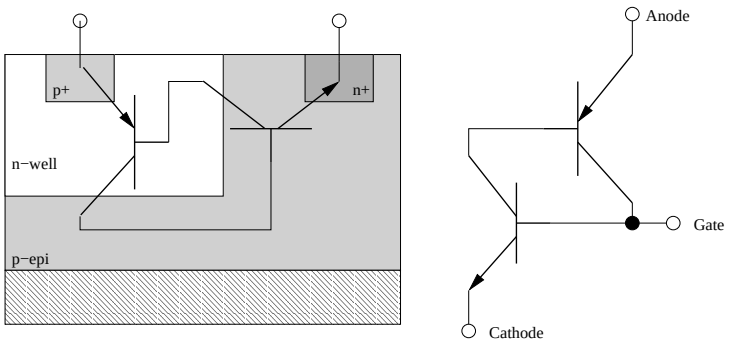

Fig. 5.7 - Parasitic bipolar structure in CMOS technology and SCR latchup model.

After several researchers started analyzing the SEL sensitivity of different devices and more and more experimental data were available, it become evident that there were differences of several orders of magnitude between data on similar devices. For a real understanding of SEL variability one had to wait until the 1990s: while the latchup effect

is the same in like devices, the triggering mechanism by a single heavy ion is significantly different from diffuse radiation induced latchup. In the case of diffuse radiation the entire device substrate is flooded with charge carriers and, as long as the irradiation is uniform, there is no doubt that a dose can be reached that is greater than the SEL threshold. In the case of impinging heavy ions specific locations must be hit, and sufficient energy must be deposited there to trigger the latchup. There may be different sensitive locations and the threshold may differ with the latchup path [89].

A SEL is a serious occurrence is space operation, since it is potentially destructive. Even in the case of a *soft latch*, when the device is not destroyed by the occurrence, it is usually necessary to turn off the supply voltage to shut down the latch.

A common solution to reduce sensitivity to latchups is the use of an epitaxial layer which, as seen in the previous section for SEUs, effectively limits the amount of charge collected by the junctions when an ionizing particle hits the device. The thickness of the epi layer and the device temperature are strongly related to the threshold LET for latchups: in [90] a CMOS SRAM design was tested for latchups with different epi thicknesses and at different temperatures. At 25°C , while for an epi-thickness of 9 μm the threshold LET was found to be above 100 MeV·cm^2/mg, it decreased down to $\sim$ 50 MeV·cm^2/mg for a thickness of 12 μm. On the contrary, below 7 μm no latchup was observed up to 168 MeV·cm^2/mg. It must be noticed that for nominally identical parts built on 9 μm epi, the threshold LET varied in the range $50 \div 90$ MeV·cm^2/mg, while converging down to 40 MeV·cm^2/mg above 75°C.

Once the thickness of the epitaxial layer is fixed, different designs may confer a particularly high resistance to SEL. For HP 0.5 μm CMOS technology, tested in [91], threshold LET increased by $\sim$ 12 MeV·cm^2/mg per 1 μm increase in the well-to-active spacing, going from 63 to 94 MeV·cm^2/mg as the well-to-active spacing increased from 1.5 to 4μm. A further increase is obtained if guard bands are used, so that the SEL threshold LET reached 120 MeV·cm^2/mg.

Latchup sensitivity can be eliminated completely by altogether removing the *pnpn* structures through the use of insulating substrates (SOI). Furthermore, trends for modern technologies show that latchup may not be possible as the supply voltages in deep submicron technologies drop and the minimum holding voltage is $\sim$ 1.0 V [89].

6 Total Dose Validation

In this chapter we describe in more detail the key issues in TID test procedures for devices and parts intended for applications in radiation environments. We then discuss a method of TID dosimetry appropriate for γ ray sources, and the procedures we adopted for γ irradiation are described. The calibration procedure we performed of the ^{60}Co irradiator at the LNL laboratories is reported.

6.1 Total dose radiation hardness assurance

The purpose of TID validation is to ensure that devices and ICs will perform as intended in the environment of interest. The key challenge is to implement this procedure in a cost-effective and timely fashion [92]. Some military environments can expose ICs to dose rates as high as 10^9 rd/s, while natural space environments have dose rates less than 10^3 rd/s. As MOS and bipolar response to radiation often depends strongly on dose rate, particle energy and biasing conditions during irradiation, one is rarely able to test a device in the laboratory under the same environmental conditions the component is required to withstand. Correlation between laboratory tests and behavior in the intended environment is required, hence the need of standardized test procedures. Historically ^{60}Co gamma rays are used [93] [94], even though in some cases ^{137}Cs gamma ray or low energy ($\sim$ 10 keV) X-ray sources are employed.

Dose rate, originally allowed in the range 2–2500 rd/s, has been limited to the 50–300 rd/s range to ensure greater uniformity from manufacturer to manufacturer to test results, even though it is recognized this can be as much as four orders of magnitude higher than the operational rates for space-operated systems. As an option [93], if the maximum dose rate is < 50 rd/s for the intended application, the parties involved in the test can agree to perform the test at any dose rate greater than the maximum dose rate of the intended application.

Accelerated aging of damage at $(100 \pm 5)^\circ$C for 168 ± 12 hours is required if the ionizing dose in the intended application is greater than 5 krd, whenever circuits are known to contain MOS elements and the dose rate during test is not the same as that of the intended application [94].

The selection of the sample conditions under irradiation is often the most important aspect of TID characterization. Typically, TID effects are worse at higher supply voltages: the device therefore should be biased at the largest specified voltage, if more values are applicable. Static bias conditions generally produce the greater degradation under irradiation; however, some technologies have shown worst responses when actively clocked. Usually such differences are not sufficient to justify the additional complexity of a system to load test vectors to ensure data are being transmitted through the significant parts of the IC by an active clock.

The sample size, for each unique set of test conditions, must be selected: "*For example, if the parts are to be used in a system, the population should be representative of the parts that will be used for flight hardware, that is, single wafer, single process lot...*" [93].

When ^{60}Co is used as a source of γ rays for TID characterization, devices under irradi-

ation must be enclosed in a Pb-Al container to minimize dose enhancement effects caused by the low-energy photons scattered by the irradiation chamber and within the Co core itself. A minimum of 1.5 mm Pb, surrounding at least 0.7 mm Al, is required. Of course, if it can be demonstrated that low energy scattered radiation is so small that it will not cause dosimetry errors, the shield can be omitted. Influence of such dose enhancement has often been measured; moreover when no shielding was used deviation from the inverse square law was reported when moving dosimeters away from the source to achieve a greater dose uniformity [95], [96].

6.2 Chemical dosimetry

Chemical dosimetry of ionizing radiation encompasses all dosimetric methods based on the determination of (different) chemical changes taking place in certain systems undergoing irradiation. A number of methods have evolved, either providing a direct measurement of energy absorption, or requiring calibration with known doses. An important factor is the dependence of such chemical changes by the ionization density as well as by the total number of ions produced. The target field of application must also be considered, as the high doses and intensities are common in solid-state applications.

Any dosimetric system must meet certain specific requirements. In particular, the *chemical transformation yield* (*G-value*), defined as the number of molecules that reacted per 100 eV of absorbed energy, must be sufficiently high and, within the foreseen range of experimental conditions, independent of: radiation type, energy, dose rate, concentration of reagents, temperature and any parameter that may vary during the irradiation.

In addition, the dosimetric system should be stable before and after irradiation, the determination of the G-value should be rapid and simple and the preparation of the system must be feasible using reagents of available degrees of purity.

A dosimetric system satisfying all the requirements above is called *ideal*, and as such, nonexistent(1). One must choose the dosimetric system that best suites his needs, taking into account the setup in use and the experimental conditions during the irradiation phase.

6.3 Dose determination

The dose absorbed by a dosimetric system is calculated from the extent of the chemical transformation that took place in the sample, knowing the G-value of the chemical transformation. Therefore, the delivered dose can be written as

$$D = \frac{N_A \cdot c}{G \cdot \rho \cdot 10} \text{ eV/g} \tag{6.3.1}$$

or

$$D = \frac{9.64 \cdot 10^8 \cdot c}{G \cdot \rho} \text{ rd} \tag{6.3.2}$$

where N_A is Avogadro's number, c is the molar concentration of the product, G, as usual, is the reaction yield and ρ is the density of the system in g/cm^3.

(1) – as yet!

In most cases, the dosimetric medium and the system under study are composed of different materials, and therefore they have different absorption parameters for γ radiation. Given a slab of absorbing material of thickness t and density ρ, the ratio between the energy exiting the slab and the initial energy is given by

$$E/E_0 = \exp\left(-\left(\mu_e/\rho\right)x\right) \tag{6.3.3}$$

where x is the *mass thickness*, $x = \rho \cdot t$, while (μ_e/ρ) is called the *mass energy-absorption coefficient*. The latter is defined by the equation:

$$(\mu_e/\rho) = (1-g)\frac{\text{KERMA}}{\Phi} \tag{6.3.4}$$

where KERMA[(2)] is the sum of the kinetic energies of all those primary charged particles released by uncharged particles (photons in our case) per unit mass, Φ is the particle fluence and g represents the average fraction of the kinetic energy of secondary charged particles (produced in all the types of interactions) that is subsequently lost in radiative (photon-emitting) energy-loss processes as the particles slow to rest in the medium. The evaluation of g can be performed by integrating the cross section for the radiative process of interest over the differential track-length distribution established by the particles in the course of slowing down.

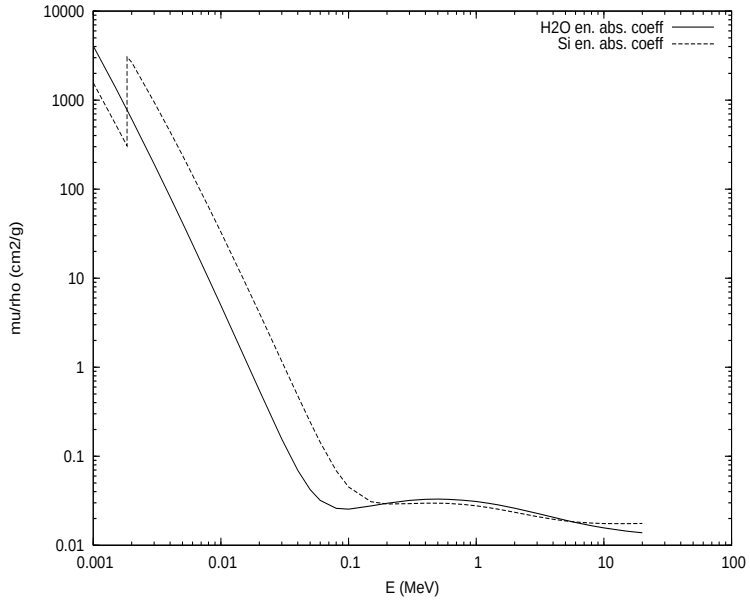

Fig. 6.1 - Mass energy-absorption coefficient in silicon and water, from [97].

From Eq. 6.3.3 it follows that the dose absorbed by the system under study may be obtained by the dose absorbed by the dosimeter using the formula:

$$D_{\text{syst}} = \frac{(\mu_e/\rho)_{\text{syst}}}{(\mu_e/\rho)_{\text{dos}}} D_{\text{dos}} \tag{6.3.5}$$

(2) – KERMA: Kinetic Energy Released in Matter.

Mass energy-absorption coefficients depend on the radiation kind and energy, and up-to-date values can be found for different materials in the NIST database [97]. In the case of compounds the mass energy-absorption coefficient can be computed from those of the constituent elements as:

$$(\mu_e/\rho) = p_1 \cdot (\mu_e/\rho)_1 + p_2 \cdot (\mu_e/\rho)_2 + \dots \tag{6.3.6}$$

where the p_i are the weight fractions of the constituent elements.

6.4 Dose rate determination

For gamma ray dosimetry we chose to employ the *ferrous sulfate system*, also known as Fricke dosimeter [98], as it best conforms to the specifications above, while remaining easy to prepare and to characterize after irradiation. Information on the preparation of the dosimetric samples are given in App. 2. The determination of the ferric iron concentration produced by ionizing radiaiton in the irradiated system is based on the spectrophotometric determination of the optical density of the solution at $\lambda = 304$–305 μm. The molar extinction coefficient ϵ of Fe^{3+} in 0.4 M H_2SO_4 is 2130 ± 36 $mol^{-1}cm^{-1}$ at 20° C; it's temperature dependent, increasing by 0.7% per degree centigrade.

If I_0 is the intensity of light striking the test tube and I is the intensity coming out on the other side, we can define the optical density Θ as

$$\Theta = \ln (I_0/I) \tag{6.4.1}$$

It is particularly convenient for our purposes to express the optical density in terms of the concentration of attenuating centers in the solution as

$$\Theta = \epsilon \cdot c \cdot l \tag{6.4.2}$$

where ϵ is the molar extinction coefficient (in $mol^{-1}cm^{-1}$), c is the attenuator concentration in the solution (in mol) and l the path length (in cm).

Dose can be readily calculated (at 20° C) using Eq. 6.3.2:

$$D = \frac{2.83 \cdot 10^4 (\Theta - \Theta_0)}{l} \text{ rd} \tag{6.4.3}$$

where Θ_0 and Θ are the optical densities before and after irradiation respectively and l is the thickness of the absorbing cell; we have considered the density of the ferrous iron dosimeter to be 1.025 g/cm^3 and its yield $G = 15.5$ ions/100 eV (see App. 2). The dose rate can therefore be computed as

$$R = \frac{2.83 \cdot 10^4 (\Theta - \Theta_0)}{lt} \text{ rd/sec} \tag{6.4.4}$$

6.5 LNL ^{60}Co source calibration

The CNR-ISOF gamma source at the INFN Laboratories of Legnaro consists of a ^{60}Co source contained by a thick Pb cylinder. Once the radioactive core is exposed it radiates almost isotropically(3). This facility provides the users with a wide range of dose rates (approximately 0.5–100 rd/s, or 1.2–250 krd/hr), easily chosen by placing the device under test (DUT) at a specific distance from the radiating core. ^{60}Co decays follow the scheme shown in Fig. 6.2: this isotope has a lifetime of 5.28 years and β-decays into excited states of the stable nucleus ^{60}Ni. With almost 99.9% efficiency the 2.51 MeV 4th excited state is formed; in this case the nucleus emits two photons (1.17 MeV and 1.33 MeV) before reaching the ground state.

Given the dependence of dose rate with solid angle, a major concern is the dose uniformity on the DUT surface. While this is not a problem in conventional irradiation chambers, known as *gamma cells*, where the dose rate is homogeneous inside the chamber, in the case of 4π sources, such as the Legnaro one, the solid angle dependence of the gamma flux forces the users to a careful planning of the irradiation setup.

A simple trigonometry calculation shows that, in the case of a circular target of radius r placed facing the source at a distance d, the flux at its outer edge is $1 - r^2/d^2$ respect to what is measured at its center. This places a strong constraint one the dose rates achievable with larger samples when a good uniformity is required.

In the June 2003 we characterized the CNR-ISOF ^{60}Co source, measuring both the absolute dose rate and its uniformity at a distance of 30 cm from the source. The experimental setup is shown in Fig. 6.3. We prepared three test tubes containing the Fricke dosimetric solution described in App. 2. A Pb-Al shield was prepared, enclosing an aluminum box (walls are 2.5 mm thick) with a 2 mm thick Pb sheet, to measure dose enhancement due to low-energy scattered photons.

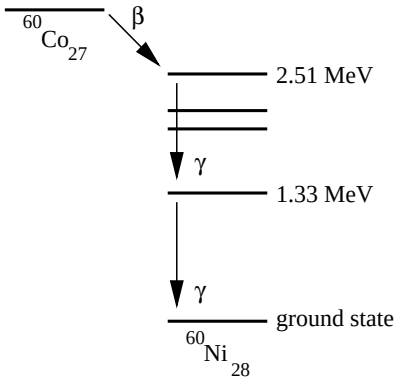

Fig. 6.2 - Decay scheme of 60Co; illustrated decay path happens 99.9% of the times.

A first tube was kept level with the source, near the surface of the table, and placed at 30 cm from the ^{60}Co core, to act as a reference sample. The results obtained with this dosimeter were compared with older data from earlier calibrations and found to be equivalent within experimental errors (the natural decay of the source intensity was obviously kept into consideration).

(3) – with a minor correction due to its cylindrical shape

A second test tube was placed at the same distance from the source and its center was raised 15 cm from the table, to monitor the uniformity in the transverse plane.

The third dosimeter was placed within the Pb-Al shield to measure the dose rate once the low energy component was suppressed. The dose rate obtained with this tube was then used for planning the irradiation of electronics samples.

The dosimetric liquid was then poured into identical glass containers 1 cm thick, previously washed and rinsed with the unused dosimetric solution. In table 4.1 the results of our measurements are shown. Inspecting the results for the 1 hour irradiated samples, we can immediately observe that uniformity in the vertical plane is better than 5% over 15 cm. Furthermore, the presence of the Pb-Al shield causes a ∼15% decrease in the dose rate. A MC simulation of the gamma energy after this shield is shown in Fig. 6.4: about 85% of the incoming photons are still contained in the two peaks at the initial energies. The remaining photons are distributed more or less evenly at smaller energies.

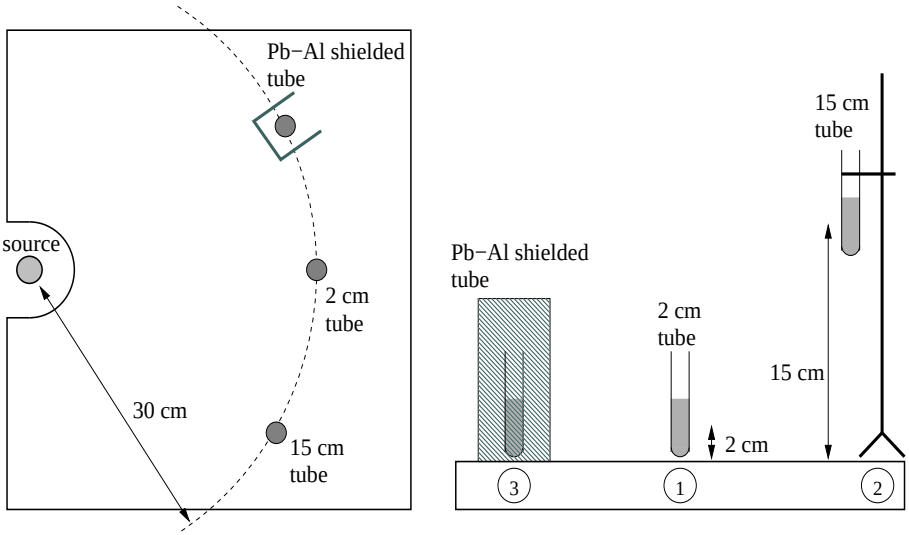

Fig. 6.3 - Schematic representation of our setup during ^{60}Co calibration.

	Tube 1	**Tube 2**	**Tube 3**
Irr. time (min)	dose ($\Theta - \Theta_0$)	dose ($\Theta - \Theta_0$)	dose ($\Theta - \Theta_0$)
30	6509 rd (0.230)	—	—
60	12537 rd (0.443)	12028 rd (0.425)	10702 rd (0.381)
90	18876 rd (0.677)	—	16697 rd (0.590)

Tab. 6.1 - Optical attenuation and corresponding doses (in rd) as measured for the three dosimetric solutions; see Fig. 6.3.

Dose rates for water, *without shielding* and at 30 cm from the source can be calculated from the values in the first column, obtaining

$$R(\mathrm{H_2O}, 13\ \text{Jun 2003},\ 30\ \text{cm, w/o shield}) = 3.50\ \text{rd/s} \tag{6.5.1}$$

Using the average shield-induced attenuation obtained from the third column in Tab. 6.1 (~ 0.87) we have the dose rate behind the Pb-Al shield

$$R(\mathrm{H_2O}, 13\ \mathrm{Jun}\ 2003,\ 30\ \mathrm{cm},\ \mathrm{w/}\ \mathrm{shield}) = 3.06\ \mathrm{rd/s} \tag{6.5.2}$$

The attenuation of ~ 1 MeV photons given by the lead plate can be calculated with Eq. 6.3.3, obtaining ~ 0.87. Within the shielded box we observe a dose rate smaller by exactly the same amount with respect to the non-shielded dosimeter: this indicates that the low-energy contribution is negligible. This implies that the use of a 4π irradiator without a heavily shielded small irradiation chamber enclosing the devices under test and the source core(s) makes the Pb-Al shield superfluous. Nonetheless, as the shield box was already built, we used it in all our irradiations. As a reference, a Monte Carlo simulation of the effect of the Pb-Al box on the ^{60}Co γ spectrum is shown in Fig. 6.4.

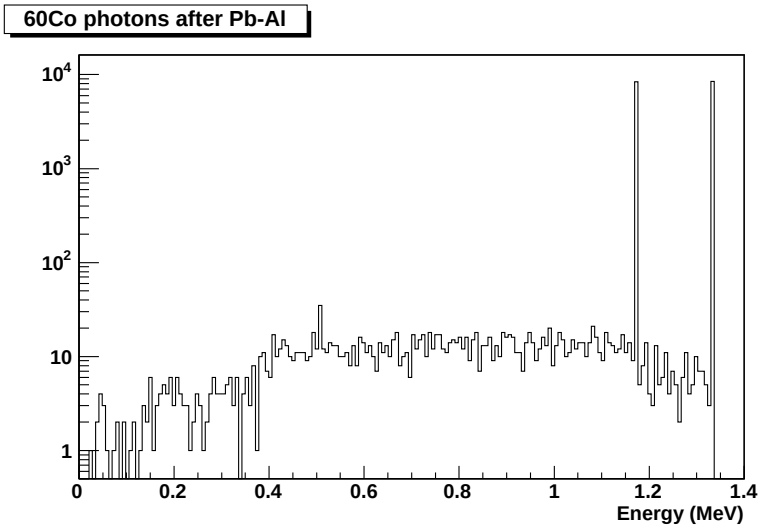

Fig. 6.4 - Spectrum of gamma rays after 2 mm Pb and 2.5 mm Al; MC simulation for 20,000 impinging photons, half 1.17 MeV, half 1.33 MeV.

The dose rates reported above refers to a water dosimeter; to calculate the dose rate in silicon we use Eq. 6.3.5, where the mass energy-absorption coefficient ratio is calculated at an average energy of 1.25 MeV (from [97]):

$$D_{\mathrm{Si}} = \frac{(\mu_e/\rho)_{\mathrm{Si}}}{(\mu_e/\rho)_{\mathrm{H_2O}}} \cdot D_{\mathrm{H_2O}} = \frac{2.652 \times 10^{-2}}{2.965 \times 10^{-2}} \cdot D_{\mathrm{H_2O}} = 0.894 \cdot D_{\mathrm{H_2O}} \tag{6.5.3}$$

Finally, we can calculate the dose rates for silicon, with and without the Pb-Al shield, obtaining

$$R(\mathrm{Si}, 13\ \mathrm{Jun}\ 2003,\ 30\ \mathrm{cm},\ \mathrm{w/o}\ \mathrm{shield}) = 3.13\ \mathrm{rd/s} \tag{6.5.4}$$

and

$$R(\mathrm{Si}, 13\ \mathrm{Jun}\ 2003,\ 30\ \mathrm{cm},\ \mathrm{w/}\ \mathrm{shield}) = 2.74\ \mathrm{rd/s} \tag{6.5.5}$$

corresponding to 11.3 krd/hr and 9.86 krd/hr respectively. This indicates that one hour is required to reach 10 krd. The required time increases by $\sim 1\%$ every month due to the natural decay of the active isotope in the source.

We calculated above the dose rates in silicon; for silicon oxide the difference is slightly less than 0.4%. All calculations assume a distance from the source of 30 cm; to increase uniformity and/or lower the dose rate the devices can be placed farther away at a distance d; in this case the dose rate will be

$$R(d) = R(30\text{ cm}) * \left(\frac{30\text{ cm}}{d}\right)^2 \tag{6.5.6}$$

7 Radiation tests

In this chapter the test procedures developed to monitor the behavior of TKR ASICs under irradiation, and to measure their performances after irradiation, are detailed. TID and SEE experimental results are presented; the entire process of assessing radiation hardness assurance for the TKR ASICs was published in [99].

In the final part of this chapter test results obtained in the INFN laboratories in Padova on DAQ ASICs and commercial components parts are shown.

7.1 RHA assurance procedures

Following standard *radiation hardness assurance* (RHA) procedures, each time a flight lot is produced, a few sample ASICs are selected for radiation testing. Test plans require us to test 2 ASICs for SEE and 7 ASICs for TID: the samples must be irradiated and test result must conform to specified standards.

Strictly speaking, this part of the radiation validation effort constitues nothing more than a *screen-test procedure*. Of course, before the RHA plan reaches this point the parties involved must have gained a detailed knowledge of the susceptibility of the different DUTs to radiation damage, so that the functionalities needing to be monitored and the boundaries defining the "expected behavior" can be assessed.

The most interesting results detailed in this chapter come mainly from this first "investigation phase", performed in late 2002 and 2003. The subsequent screening procedure is now being completed with the test of the final flight lots of TKR and DAQ ASICs.

7.2 The VME DAQ system

In this chapter the details of the tests performed on TKR ASICs are given. Tests of the Multi-Chip Modules were carried out using the Test Data Acquisition system developed at SLAC: a description of the hardware configuration is given here, while the next sections describe the software we developed.

The central part of the DAQ is a VME COM board. It is a FPGA-driven, 16-bit *pattern generator* and *logic analyzer* used to generate the desired control and data signals and to capture the response of the system under test. The VME interface is managed by the XILINX VME core. An internal generator provides a 40 MHz data clock, or an external clock can be provided; the clock frequency on the data lines is half the one provided to the logic core. All 16 outputs are LVDS lines.

register	storage in 32 bit words	VME address
CONTROL	1	BaseAddr+0x0
STATUS	1	BaseAddr+0x4
PLAY FIFO	32k	BaseAddr+0x8
RECORD FIFO	32k	BaseAddr+0xC

Tab. 7.1 - Registers implemented in the COM, their storage capabilities and their position in the VME memory space.

Two 32k FIFOs are implemented, labeled *PLAY* and *READ*; in the former patterns are stored before they are send to the DUT, while the latter receives the output. Two register, labeled *CONTROL* and *STATUS* manage the board operations; as an example, the contents of the CONTROL register are shown in Tab. 7.2.

Two 16×2 in-line connectors are placed on the COM front panel: the 16 LSB of bytes in each FIFOs are sent to or received from the corresponding LVDS line in the IN or OUT connector. Signals transit through a LVDS repeater board (IF, *interface board*), where signals are regenerated by a LVDS-CMOS-LVDS conversion. Two ribbons of Teflon-coated wires departs from the IF board and reach the two GTRC ASICs in the MCM. A summary of the interconnections from the cables and the ASICs on the MCM is shown of Fig. 3.12.

A schematic of the DAQ system is shown on Fig. 7.1.

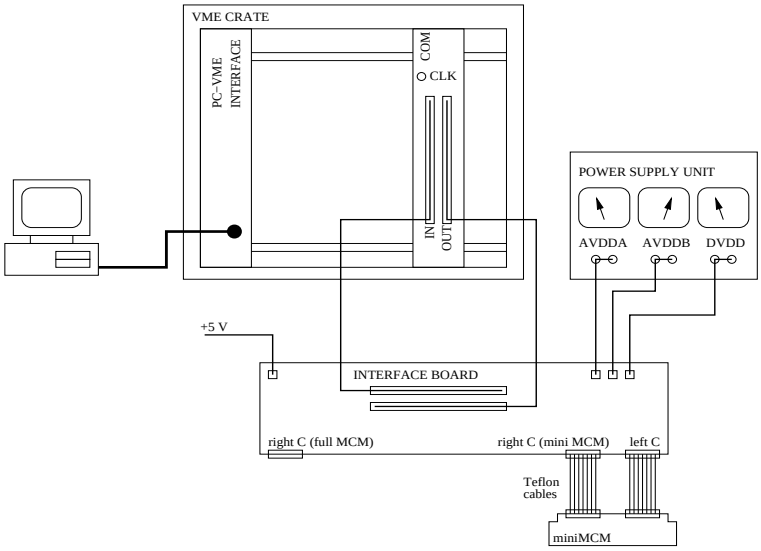

Fig. 7.1 - Schematic of the TKR DAQ in Padova.

7.3 The SCIPP software environment

For tests performed at the Santa Cruz Institute for Particle Physics a graphical environment was developed, with a Python-wrapped C library, managing the VME COM board through a National Instrument interface board, and an upper-level Python API to manage ASIC operations. Scripts, written in Python using the predefined top-level functions, are executed by the main application and results are displayed on the output window.

7.4 The SIRAD test programs

Being specifically crafted to be used in routine tests performed in laboratory, the SCIPP software was not found to be perfectly suitable for irradiation tests, mostly due to complications involved in adding extensions providing a careful timing, often necessary to check simultaneously data readout from the ASIC registers, the power supplies, etc. Moreover, a certain speed in data handling is required when dealing with high ion fluxes and therefore high SEE rates. Rather than trying to modify the existing code we decided to develop a new test suite, specifically thought for irradiation tests, as a standalone application. The

low level VME interface is the same used by SCIPP, without the Python wrapper and slightly modified to use a SBS-617 VME interface we already possessed in Padova.

We chose to develop an intermediate level library, implementing all useful GTRC and GTFE commands ([48],[52]). A *data stream* object is created, as an array of *frames*; each frame stores the status of the 16 output lines (`1` or `0`). Once the data stream is complete it can be written in the PLAY FIFO. When the `play()` command is issued the frames are sent to the output lines in sequence, timed by the COM clock. As the internal COM clock runs at 40 MHz it means that on any line a 20 MHz clock can be generated by storing in the corresponding position in the data frames an alternating sequence of `1`s and `0`s.

CONTROL register	
bits	function
0-5	chan 0 delay
6-11	readback delay
12	reset PLAY data, conf
13	reset PLAY data
14	reset RECORD data, conf
15	reset RECORD data
16-23	delay in writing to RECORD
24-28	unused
29	auto clock on chan 0
30	acquisition trigger enable
31	start acquisition

Tab. 7.2 - CONTROL register contents.

While the PLAY FIFO is clocked, the RECORD FIFO stores the status of the COM input lines. The intermediate level library contains functions to load the RECORD FIFO contents into a new data stream. The stream can then be analyzed to extract the ASIC response: commands, data fields, trigger requests, tokens, etc.

Test are realized as a top level library implementing all tests described in [100], [101]. The final test program is an application that interfaces with the user, handles his requests and the output, plus other external tools.

7.5 The SEE-safe power supply box

Irradiation tests expose the DUT to the risk of destructive phenomena. In particular we are requested to test for SEL, and any such occurrence could easily lead to a dead ASIC. Commercial power supplies have the possibility to set a current limit, but the response times in case of fast transients was not believed to be appropriate. Moreover, limiting the current to a nominal value given by the power consumption of a single ASIC times the number of ASICs on a MCM does not ensure that, in the case of a SEL, a single chip could not draw the entire current amount through the SEL conductive path and thus be destroyed. It becomes necessary to completely cut the power, a function that in many commercial power supplies is not available and that becomes too slow if implemented via software remote operation.

In some cases a simple current-limiting stage is employed, like the one shown in Fig. 7.2. The resistor limits the amount of current the DUT can sink, while the capacitor provides

the initial charge required to sustain the activation of the latchup until the sense circuit recognizes the SEL. Such a filter can generally be tuned to fit the user's needs, yet it does not always allow for a fast and precise monitoring of the SEL occurrence and duration. Therefore, we decided to develop a custom SEL-safe power supply box (PSB), tailored to provide the currents required by the MCMs.

The PSB is composed by two circuit boards. The top board hosts the analog part of the unit. The required AVDDA, AVDDB, DVDD voltages (see Sect.3.9) are generated with voltage regulators; trimmers can be used to fine-tune the voltage levels so that the required values are met *at the MCM level*.

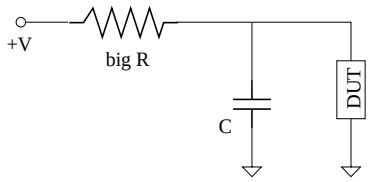

Fig. 7.2 - A schematic of a simple but effective limiting circuit for current transients.

Each power line contains a small ($< 5\ \Omega$) resistor; the voltage drop across this resistor enters a two stage amplifier and the output is compared with an adjustable threshold voltage. If the voltage drop increases over the threshold the power (*on all power lines*) is cut in less than 1 μs. The power is then restored with a slow ramp (requiring at least 5 s) to allow for a prompt power-down if the power dissipation is still above threshold. A LED close to the each power outlet give the output status, turning off if the corresponding power line caused the power-down and turning on when the power is back to normal.

Using the same logic, a second board in the PSB generates a byte where the 3 LSB encode the status of the corresponding power outlet. A PC serial interface was implemented so that it is possible to inquire the output status and thus identify SEL and wait for the power to reset. The board requires the query from the PC to generate the status word, so the status must be periodically checked to spot power interruptions.

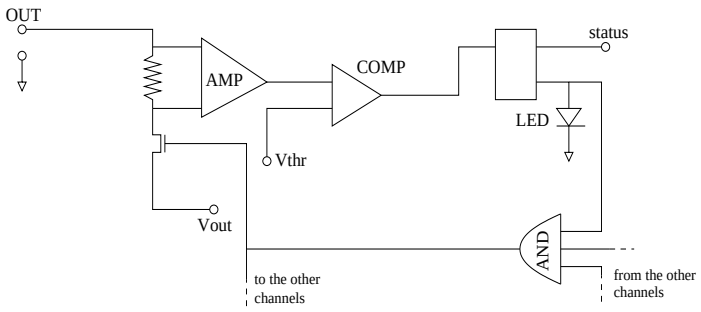

Fig. 7.3 - Schematic drawing of a power outlet in the PSB; the status bit going to the serial interface is shown on top.

7.6 SEE tests

The procedures followed in SEE tests with heavy ion irradiation are simple. Only digital operations are required for measuring SEU cross sections, while monitoring the PSB let us spot latchups.

In order to measure SEU cross sections it is necessary to load in all sensitive registers a recognizable pattern, or more than one as we are interested in both `1→0` and `0→1` transitions. Rather than using simple all-zero and all-one patterns we decided to use complementary picket-fence patterns (i.e. `1010` and `0101`); while making the data analysis slightly more complicated, this allows one to clearly identify problems in data communications.

The amount of time between the read and write operations corresponds to the time during which SEUs are recorded. While being written and read-out the registers are not SEU-hardened: this means that the SEU cross sections increase in this period by a factor 4[(1)]. The writing operation requires a time interval of the order of a hundred clock cycles, corresponding to 5 ms. We usually wait about ten seconds between the write and read instructions: this means a factor 2000 in difference, more than enough to consider the deviation in the cross section estimates negligible. Moreover, in the amount of time during which registers are anomalously sensitive to upsets a maximum of 10 ions could hit the DUT, even with the highest ion fluences available. The chance of one of them hitting a sensitive part of the ASIC is so low that we can easily ignore these intervals and consider the cross sections we report to be accurate. Similar considerations apply to the non-hardened shadow registers, where data are stored while being serialized.

For recording SELs we took advantage of the fact that, once the power is cut, it takes from 5 to 10 seconds for the status to revert to nominal, assuming the latchup was neutralized by the reset cycle. So, checking for SELs every second is an adequate procedure.

7.7 SEE irradiation procedures

The list of the most common ion beams at SIRAD and the relative LET and range in Si is reported in Tab A3.1 for the Tandem accelerator running at 14 MV: ^{197}Au has the highest available LET (see App. A3).

We have already seen in Sect. 4.6 that the maximum LET the GLAST orbit permits is around 100 MeV×cm^2/mg; saturation is in any case expected sooner from previous experiments on test structures. We have seen in Chap. 5 that 5 MeV×cm^2/mg is considered the lower limit of the "interesting range" for SEE studies.

The larger the number of ions hit the DUT the better the cross section estimates are, but we must limit the TID delivered to the ASIC by them. A good compromise is to deliver a total of 10 krd summing all four ion irradiations, as this is the value the chips must prove to withstand.

Given the above constraints, we select a set of four ions more or less evenly spaced in LET from the list: Si, Ni, Br and Ag. Au could be added to this list if SEE cross sections do not saturate before Ag. To verify the saturation trend before switching to a simplified schedule removing Au, we decided to execute a heavy ion run delivering a total of 30 krd; the chips did survive and the results are shown in Tab. 7.4.

The beam size is approximately 2 × 2 cm^2; as the GTFEs in particular are placed very close to each other this means we would irradiate more than one chip at a time. While this is not a problem for SEUs[(2)], it becomes a big unknown when calculating

(1) – in Sect. 7.11 we will see how we could measure this value.

(2) – besides the undesirable waste of half the chips present on a MCM.

SEL rates. We therefore used a shield made from an Al plate 2 mm thick. The shield let us expose odd (even) GTFEs while protecting even (odd) ASICs. A similar shield was manufactured, with holes in correspondence with the GTRCs, when they required irradiation. All SIRAD ions are stopped by the shields we use: 2 mm Al are enough to stop protons with an energy of 20 MeV or less [102].

7.8 The SEE tests suite

Using the software libraries described above a SEE test program was written. Immediately after the basic initialization, it forks into two parallel processes.

- The first process continuously writes data into the DUT registers, waits a preset amount of time and reads them back, then stores the raw data into a log file. It checks for differences between the input and output patterns in real time to give the user a quick summary of what is going on (number of recorded upsets, other errors, etc.). If during the waiting phase the SEL flag is raised, the current acquisition is discarded and the process starts a new write-wait-read cycle once the SEL ends.
- The second process periodically asks the PSB for the power status. If the power is off it raises a flag that stops the companion process. In this case it continues the monitoring until the power is back to normal and then lowers the flag and let the operations resume.

On Fig. 7.4 an example screenshot is shown. "Good" SEUs (bottom left) are defined here as events in which less than 10 bits flipped, to distinguish communication errors or complete functionality interruptions. This parameter is meant only as a hint of the DUT behavior for the operator: SEU analysis is performed later on logged data. The parameter window (bottom right) shows the configuration entered from the command line when the program was launched: the selected DUT, the employed pattern, the GTRC the commands are sent to, the number of steps and the time between each write and read commands, verbosity of data output and status of the serial connection to the PSB.

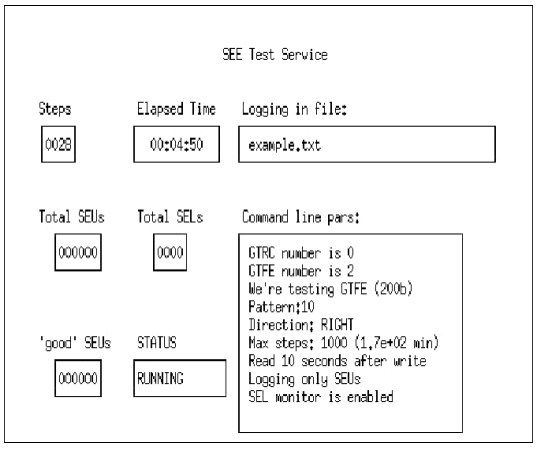

Fig. 7.4 - Example screenshot of the SEE test suite, running with a standard parameter choice.

7.9 Example data from SEE runs and analysis

As an example we include here fragments from several log files from an actual SEE run with heavy ions; data are shown in Fig. 7.5–7.7.

```
Thu Jun  5 21:59:02 2003
<t=571>GTFE TRG: 1 seu(s) detected!!
>>10101010101010101010101010101010101010101010101010101010101010
<<10101010101010101010101010101010111010101010101010101010101010

Thu Jun  5 21:59:02 2003
<t=571>GTFE DAC: 1 seu(s) detected!!
>>00000000000000000000000000000000000000000000000010101010101010
<<00000000000000000000000000000000000000000000000010101010101000

Thu Jun  5 21:59:12 2003
<t=581>GTFE CAL: 1 seu(s) detected!!
>>10101010101010101010101010101010101010101010101010101010101010
<<10101010101010101010101010101010101010101010001010101010101010

Thu Jun  5 21:59:53 2003
<t=622>GTFE MUTE: 1 seu(s) detected!!
>>00000000000000000000000000000000000000000000000000000000000001
<<00000000000000000000000000000000000000000000000000000000000000

Thu Jun  5 21:59:53 2003
<t=622>GTFE CAL: 1 seu(s) detected!!
>>10101010101010101010101010101010101010101010101010101010101010
<<11101010101010101010101010101010101010101010101010101010101010

Thu Jun  5 21:59:53 2003
<t=622>GTFE DAC: 7 seu(s) detected!!
>>00000000000000000000000000000000000000000000000010101010101010
<<00000000000000000000000000000000000000000000000000000000000000
```

Fig. 7.5 - Sample SEU data taken during a GTFE irradiation with Ag.

```
Fri Jun  6 04:55:20 2003
<t=70>GTRC CONF: 30 seu(s) detected!!
>>00000000000000000000000000001111100000110101010101010101010101
<<53054928163880062520491516251950175013568623684915162200491512878

Fri Jun  6 04:55:20 2003
Error reading pattern from GTRC sync... retry
```

Fig. 7.6 - Sample SEFI data taken during a GTRC irradiation with Si at SIRAD.

For each read-back with errors[3] local time and seconds elapsed since the test began are logged. The register being accessed is specified, and the total number of mismatched bits is calculated. The written pattern (indicated by a ">>" sign) and the read one ("<<") are written one on top of each other, allowing for further analysis.

```
Fri Jun  6 02:18:16 2003
<t=71>GTFE MUTE: 1 seu(s) detected!!
>>00000000000000000000000000000000000000000000000000000000000001
<<00000000000000000000000000000000000000000000000000000000000000

Fri Jun  6 02:18:16 2003
<t=71>GTFE CHN: 32 seu(s) detected!!
>>10101010101010101010101010101010101010101010101010101010101010
<<00000000000000000000000000000000000000000000000000000000000000

Fri Jun  6 02:18:16 2003
<t=71>GTFE CAL: 32 seu(s) detected!!
>>10101010101010101010101010101010101010101010101010101010101010
<<00000000000000000000000000000000000000000000000000000000000000

Fri Jun  6 02:18:16 2003
<t=71>GTFE TRG: 32 seu(s) detected!!
>>10101010101010101010101010101010101010101010101010101010101010
<<00000000000000000000000000000000000000000000000000000000000000

Fri Jun  6 02:18:16 2003
<t=71>GTFE DAC: 7 seu(s) detected!!
>>00000000000000000000000000000000000000000000000010101010101010
<<00000000000000000000000000000000000000000000000000000000000000
```

Fig. 7.7 - Sample SEFI data taken during a GTFE irradiation with Ni as SIRAD.

In Fig. 7.5 some characteristic features are present. The first events are "standard" events: a bit in the output stream has flipped. The last event is clearly different: the data field is completely blank: this usually indicates a communication error, or a failure in functionalities. The distinction is rather delicate and deserves a detailed explanation.

[3] – assuming verbose logging was not selected, else all read data are saved.

In the case a GTRC is under test, when a failure happens the output stream from the MCM contains only garbage or it is missing altogether. In these cases the data extraction routine fails and a series of random digits appear in the logged output frame, as the storage array was not initialized properly (see Fig. 7.6). On the contrary, when a GTFE is being tested, even a complete functional failure produces only empty streams, as the communication with the GTRC is carried on flawlessly, the only difference being that no data are received from the GTFE.

We have defined the following terminology, to unify the description of TKR ASICs single-event effects:

- a *Single Event Functional Interrupt* (SEFI) is observed when the output stream from the GTRC is completely garbled, OR when all read operations tried on an ASIC keep failing until a full reset is issued;
- a *Communication Error* (CME) is observed when a data frame from the DUT is blank, but other reading operation performs correctly in the same time window between two reset cycles, OR when five or more nearby bits flip together, the probability of this last occurrence because of one or more SEUs being negligible.

The fourth event in Fig. 7.5 involves the GTFE MUTE (aka MODE) register. Being only two bit long it is impossible to discriminate between communication errors and real upsets; for this reason data are included in log files for completeness, but are not further analyzed.

The correct behavior of the PSB was checked before all irradiations: by shorting the outlets with a small resistor we verified that the DAQ program reported a SEL.

7.10 Measurement of SEE cross sections

In this section the results of the TKR SEE characterization are reported. SEU cross sections are calculated *per bit*, i.e. the number of observed failures in a register is divided by the number of bits it contains and by the delivered fluence to obtain the SEU cross section as $\mathrm{cm}^2/(\mathrm{bit}\times\mathrm{ion})$; the overall ASIC susceptibility to upsets can be then calculated given the number of (sensitive) bits each register contains. On the contrary CME, SEFI and SEE cross sections are calculated *per ASIC*, i.e. the number of observed failures in a chip is divided by the fluence and cross sections are expressed as $\mathrm{cm}^2/\mathrm{ion}$.

Two GTFE and two GTRC ASICs were irradiated at SIRAD; the ion species, their LET and the average SEU cross sections per bit are reported in Tab. 7.4. Reported data refer to the three 64 bit registers in the GTFEs and the CONF part of the GTRC REG register (22 bits). The GTFE DAC and MODE and the GTRC SYNC registers are not analyzed because of the small number of bits they contain (14, 2 and 5 bits, respectively).

Several things can be noted from the data. First of all the minimum LET of 8.5 $\mathrm{MeV}\times\mathrm{cm}^2/\mathrm{mg}$ is clearly very close to the SEU threshold: only for CONF we observed some upsets (7 after 8×10^7 Si ions per cm^2). Cross sections appear to saturate in correspondence of Ag, even if only a fit can return the correct value. The four registers appear to have a similar behavior within experimental error.

Cross sections are plotted in Fig. 7.8. Data are fitted with a Weibull function (Eq. 5.4.3) and fit results are summarized in Tab. 7.5. Given the few experimental points available the threshold L_0 was fixed to 8.5 $\mathrm{MeV}\times\mathrm{cm}^2/\mathrm{mg}$, as this value was found to be the correct threshold in several test performed on test structures and prototypes [69]. The quality of

the fit is not excellent, probably due to the low number of events observed. In particular the fit for CONF still does not converge: we are forced to fix another parameter to have at least an estimate. We decided to fix the curve width to a weighted average of the values obtained for the other registers.

Ion Species	**Energy (MeV)**	**Range in Si (µm)**	**Surface LET in Si (MeV×cm^2/mg)**
^{28}Si	161.06	62	8.5
^{58}Ni	236.13	34	28.4
^{79}Br	246.84	31	38.8
^{107}Ag	271.88	28	54.7
^{197}Au	275.68	23	81.7

Tab. 7.3 - Ion species used, their LET and range in Si for the Tandem accelerator running at 14.3 MV.

SEU cross sections [cm^2/(bit × ion)]					
Ion	LET [MeV×cm^2/mg]	σ_{CAL} ($\times 10^{-8}$)	σ_{TRG} ($\times 10^{-8}$)	σ_{CHN} ($\times 10^{-8}$)	σ_{CONF} ($\times 10^{-8}$)
Si	8.5	<0.1	<0.1	<0.1	0.4±0.2
Ni	28.4	10.4±1.4	11.3±1.5	9.8±1.4	6.4±0.2
Br	38.8	9.6±1.6	12.8±1.8	7.6±1.4	11.4±2.5
Ag	54.7	31.6±3.5	16.4±2.5	17.2±2.6	19.7±3.9
Au	81.7	20.3±2.8	17.6±2.6	19.1±2.7	24.5±4.7

Tab. 7.4 - SEU cross sections measured at SIRAD on GTFE and GTRC ASICs.

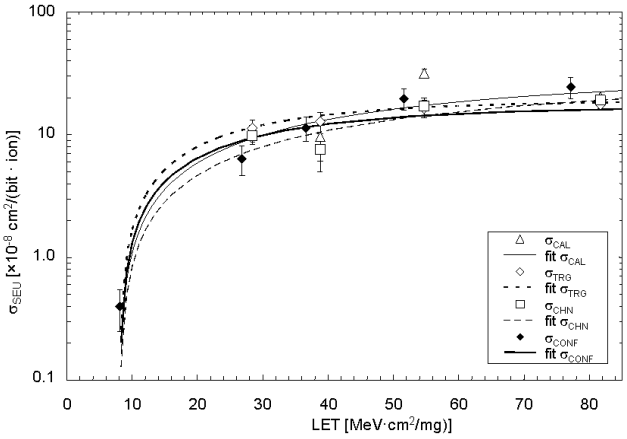

Fig. 7.8 - Plot of SEU cross sections as measured at SIRAD and their fit with a Weibull function.

We can have an estimate of SEU cross section saturation by taking the weighted average of the S values from the data in Tab. 7.5. This way we obtain

$$\langle S \rangle = (1.77 \pm 0.16) \times 10^{-7} \text{cm}^2/(\text{ion} \times \text{bit}) \tag{7.10.1}$$

even if we exclude the CONF value from the weighted average we obtain $\langle S \rangle' = (1.93 \pm 0.28) \times 10^{-7} \mathrm{cm}^2/(\mathrm{ion} \times \mathrm{bit})$, compatible with the former estimate within 1σ.

CME and SEFI cross sections are reported in Tab. 7.6. Notice how the cross sections are calculated per ASIC, given the global nature of these errors. We did not observe any SEFI in the GTFE in this irradiation.

Cross section	S [$\times 10^{-7}$cm^2/(bit $\times$ ion)]	L_0 (fixed) [MeV $\times$ cm^2/mg]	W [MeV $\times$ cm^2/mg]
$\sigma_{\mathrm{SEU-CAL}}$	3.1±1.1	8	57±30
$\sigma_{\mathrm{SEU-TRG}}$	1.8±0.3	8	22±8
$\sigma_{\mathrm{SEU-CHN}}$	2.9±1.4	8	68±46
$\sigma_{\mathrm{SEU-CONF}}$	1.7±0.2	8	25 (fixed)

Tab. 7.5 - SEU cross sections, fitted with Eq. 5.4.3.

Fit results are shown in Tab. 7.7. Once again we fixed L_0 to 8.5 MeV$\times$cm^2/mg; we were forced to fix also W for the GTRC CME to the value measured for the GTFE CME to ensure the fit convergence.

CME-SEFI cross sections [cm^2/(ASIC $\times$ ion)]					
Ion	LET [MeV$\times$cm^2/mg]	$\sigma_{\mathrm{CME-GTRC}}$ ($\times 10^{-7}$)	$\sigma_{\mathrm{CME-GTFE}}$ ($\times 10^{-7}$)	$\sigma_{\mathrm{SEFI-GTRC}}$ ($\times 10^{-7}$)	$\sigma_{\mathrm{SEFI\_GTFE}}$ ($\times 10^{-7}$)
Si	8.5	2.9±0.6	0.3±0.2	4.6±0.8	<0.6
Ni	28.4	11.0±3.3	29.0±5.4	14.0±3.7	<3.8
Br	38.8	18.8±4.8	27.5±5.9	26.3±5.7	<5.0
Ag	54.7	36.7±7.8	30.0±7.1	41.7±8.3	<7.5
Au	81.7	40.0±8.9	22.0±6.6	22.0±6.6	<7.5

Tab. 7.6 - CME and SEFI cross sections measured at SIRAD on GTFE and GTRC ASICs; upper limits are 95% C.L.

Cross section	S [$\times 10^{-7}$cm^2/(ASIC $\times$ ion)]	L_0 (fixed) [MeV $\times$ cm^2/mg]	W [MeV $\times$ cm^2/mg]
$\sigma_{\mathrm{CME-GTRC}}$	30.7±3.7	8	25 (fixed)
$\sigma_{\mathrm{CME-GTFE}}$	32.7±3.7	8	25±11
$\sigma_{\mathrm{SEFI-GTRC}}$	31±10	8	28±22
$\sigma_{\mathrm{SEFI-GTFE}}$	n.a.	n.a.	n.a.

Tab. 7.7 - CME and SEFI cross sections fitted with a Weibull function, Eq. 5.4.3.

Given the parameters reported in Tab. 7.5 and Tab. 7.7 we can try to estimate the maximum expected SEE in the whole TKR for a 5 year mission. It must be stressed that we are not interested in providing a reasonable figure for the SEE rates, rather we need an upper estimate we are sure it will not be exceeded under any reasonable condition.

In Sect. 4.6 we discussed the radiation environment in the LAT orbit, stating that the worst case scenario implies ~ 0.2 galactic ions (GCR) per cm^2 and < 0.1 solar particles (SPE) per cm^2 in 5 years. To add a further safety margin we will assume in our calculations

an ion fluence of 1 ion/cm^2 in 5 years, and we let all ions be above the saturation LET: this way we will consider only saturated cross sections.

In the case of SEU we must take into account the number of register bits each ASIC contains. We will consider all the bits contained in the GTFE registers ($64 \times 3 + 2 + 14 = 208$). For the GTRC we will consider only the SYNC register and the CONF part of the REG register: any bit flip in the remaining part cannot affect the behavior of the electronics, if not by requiring a repetition of a command when an error bit is raised.

SEE	Exstimates for GTFE	Extimates for GTRC
SEU	0.7	0.005
CME	0.04	0.004
SEFI	<0.01	0.004
SEL	<0.01	<0.0007

Tab. 7.8 - Overestimation of SEE events in a 5 year mission for the whole TKR, as obtained by data measured at SIRAD.

Considering a TKR containing 13,824 GTFEs and 1,152 GTRCs we calculate the figures shown in Tab. 7.8. As we did not observe any SEFI event in the GTFEs we irradiated, the figure shown is an upper limit calculated assuming that when no event was observed this meant that less than 3 are expected at 95% C.L. The same procedure was used to deal with SEL rate estimates.

SEU rate constraints are relaxed by the periodical reloading of ASIC configuration: the maximum allowed upset number in a 5 year mission is about 700. From Tab. 7.8 we can expect a maximum of about 1 upset in 5 years in the whole TKR, under the rather harsh assumptions we detailed above.

The SEL rate is of course a much more delicate issue, and the validation request is 0.5 latchups in a 5 year mission. We predict an upper limit of 4.4×10^{-4} at 95% C.L., 3 orders of magnitude smaller than the above limit. We notice that in [91], for the same process but using slightly different design rules[(4)], SEL threshold was measured to be 63 MeV×cm^2/mg (see Sect. 5.7), while previous measurements on GLAST TKR test structures [103] confirm our findings that $L_0 > 81$ MeV×cm^2/mg. Moreover, tests reported in [103], performed injecting charge with a pulsed laser, reached an energy deposition of 200 pJ, equivalent to ~ 600 MeV×cm^2/mg, without the occurrence of a SEL.

The results of our SEE characterization of LAT TKR ASICs is therefore reassuring: no problems whatsoever are expected during the LAT mission due to ion-induced single event effects. In particular the risk of destructive damage to the ASICs appears negligible.

7.11 Effects of SEU hardening

Older versions of the GTFE ASICs (GTFE-F) had the SEU-hardening feature removed from the CAL register. This was decided when a problem was discovered when trying to preset registers which are held by the SEU circuitry: one could not preset them reliably

(4) – in the standard cells used in the digital part of the TKR ASICs, separate metal busses for the ground return and the substrate contacts (without changing the location of the substrate contacts in the cell) were implemented.

and they drew large currents during writing operations. As it was considered unimportant to harden the CAL registers because they can be set before each calibration and are not involved in the normal acquisition procedures, the hardening circuitry was simply removed. This allowed us a fortunate chance to easily test the impact of the design hardening against SEUs on the upset cross sections by making a comparison between SEU cross sections for the unhardened CAL register in GTFE-F ASICs and values obtained for hardened registes.

In Fig. 7.9 SEU cross sections for a GTFE-F as measured at SIRAD are reported; total delivered dose was kept at 10 krd per GTFE: the cross sections are calculated over two ASICs to improve the number of measured upsets and thus reduce the statistical errors.

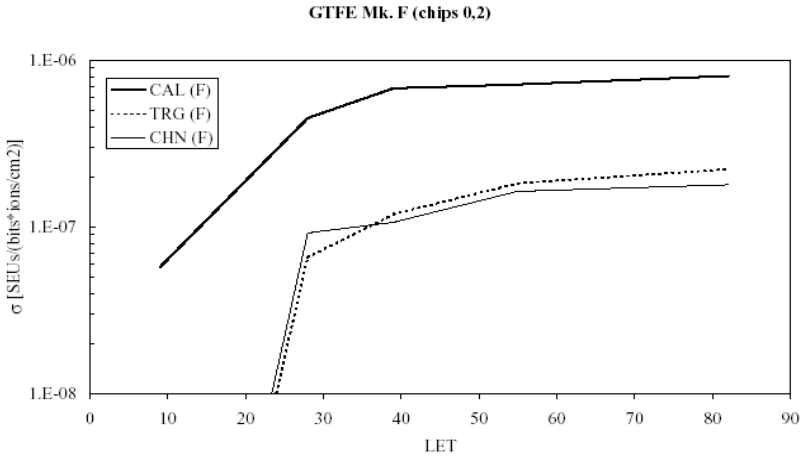

Fig. 7.9 - SEU cross sections measured on a GTFE-F with no hardening of the CAL register; average of two GTFEs.

SEU cross section	S $[\times 10^{-7}\text{cm}^2/(\text{bit}\times\text{ion})]$	L_0 $[\text{MeV}\times\text{cm}^2/\text{mg}]$	W $[\text{MeV}\times\text{cm}^2/\text{mg}]$
$\sigma_{\text{CAL–NONHARD}}$	8.97±0.82	6.58±0.26	28.8±5.3

Tab. 7.9 - Weibull fit of GTFE-F SEU cross section for the unhardened CAL register.

One obtains that the saturation cross section is smaller for SEU hardened registers by a factor ~ 4 ($\sim 8 \times 10^{-7}$ cm^2 for CAL, $\sim 2 \times 10^{-7}$ cm^2 for TRG and CHN). Even more important, the threshold LET appears to be significantly smaller in the case of the non-hardened CAL register.

The parameters obtained by a fit of the CAL experimental points are reported in Tab. 7.9. We do not fit data corresponding to the other registers because the significance is smaller of what measured in the last sections; data in Tab. 7.5 should be considered. Data obtained for the CAL registers, being the involved SEU cross sections 4 times higher, have instead a comparable significance.

The observations we already made on the plot in Fig. 7.8 are confirmed; the uncertainty on the width W is still too big to let us draw conclusions on its possible variations.

7.12 Partial cross sections (1→0 and 0→1)

In Tab. 7.10 the partial cross sections for the 1→0 and 0→1 transitions are measured, as observed during the same irradiation test described in Sect. 7.10. It is clear that the 0→1 transition is more probable by more than an order of magnitude. It is impossible to give a quantitative estimate of the difference: the number of upsets we witnessed for the 1→0 transition after the allowed dose was delivered to the DUT is too low (3/3/4/1/1 for Si/Ni/Br/Ag/Au irradiation) to permit a statistical analysis of the 1→0 curve.

Such difference in the partial cross sections is common, being related to the difference in the critical charge necessary to cause the bit flip. Summing the two cross sections shown here one obtains the overall cross section, reported in Tab. 7.4.

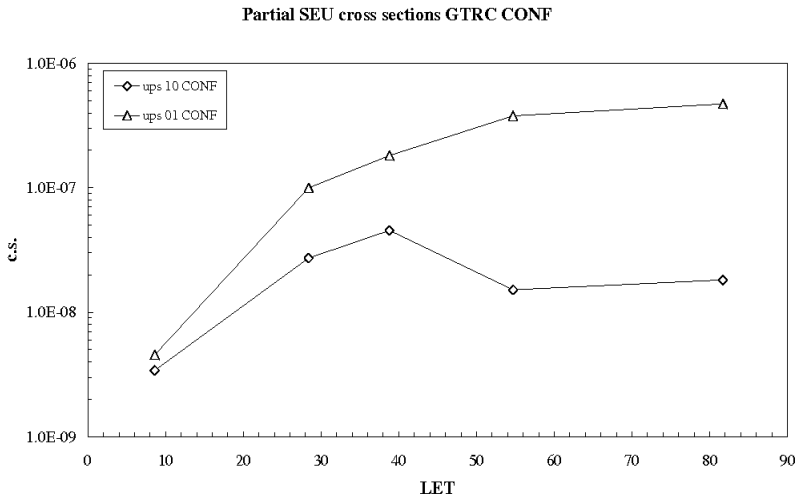

Fig. 7.10 - 1→0 and 0→1 SEU cross sections in the GTRC CONF register.

Partial SEU cross sections [cm^2/(bit × ion)]			
Ion	LET [MeV×cm^2/mg]	$\sigma_{CONF(1->0)}$ ($\times 10^{-8}$)	$\sigma_{CONF(0->1)}$ ($\times 10^{-8}$)
Si	8.5	0.170±0.098	0.23±0.11
Ni	28.4	1.36±0.79	5.0±1.5
Br	38.8	2.3±1.1	9.1±2.3
Ag	54.7	0.76±0.76	18.93±3.8
Au	81.7	0.91±0.91	23.63±4.6

Tab. 7.10 - Partial cross sections measured for the GTRC ASIC at SIRAD.

7.13 Range (in)dependence of SEL predictions

The range of the ions available at the SIRAD beam line (down to ~ 20 μm, see Tab. 7.3 and App. 3) is of no importance for SEU studies, as the thickness of the layer where the CMOS circuitry is implemented is of the order of 1 μm.

While a SEU is fundamentally a surface mechanism, a SEL involves a space charge extending for several micrometers in depth. In this aspect the ions available at SIRAD are quite different from the ions the LAT will encounter after its deployment in orbit: the ranges available at SIRAD can be as small as 23.4 μm (Au) while the ions overcoming the Earth magnetic cutoff will deposit energy in hit devices along the whole thickness. In literature it is generally considered appropriate to test for SEL with ions for which the range in silicon is at least about twice the epitaxial layer thickness, and in this all ions available at SIRAD are adequate. Nonetheless it was believed that a dedicated SEL run with greater ranges would remove all doubts on our SEL rate predictions.

A day was reserved at the Cyclotron Institute of the Texas A&M University (TAMU) [104]. The Radiation Effects Facility is powered by a K500 Superconducting Cyclotron able to provide ions from H to U with energies up to 15 MeV per nucleon (70 MeV for H). The high ranges available let us to place the DUT in air, thus simplifying the irradiation procedure.

Ion Species	**Energy (MeV)**	**Range in Si (µm)**	**Surface LET in Si (MeV×cm^2/mg)**
^{84}Kr	1259	134	27.8
^{129}Xe	1934	120	51.5

Tab. 7.11 - Ion beams used for SEL tests at TAMU Radiation Effects Facility.

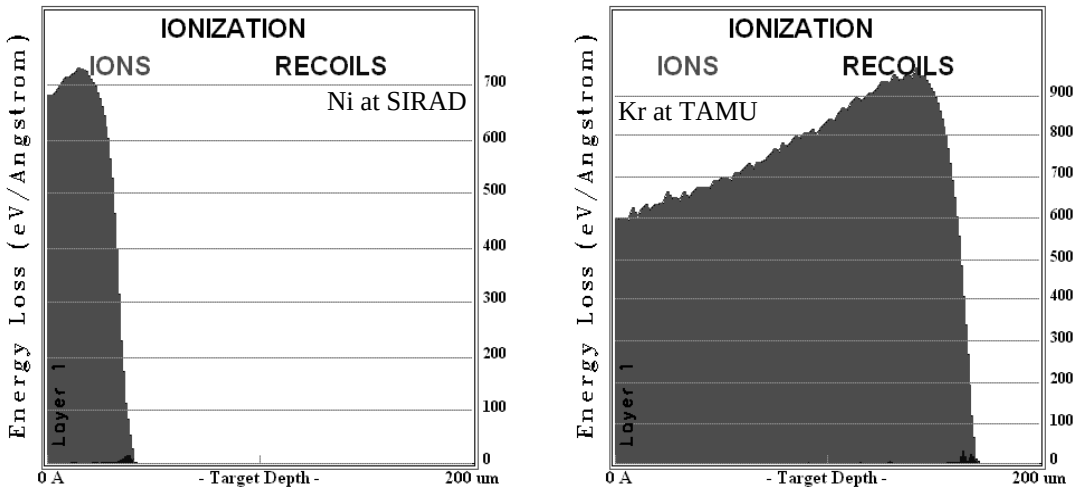

Fig. 7.11 - Ionization profile for Ni at SIRAD and Kr at TAMU.

The selected ion beams are shown in Tab. 7.11. We selected Kr as its surface LET is close to the value we had in our tests at SIRAD with Ni, while Xe has approximately the same surface LET as Ag at SIRAD. We can compare the SEU cross sections, that are range independent as said above, and double check the validity of this test in different experimental conditions. On the other hand, ranges at TAMU are bigger by almost 100 μm: an example of the ionization profile for Ni at SIRAD and Kr at TAMU is shown on Fig. 7.11.

During the irradiations we used the same VME COM board, Interface board and PSB we used at SIRAD. The cables and connectors were the same to minimize the change in

the DAQ system. Only the PC and the VME crate were different: we used an on-board-PC VME board, remotely accessible thanks to a PPP serial connection; the VME crate was provided by SLAC. Two MCMs were tested irradiating both GTRCs and the two outer GTFEs (#0 and #23).

We decided to perform a low flux run on the first MCM first, ϕ=10^4 ions/(cm^2·s), to measure SEU cross sections in conditions as close to those at SIRAD as possible. Results are shown in Tab. 7.12; the values measured at SIRAD are reported in Tab. 7.4. The agreement is only approximate for Kr and Ni, with cross sections measured at TAMU being smaller (2/3 down to 1/2). Xe and Ag (for which the SEU cross sections are saturated) are more compatible, even if some problems seem to persist for TRG and CHN. In any case no clear effect is evident: experimental errors are so big that no clear deviation can be asserted.

SEU cross sections [cm^2/(bit × ion)]					
Ion	LET [MeV×cm^2/mg]	σ_{CAL} ($\times 10^{-8}$)	σ_{TRG} ($\times 10^{-8}$)	σ_{CHN} ($\times 10^{-8}$)	σ_{CONF} ($\times 10^{-8}$)
Kr	27.8	5.6±0.9	5.2±0.9	5.9±1.0	7.7±1.9
Xe	51.5	31.7±2.2	10.5±1.3	8.9±1.2	22.7±3.2

Tab. 7.12 - SEU cross sections measured at TAMU on GTFE and GTRC ASICs.

After 5×10^6 Kr and 5×10^6 Xe ions were delivered to each ASIC, we increased the flux by a factor 10 and delivered another 2×10^7 ions of each kind, for a total delivered dose of $\sim$ 30 krd. Then we replaced the MCMs with the second one and we delivered 2×10^7 ions of each kind to each ASIC.

During the whole test no SEL was observed; the resulting SEL upper limits (at 95% C.L.) are reported in Tab. 7.13. The upper limit on the number of SEL in the whole TKR for a 5 year mission dropped to a total of 5×10^{-4}, two orders of magnitude lower than the estimates obtained at SIRAD.

SEE	Exstimates for GTFE	Extimates for GTRC
SEL	$<4.4 \times 10^{-4}$	$<3.8 \times 10^{-5}$

Tab. 7.13 - Overestimates of SEL events in a 5 year mission for the whole TKR, as obtained by data measured at TAMU.

There was no clear indication of a need for an increase in range beyond the capabilities of the SIRAD beam line. Moreover, the absence of latchups even after such high fluences confirms that SELs are not a concern in LAT operations.

7.14 TID tests

TID tests involve all the ASIC functionalities, as both analog and digital operations are affected by the prolonged exposure to the ionizing radiation.

The test of digital performances is performed by operating the chip registers many times, in a way similar to what was done for SEE tests (with no need for any delay between read and write), and checking for errors.

Analog tests verify the front-end capabilities using charge injection by means of the calibration pulse: channel masking and the effectiveness of threshold discrimination are verified.

Electronic noise measured at a set threshold is particularly important, as it affects directly the L1T and the detector dead time. Electronic noise is usually described as an *Equivalent Noise Charge* (ENC), i.e. by the amount of electrons that, injected in the electronic channel would give a signal of similar amplitude. Generally, the major noise source is the first amplification stage, depending on the input capacitance. Flicker and thermal noise in the input MOSFET channel, and thermal noise in the microstrip polysilicon resistor all have a role in making the preamplifier noisy. All these contributions add and are usually parametrized as

$$ENC = a + b \cdot C_{tot} \tag{7.14.1}$$

where C_{tot} is the capacitance of the Si detector as seen by the electronics. Typical values are some hundreds of electrons for a, and some tens of e^-/pF for b.

Here we are particularly interested in the intrinsic noise of the GTFE amplifier stage (the a parameter in Eq. 7.14.1), i.e. the noise measured without the silicon detector, as this is one of the key parameters we are required to test under irradiation. Tests performed on GTFE test structures give $a = 174\ e^-$ and $b = 32\ e^-$/pF, while for a TKR SSD $C_{tot} = 47$ pF[(5)]. These figures mean that the amount of noise given by the GTFE is ~ 10 times less than the contribution depending on the SSD. In normal conditions the ASIC noise is therefore negligible: we have to verify this is true even after irradiation. The presence of the single threshold discrimination allows us to estimate the noise rate f at a certain threshold setting T (in equivalent electrons) to be

$$f = f_0 \times \exp\left(-\frac{T^2}{2 \times G \times ENC^2}\right) \tag{7.14.2}$$

where G is the channel gain, so that $log(f)$ should depend linearly from threshold.

Finally, satellite operation forces strong limitations on the power available to the electronics. Hence, power consumption is monitored before, during and after irradiation.

7.15 TID irradiation procedures

Given the expected dose of ~ 0.8 krd on the outer regions of the TKR, and allowing for a 5× engineering safety limit, we obtain a limit of ~ 4 krd in a 5 year mission. In view of the possible doubling of the GLAST mission duration we decided to test the TKR ASICs up to 10 krd (see [100],[101]). Tests must be performed *before irradiation* to check the correct behavior of the brand new ASICs, and *after irradiation* to look for changes. Irradiations are performed in 2.5 krd steps, and test procedures required that ASICs should be characterized after each step. Following a first irradiation campaign on test chips it appeared evident that the delivered dose could not in any way harm the

(5) – this value is not expected to change significantly after irradiation; see [105], [106] for details on the performances of irradiated silicon detectors.

ASIC functionalities; because of this the test procedures were revised and currently tests are usually performed only after the total desired dose has been delivered, with a notable exception: in any case power consumption *must* be measured after every irradiation step.

During all ^{60}Co irradiations a Pb-Al shield like the one described in Sect. 6.1 must be used. This ensures that there is no dose enhancement due to low energy photons. In Fig. 7.12 the typical setup we employed in ^{60}Co irradiations is shown. An Al box is covered with a Pb sheet to realize a Pb-Al shield that encloses the DUT (see Chap. 6). The DUT (in this case a MCM) is placed inside the box and held firmly flat against it by an aluminum plate locked in position with a screw. The cables on the right connect the DUT to the interface board (not shown). On the far left a metal cone can be seen: this is the top of the Co source holder, in the picture still inside the Pb case (below the table). When the source is activated, an automated cable-and-pulley system extracts the holder so that the Co cylynder faces the DUT. Extraction requires ~ 5 seconds.

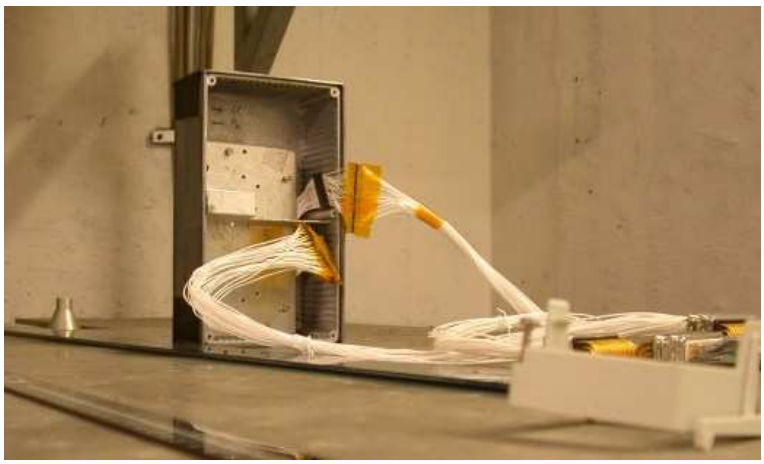

Fig. 7.12 - A MCM immediately before gamma irradiation at LNL; the DUT is inside the Pb-Al box, behind the plate that holds it firm, on the far left the top of the Co source holder can be seen.

7.16 Functionality tests

The first test of the basic digital functionalities uses the same procedure employed for SEU tests: picket fence patterns (`1010`) are written in all ASIC registers and read back, and errors are reported. As any corruption cannot be attributed to a transient event (tests are not performed under irradiation) we can set the delay between read and write to zero. This way we can easily test 1000 read-write cycles in a few seconds, ten times the amount required by the TID test plans [100],[101].

Tests are repeated employing all possible GTRC IDs (0–15): normally the layer ID is hardcoded in the flex cable connecting the GTRC with the corresponding GTCC, but in our DAQ setup the four pads are connected to four of the LVDS outputs of the VME COM board (see Fig. 3.12, pads A0–A3). This way we can test that each GTRC performs properly regardless of its placement on the TKR.

Next, hard and soft reset are tested: the usual patterns are loaded in the GTRC and GTFE registers, a reset command is sent to the ASIC under test and the register contents are downloaded. GTRC resets properly, i.e. after the reset cycle the registers contain their

default values, as detailed in Tab. 3.4. On the contrary the soft reset of the GTFE ASIC does not produce the expected results: the patterns loaded in the registers are still there after the reset command. Lacking a hard reset function, this means the register contents must be reloaded to switch back to their default values. As this is in any case the correct procedure this is not seen as a problem. More important to our purposes, this problem is not related to radiation damage as it is present before the chips are exposed to radiation.

No changes are observed in the digital operations after irradiation. With the minor exception of the GTFE soft reset, as explained above, all functionalities perform correctly and no problem was ever observed.

Given their exhaustiveness, TID functionality tests are commonly used to test the data acquisition system each time it is assembled.

7.17 Noise rate

As explained in Sect. 3.7 the enabled channels in the GTFE are OR-ed to generate a fast-OR signal; next all GTFEs propagate this signal OR-ing it with the one coming from the neighboring GTFE in the MCM. This *layer-OR* is used as trigger request. The noise rate depends on the set threshold, as only noise spikes above threshold concur in forming the *layer-OR*, so the noisiest channel dominates the OR channel. Validation requirements indicate that, with a threshold of 10 DAC channels, a trigger rate less than 100 Hz per ASIC is needed to ensure the expected TKR performances.

Clock is not required to the OR generation, and using a probe or modifying the test MCMs one could access it directly and measure the noise rate with a simple frequency meter. Nonetheless, our need to access it through the active GTRC requires the clock be provided. This means a more subtle approach must be used to extract noise rate information.

The procedure we adopted is described here in some detail. First we load GTRC registers with an appropriate configuration. Next, all GTFE are muted disabling trigger and channel masks, and setting the DAC threshold to its maximum. Then, in the GTFE selected for the test, the threshold is set to the chosen value and all channels are enabled. Now the test program:

- resets the trigger counter
- clocks the chip and wait for 0.5 sec
- reads the trigger counter

The 0.5 seconds delay in which we measure the noise frequency is split in 1000 smaller intervals due to the COM board memory limitations. The test program therefore resets the MCM, loads each ASIC with the configuration described above and waits 10,000 clock cycles counting the trigger hits. The procedure is repeated 1000 times to have enough statistics, corresponding to a total of 0.5 s in which the layer-OR is monitored.

The trigger rate measurement is repeated from left and right. The test application returns the noise frequency (in triggers per second), while separate left and right readings let us check that the GTFE is working the same way under both conditions and that both GTRCs propagate the trigger correctly.

A first noise rate scan performed with the procedure described above returned the plot shown in Fig. 7.13. Instead of the expected exponential decay, the noise rate reached a plateau at a value of 2000 Hz for the threshold in the range 7–11 DACs. The value

measured at the plateau is very suspicious: 2000 Hz means 1000 noise hits in the 0.5 s time window, that is exactly one hit in each of the sub-intervals. The test program was modified to return the time elapsed, in clock cycles, before each trigger hit: from the results shown in Fig. 7.14 one observes that all "noise" hits happen in the first 50 clock cycles of each sub-interval.

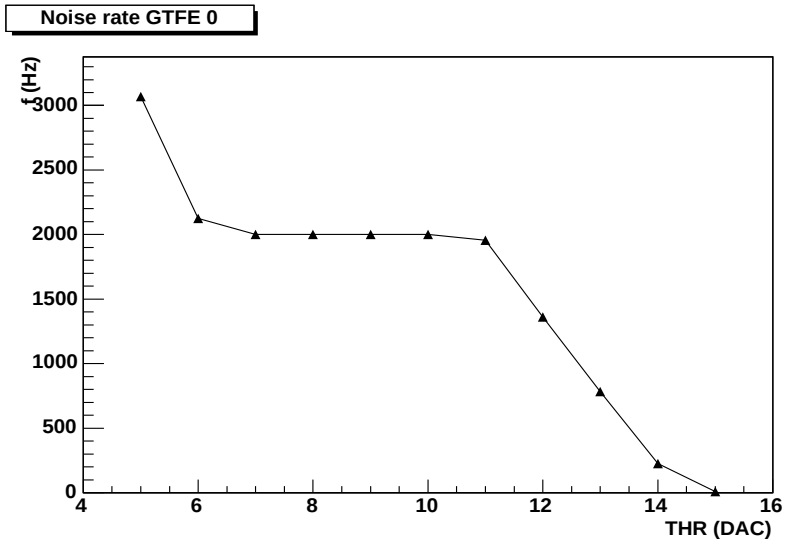

Fig. 7.13 - Noise rate versus threshold for a GTFE without enough delay before counting mode is enabled.

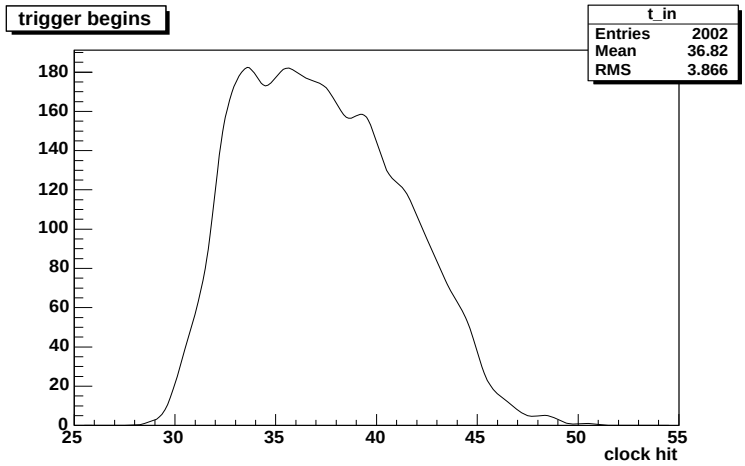

Fig. 7.14 - Start of layer-OR hits for test program run without enough delay before counting mode is started.

For completely random hits one would expect to find an uniform distribution within the sub-intervals, 10,000 clocks long. This lead us to suppose some incorrect behavior of the ASIC or some problem in our procedure. As a possible explanation we can assume that the GTFE requires some small time to stabilize after a reset before the analog front-end works properly. The delay between reset and the start of the counting procedure was set to 50 clocks; adding another 500 clocks before enabling the trigger counter completely solves this problem: now the noise rate versus threshold plot is as expected and, setting

the threshold to have a noise rate of several kHz, the noise hits are evenly distributed between 0 and 10,000 in all subintervals. It must be stressed that this is not going to be an issue in space operations, even if a stray trigger request should actually happen on the rare occasions when chips are reset.

With the updated test program we measured the noise rate for a large number of GTFE ASICs, before and after ^{60}Co irradiation. In all cases the requirements (noise rate less than 100 Hz at THR=10 DAC) were met, up to doses of 10 krd. A sample measurement of the same GTFE ASIC before and after irradiation is shown in Fig. 7.15: the noise rate was measured both from the left and from the right. From Eq. 7.14.2 linearity is expected in the logarithmic plots, nonetheless saturation effects usually appear at lower thresholds and higher rates.

The effect of gamma irradiation appears in some way to be unexpected, as noise seems to diminish. As a possible explanation we notice that the threshold offset or the shaping time might change slightly due to irradiation, and therefore reduce the ENC. Gain could diminish, too, producing a similar result; however, in the next sections we will see how this effect is negligible. We can estimate how the gain should change to account for the observed noise decrease. We fit the 6 points for the un-irradiated and irradiated curves where linearity is fair, i.e. those at higher thresholds, obtaining a slope of $-(2.98 \pm 0.18)$ 1/DAC for the not irradiated curve and $-(4.14 \pm 0.17)$ 1/DAC for the irradiated curve. As this slope is $1/(2 \times G \times ENC)$ we would derive a $\sim 30\%$ decrease in gain.

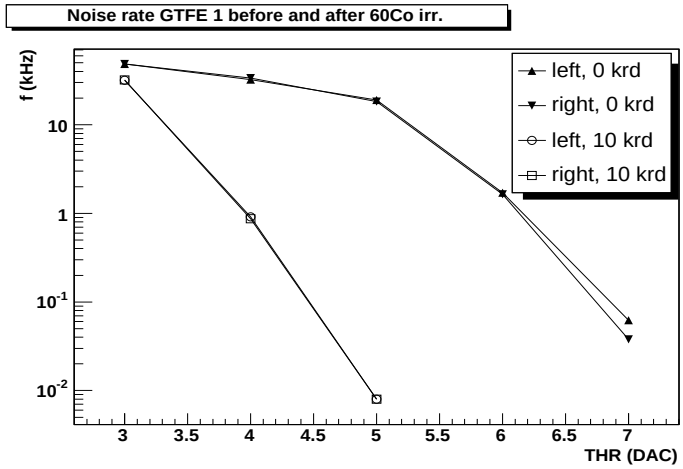

Fig. 7.15 - Noise rate for a GTFE, before and after irradiation with ^{60}Co gamma rays, read using both left and right GTRC.

7.18 Charge injection, threshold and mask functionalities

This set of tests verifies that:

- the charge injected in a GTFE channel, when above threshold, is detected with 100% efficency;
- all 4 GTFE data buffers store correctly event data;
- masked channels are effectively silenced.

Threshold is set to 20, equivalent to $\sim$ 1 fC, and the calibration pulse is set to 40, equivalent to $\sim$ 3 fC (see Fig. 3.11); this way all electronic noise is cut while the injected

charge remains well above threshold.

First, each odd GTFE channel is pulsed 100 times and event data are stored in GTFE buffer 0. The event buffer is downloaded and its contents are checked for missing hits. This is repeated for even channels, and then for all four data buffers.

Next, a buffer is selected and 1000 pulses are sent, to have more statistics and verify that pulses are recorded with 100% efficiency.

Finally, all channels are disabled in the MASK register, and again 100 pulses are sent. No channels must be found in the data output.

All the tests above are repeated using the left and the right GTRC. No problem was ever observed, either before or after irradiation: all tested GTFEs performed as specified.

More details on the front-end noise are given on the next section.

7.19 Gain scan

Though not strictly required to validate the TKR ASICs, gain was measured for the GTFE channels, before and after irradiation.

The internal calibration system is used to inject a (rather high) fixed charge into each channel and a scan over the threshold level is performed. Being data readout for each channel completely digital (i.e. only a 0 or 1 can be read) it is necessary to measure the channel occupancy as a function of the threshold.

Let Q be the injected charge; the peak height after the amplifier stage will be

$$H_{\text{out}} = s + n \tag{7.19.1}$$

where s and n are the signal and noise contribution respectively. s will be distributed like a Dirac delta, function of the injected charge and the amplifier gain G as in

$$s = \delta(G \cdot Q) \tag{7.19.2}$$

We can assume that n follows a normal distribution with null average and width σ_n:

$$n = N(0, \sigma_n) \tag{7.19.3}$$

then,

$$H_{\text{out}} = N(G \cdot Q, \sigma_n) \tag{7.19.4}$$

The probability for H_{out} to be greater than the threshold level T is given by

$$Occ = 1 - erf\left(\frac{T - G \cdot Q}{\sigma_n}\right) \tag{7.19.5}$$

where `erf()` is the Gaussian error function, here defined as the normalized area of a Gaussian centered in $x = 0$ with width 1. Occ is then the expected occupancy after a great number of charge pulses are sent and statistical fluctuations can be ignored.

A fit of the occupancy-versus-threshold curve would give easily both gain and noise. The noise measure can be subsequently converted in the usual expression in equivalent electrons:

$$ENC = \frac{\sigma_n}{G} \tag{7.19.6}$$

We are not interested in characterizing the front-end, but rather to monitor if any change due to irradiation happens with a screening procedure. The simplest way of measuring the gain is therefore to perform the occupancy versus threshold scan as explained above, but G (or more correctly, $G{\cdot}Q$) is taken to be the threshold value at which 50% occupancy is measured.

In particular, we measure the gain at two calibration pulse widths (10 and 20 DACs) with 100 pulses. An example of a typical gain map of a GTFE, before and after ^{60}Co irradiation, is shown in Fig. 7.16. The average gain does not change after irradiation and the channels with the biggest decrease do not reach in any case the 30% variation required to justify the apparent decreasing in the noise levels after irradiation of the GTFE.

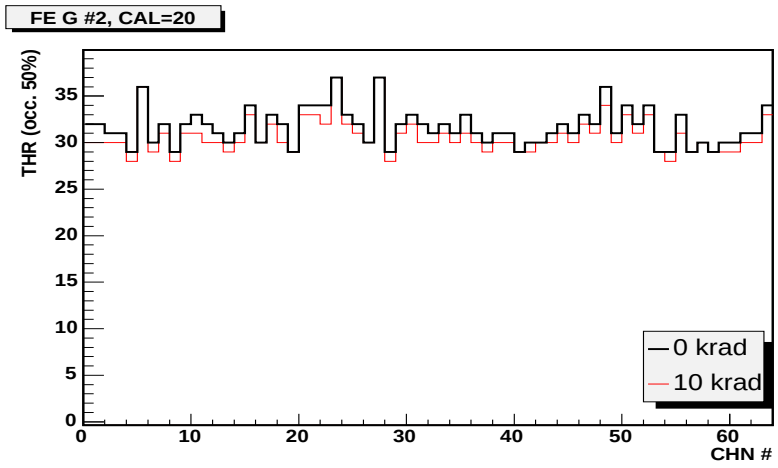

Fig. 7.16 - Gain as measured on all 64 channels of a GTFE before and after ^{60}Co gamma irradiation, delivered dose 10 krd.

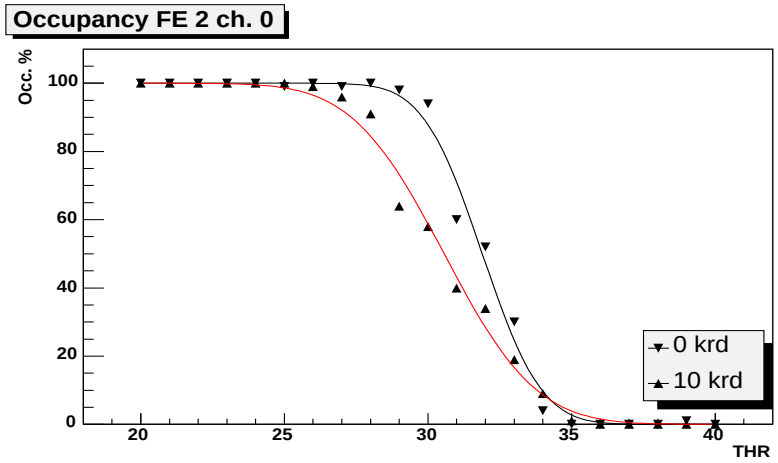

Fig. 7.17 - Occupancy for GTFE channel 0 of Fig. 7.16; fit with (1-erf) is shown.

A more detailed analysis can be performed: in Fig. 7.17 the occupancy for channel 0 of

the GTFE in Fig. 7.16 is shown, both before and after irradiation. Fitting with Eq. 7.19.5 one obtains gain and noise data for the selected channel. Results are shown in Tab. 7.14, together with the $G \cdot Q$ obtained taking the point of $Occ = 50\%$.

The example data in Tab. 7.14 let us address several issues. First, the fast method for determining the gain appears justified, as long as the occupancy curves follow the erf distribution. Second, gain does not diminish significantly after irradiation. Third, the channel noise (σ) actually increases, as expected, after irradiation.

This means the decrease in the noise rate on the *layer-OR* line after irradiation is due to some other effect. A significant decrease in gain being excluded, the most probable cause is a shift in the threshold analog levels. A shift of 2 DAC channels after irradiation would completely account for the observed noise rate values. Given that the delivered dose for testing (10 krd) is 12.5 times the expected dose for a 5 year mission, the effect appears to be negligible. In any case gain and noise will be monitored on-line during the satellite operations, and corrections on the threshold levels could be applied.

before irradiation			after irradiation		
	fit	50%		fit	50%
$G \times Q$	31.83±0.02	32	$G \times Q$	30.56±0.03	30
σ	2.29±0.04	-	σ	3.57±0.06	-

Tab. 7.14 - Gain and noise for GTFE 2 channel 0, obtained by fit and taking the point at $Occ = 50\%$.

As seen in Sect. 7.18, the noise rate measured for the LAT front-end ASICs, before and after irradiation, indicates no cause for worry: measured parameters fall within constraints, and even a more detailed analysis of gain and noise performed on a channel-by-channel basis, as shown on this section, indicates that GTFE performances are more than adequate even after 10 krd.

7.20 Power consumption

Power consumption in satellite missions is critical. For this reason we monitored the amount of current drawn by each MCM before and after irradiation, and after each 2.5 krd step.

Requirements indicate that the maximum allowed increase is 20%. We monitored the power lines reaching the MCM, so the currents we measured are actually the sum of all the ASICs on the board.

Typical values for a test MCM carrying seven GTFEs and the two GTRC are $\sim$ 14 mA drawn on the AVDDA line, $\sim$ 5 mA on AVDDB and $\sim$ 15 mA on DVDD, for a power consumption of $\sim$ 20 mW, $\sim$ 12 mW and $\sim$ 38 mW, respectively. No significant increase after irradiation is observed: fluctuations within 5% arise between different measurements, depending on temperature, humidity, conditions of the contacts, etc., while after irradiation the increase is well below this margin.

From these figures we can calculate then a power dissipation of $\sim$ 70 mW for $64 \times 7 = 448$ channels, i.e. of 156 μW per channel; this is a slight overestimate as in the full-sized MCMs there will be 24 GTFEs but still only two GTRCs, so the net DVDD consumption is somewhat smaller in comparison. Still, we lie well within the LAT requirements.

7.21 SEE tests of DAQ ASICs

Given the succesful SEE characterization of TKR ASICs, we agreed to test at the SIRAD facility in Legnaro also the DAQ ASICs: the two cable controllers and the LVDS translator. Ion beams employed in the SEE characterization are those in Tab. 7.3, but Au was discarded as cross sections are expected to saturate before the LET corresponding to Ag, as observed for the TKR ASICs. At the end of the irradiations each part had received a dose of 10 krd [107].

Two ASICs of each kind (GTCC, GCCC and GLTC) were placed on custom test boards designed at SLAC. The test system was developed at SLAC and, besides many minor differences, worked exactly like the one we developed in Padova for the TKR ASICs: "picket-fence" bit patterns (`1`→`0` and `0`→`1`) were written into the chip registers and were read back after 10 seconds. Errors were counted and cross sections calculated. As SEL robustness for the Agilent 0.5 μm technology was already demonstrated with the TKR ASICs no SEL was expected, so we decided not to build a SEL-safe power supply for the DAQ. As the one used for the TKR MCMs was not easily reconfigurable, we simply used the over-current protection of the Agilent HP3631 power supply.

DAQ SEE cross sections [cm^2/(ASIC × ion)]						
Ion	LET [MeV×cm^2/mg]	$\sigma_{GTCC-SEU}$ ($\times10^{-6}$)	$\sigma_{GTCC-CME}$ ($\times10^{-6}$)	$\sigma_{GCCC-SEU}$ ($\times10^{-6}$)	$\sigma_{GCCC-CME}$ ($\times10^{-6}$)	$\sigma_{GLTC-SEU}$ ($\times10^{-6}$)
Si	8.6	0	0.4	0	0.67	0
Ni	28.4	1.95	4.39	3.10	7.99	0.10
Br	38.8	3.45	6.14	6.55	7.37	0.06
Ag	54.7	5.08	7.83	9.58	12.67	0.58

Tab. 7.15 - Soft SEE cross sections measured on the DAQ ASICs at SIRAD, from [107].

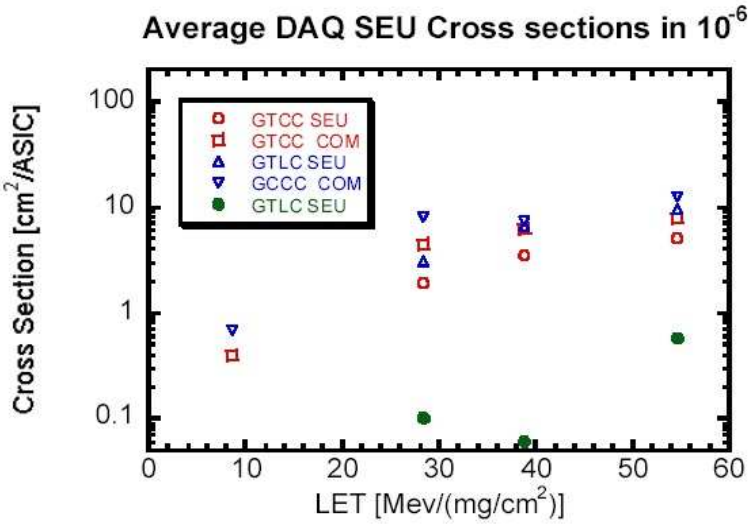

Fig. 7.18 - Soft SEE cross sections per DAQ ASIC as measured at the SIRAD, from [107].

No SEL was observed: we calculated an overestimate for SEL rates in GLAST DAQ

electronics with the procedure described in greater detail in Sect. 7.10: zero observed events translates into less than 3 at 95% confidence level. Assuming that all the ions hitting the DAQ electronics in space have a LET similar to the maximum LET we used in our test (Ag) we can divide by the total delivered Ag fluence (6×10^6) and obtain an upper limit for the SEL cross section of 5×10^{-7} SEL·cm^2/ASIC. As it was done in Sect. 7.10 we multiply this by a fluence of 1 ion/cm^2, which is a safe upper limit for the expected fluence in a 5 year mission, obtaining a SEL probability of 10^{-4}, where we assumed the presence of 64 GCCC, 128 GTCC and 18 GTLC in the LAT. We can therefore consider the probability of a SEL happening to the LAT DAQ electronics in the GLAST mission to be negligible. Cross sections (per ASIC) relative to soft SEU events are reported in Tab. 7.15. Both SEU and CME cross sections appear to saturate at $\sim 10^{-5}$ cm^2/(ASIC×ion); GLTC is an exception as CME were not observed and SEU cross section remains below $\sim 10^{-6}$ cm^2/(ASIC×ion).

7.22 TID tests of DAQ ASICs

TID tests of DAQ ASICs are currently under way at the CNR-ISOF ^{60}Co irradiation facility at the INFN National Laboratories of Legnaro and will be completed in the first month of the next year as the final flight lots will be produced. Total delivered dose, dose rate and details of the measurements are described in [108]. ASICs shall receive a total dose of 10 krd, given in four steps of 2.5 krd, with a dose rate of less than 3 rd/s. After each irradiation step power consumption must be measured; the overall increase after 10 krd must be below 20%.

The ASICs reside in Burn-in Boards, which in simplified form takes the place of the TEM. The 20 MHz clock is generated by ancillary electronics placed on the test boards; these components must be shielded from radiation with Pb bricks in front of them. The usual Pb-Al shielding is used, as described in Chapt. 6, to avoid dose enhancement by low energy photons. After the irradiation phase, DUTs are moved to the laboratory and tested, to ensure all digital functionalities perform correctly.

The first results of tests of GTCC and GCCC ASICs are reported in [109]. No significant increase in power consumption is observed (currents after irradiation change less than 2% with respect to the values measured before irradiation). Power consumption was monitored again 9 and 11 days after irradiation, with identical results. Test of digital functionalities showed no deviation after irradiation.

7.23 SEE test of COTS components

The GLAST LAT group tested the radiation hardness of MAXIM DC-DC converters as a preliminary step for their use as flight parts. DC-DC converters are used in the spacecraft as voltage converters; we used in this test parts from MAXIM, described in Tab. 7.16: the first is developed in Bipolar technology, the other two are CMOS. It must be noted that the use of *Components Off-The-Shelf* introduces great advantages, first of all their limited cost with respect to avionic or military parts, and availability.

Suitable TID hardness was previously demonstrated: the same models described here were irradiated in the UCSC ^{60}Co source at a dose rate of 4.5 krd/hr. The input and output power was monitored and the chips were irradiated until they obtained a negligible current draw (0.1 mA) and no output voltage. The CMOS parts survived a TID in excess

of 20 krd, while the bipolar device was still functioning after 400 krd, although with a somewhat lower efficiency [110], here defined as the ratio of output power to input power:

$$\mathrm{Eff} = \frac{\mathrm{P_{out}}}{\mathrm{P_{in}}} = \frac{\mathrm{V_{in}} \cdot \mathrm{I_{in}}}{\mathrm{V_{out}} \cdot \mathrm{I_{out}}} \tag{7.23.1}$$

SEL resistance has to be proven too. Here we report the results from a latch-up testing at the SIRAD beam line at the INFN Laboratories of Legnaro (LNL) of three parts identical to the ones irradiated at UCSC.

Part	Tech.	Vin [V]	Iin [mA]	Rout [Ω]	Vout [V]	Iout [mA]	Eff.
MAX724	Bipolar	24	148	2.14	1.82	850	0.44
MAX1523	CMOS	5	12	3017	11.8	4	0.76
MAX1809	CMOS	5	265	1.56	1.12	720	0.61

Tab. 7.16 - Table of MAXIM DC-DC converters tested at SIRAD; parameters as measured before irradiation.

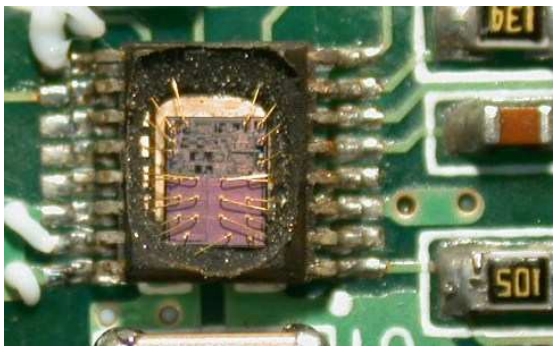

Fig. 7.19 - A delided MAX1809 placed on the SLAC test board.

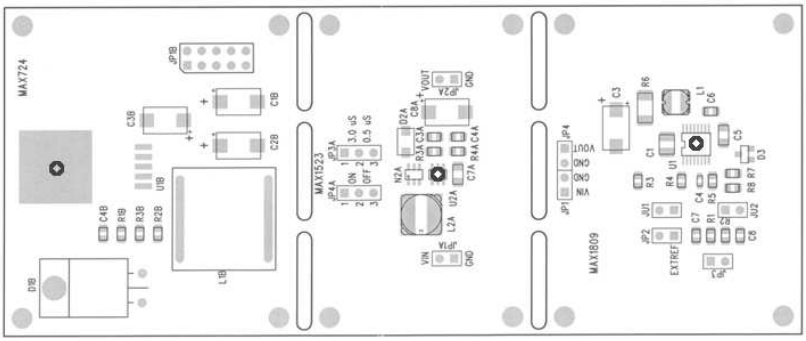

Fig. 7.20 - Custom board hosting the three MAXIM DC-DC converters; black circles indicates the DUTs.

The selected ion beam was Bromium with an LET = 38.6 MeV/(mg/cm^2), and the delivered fluence was 10^7 cm^{-2} for each of the three DC-DC converters, equivalent to a delivered dose of $\sim$ 6.2 krd. The parts were placed on a custom board, designed at SLAC to mount the DUTs and the necessary auxiliary components. Heat sinks were added to

put in thermal contact the parts under tests and the vacuum chamber, as conventional heat dissipators do not work in vacuum and PCB boards conduct heat very poorly. Cables connect the converters output stages with the load resistors specified in Tab. 7.16. Parts have been de-lidded to remove the plastic cover allowing the beam to hit the silicon die: given the limited range of the heavy ions the plastic case would completely absorb the beam. The irradiated parts were powered, but without the latch-up detection circuit described in Sect. 7.5, i.e. they were only protected by the over-current protection of the Agilent HP3631 power supply set to twice the nominal currents.

The output stages of the three converters were connected to pass-through BNC connectors on a flange and the load resistors were placed outside the vacuum chamber. This introduces a small uncertainty on the value of the resistive load, especially given the small resistances involved (as small as 1.5 Ω), but this setup proved necessary given the rather big power dissipated by the load resistors (as high as 1.5 W): resistors could then be firmly pressed against the steel of the vacuum chamber support to help heat conduction.

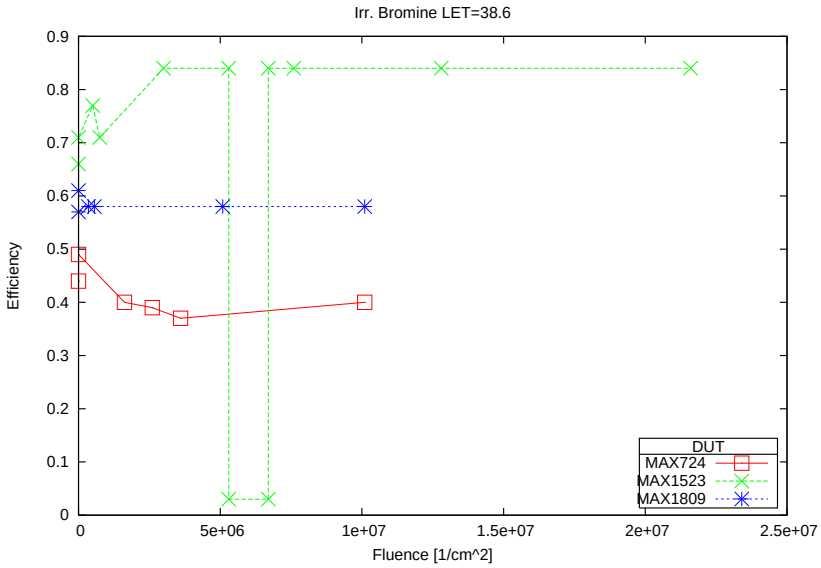

Fig. 7.21 - Effifiency versus fluence for the three MAXIM converters; after the SEL event for MAX1523 the output power remains off until main power is cycled.

The status of the power supply and the digital multimeter measuring the output current, both placed within the experimental room close to the vacuum chamber, was monitored constantly both by remote GPIB interface and with the help of a video camera. This allowed us to measure the efficiency during the whole irradiation and observe the effects of the delivered dose on the converters' performances.

One SEL was observed in one of the converters (MAX1523), after a fluence of 5×10^6 cm^{-2}. The power in the MAX1523 output stage dropped to zero and remained such until the power supply was reset. We continued the irradiation for the remaining 5×10^6 cm^{-2}, and then for another 10×10^6 cm^{-2}, without observing any other latch-ups. No SEL was observed in MAX1809 or MAX724 [111].

Efficiency is plotted as a function of the fluence in Fig. 7.21. We observe that only MAX724 shows an overall decrease in the efficiency, while for the other two parts the

effect of the delivered dose appear to be a small improvement followed by a plateau. This is consistent with results in [110] in the sense that the efficiency starts to drop only after $\sim$ 20 krd are delivered. The small increase could depend on a sizeable increase in temperature of the DUT and the companion electronics in the few minutes the irradiation lasted, as heat dissipation within the vacuum chamber was still far from excellent.

8 Integration and Test

8.1 Integration

TKR assembly and testing are responsibility of INFN. Flight parts are being tested and assembled into working towers in the INFN laboratories in Pisa. Once the towers are completed, they are sent to SLAC for the final tests and their insertion on the LAT grid, together with the calorimeter.

Hamamatsu SSD sensors are tested in the INFN-Pisa cleanroom. The incoming tests include measurements of leakage current, breakdown and depletion voltage, and a check of geometrical constraints. Accepted sensors are then assembled by Italian industrial partners (Mipot, G&A) into ladders, pads are bonded and bonds are encapsulated. Non-conformity of incoming SSD is about 0.5%, while ladder assembly yield is about 98%[(1)].

TKR MCMs are received in Pisa from SLAC and tested with the same procedures described in the following sections. Accepted MCMs are then sent to G&A together with SSD ladders for the tray assembly. Once trays are received back by INFN they are thoroughly tested and the accepted ones are assembled into a TKR tower. The next sections will deal in detail with the tray acceptance test and assembly procedures, in which we took part in Pisa.

8.2 EGSE

The whole test bench for a hardware subsystem is labeled EGSE, from *Electrical Ground Support Equipment*. The EGSE used to test the TKR trays is composed by

- a *Tower Electronic Module* (TEM), to access TKR components and ensure all TKR functionalities;
- a *Power Supply Assembly* (PSA), providing all digital and analog voltages to TKR and CAL; furthermore it provides the bias voltage to TKR and CAL sensors;
- a 28 V power supply; it simulates the power provided by the spacecraft supplies;
- a VME *LAT Communication Board* (LCB), emulating the Power Distribution Unit and Global Trigger (GASU) functionalities; it provides the clock, manages the trigger and has two FIFOs for commands and events sent to the TEM;
- a VME Motorola computer (MVME2304) managing the whole system and interfacing the EGSE with the operator PC.

8.3 Online software

From the point of view of control software, the LAT is represented as a hierarchical network of nodes, as shown on Fig. 8.1.

At the highest level we have the 16 TEMs and the GASU, containing the AEM (ACD Electronic Module) and the Global trigger Electronic Model (GEM).

(1) – about half of non-conformant ladders were due to broken edges; ladder storage was redesigned to further increase the ladder assembly yield.

Each TEM contains the calorimeter electronics (prefix `GC`), the tracker electronics (prefix `GT`) and the Trigger Interface Controller (GTIC). The GTIC allows the operator to manually access the triggering system: it can be used to enable/disable event readout and to select the trigger primitives (three-in-a-row, external trigger, read-on-command).

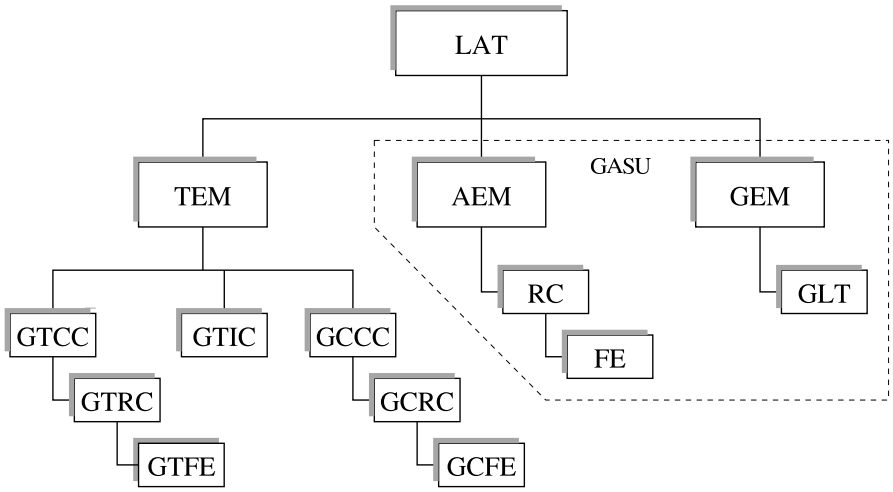

Fig. 8.1 - LAT hierarchy as implemented by the online software; the TEM structure is replicated 16 times.

TKR and CAL structures are identical: first the operator selects a tower ID, then he can access the different cable controllers (CC), and from there he can follow the LAT hierarchy down to a specific layer and to its Readout Controller (RC). The last branch is constituted by the Front End electronics (FE) attached to each RC. For each node registers can be accessed, monitored and modified, and commands can be sent to the selected ASICs.

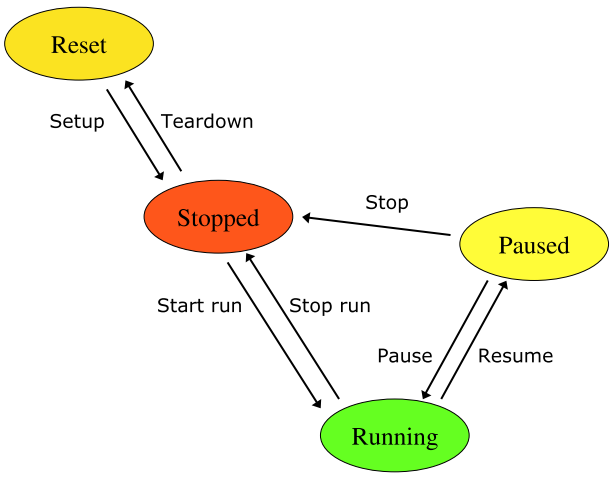

Fig. 8.2 - Transitions in Run Control; to each corresponds a method to be implemented by the operator.

LATTE is the software environment that allows one to control the various nodes. It consists of a series of low level routines implementing LAT hierarchy, managing all LAT

functionalities, triggering and data flow. Auxiliary tools, for graphical interface and data storage, are included. All LATTE routines are written in Python, to allow for multi-platform operation and easy upgrade.

The higher level control, *Run Control*, is implemented as a finite state machine (FSM). The operator loads a test routine and then controls its behavior with the most familiar set of buttons: play, stop, pause and eject. Each button causes a change of state, as described in Fig. 8.2. A routine corresponds to each change of state, and it is the operator's responsibility to implement it in the test scripts.

Test results are commonly saved as HTML files, where the test result is clearly indicated for the tested component, automatically generated from the DUT specifications. Test details are described, such as the employed configuration, and relevant plots and ntuples are included as links.

A database was developed in Pisa to guide the operator through the test procedure and to automatically upload output files to the online database.

In the next sections the most common tests for TKR electronics are described, and some results are shown.

8.4 Register Tests

Both MCMs and trays are tested to ensure that all registers can be accessed and programmed correctly. *Picket-fence* bit patterns (1010... and 0101...) are loaded into the writable part of both GTRCs and GTFEs, both accessing all ASICs one by one and using a broadcast command. Each ASIC is then read back and the register contents are compared to the input pattern. Any error is reported and malfunctioning ASICs are identified.

8.5 Reading Configuration Test

For each MCM, each GTFE can be read either from the left or right GTRC. The choice of the split point in the GTFE chain is called a *reading configuration*; 25 different configurations are possible. This allows for a great flexibility and redundancy in the readout process, minimizing the impact of the failure of a GTFE or a GTRC.

To detect failures each MCM is tested in three configurations: first all front end ASICs are read out by the left Readout Controller (*24–0*), then all GTFEs are read out from the right (*0–24*) and finally the readout is split in half (*12–12*). Charge is injected into randomly selected channels, one for each GTFE, and the data output from each side is searched to ensure it contains a signal for all the expected strips and no other. Presence of noisy/dead channels can influence the result of this test.

8.6 Gain and Noise

Gain and noise for each FE channel are measured to ensure that they lie within acceptable limits, similarly to what was done in Sect. 7.19. The internal calibration system is used to inject a (rather high) fixed charge into each channel and a scan over the threshold level is performed; for each step channel occupancy is measured.

Malfunctioning channels are identified checking the measured gain to verify that it lies within the constraints. Disconnected/dead channels are those for which the measured noise is smaller than a set limit. The constraints must be properly set to discriminate

efficiently good and bad channels and therefore are chosen differently for MCMs and trays, given the different input capacitance in the two cases.

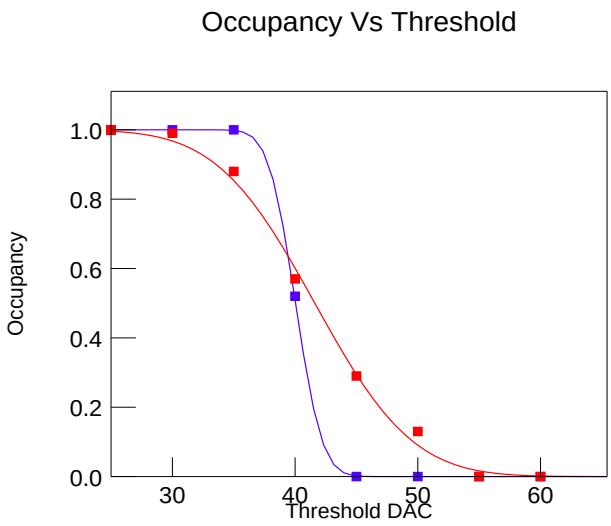

Fig. 8.3 - Occupancy versus threshold for a channel connected to the SSD and for a disconnected channel, fitted with Eq. 7.19.5. Notice how the disconnected channel shows a much sharper transition between 100% and 0%.

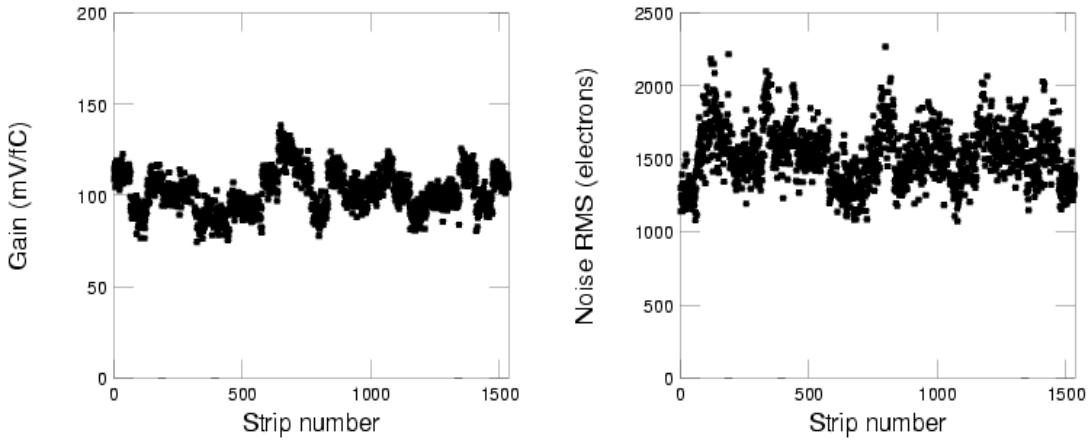

Fig. 8.4 - Gain and noise for all 1536 channels in a TKR layer.

8.7 Noisy Channels

The easiest way to spot noisy channels is to set the threshold to a low value, and read the channel occupancy in an asynchronous way, i.e. sending random triggers via software control. Noisy channels must be masked, as the channel readout is completely digital and the first level trigger, L1T, is obtained starting from the logical OR of all the channels in a silicon layer.

Again, the limiting values for the acceptance for a MCM and for a tray differ: for the latter the limits are higher to keep into account the noise contribution from the additional capacitance at the preamplifier given by the silicon sensors.

8.8 Time over Threshold

The check of the TOT is not intended for a calibration of the single channels, but rather for a check of the linearity and gain in charge measurement.

Using the internal charge injection circuit a set charge is sent into the amplifier, and the corresponding TOT is measured. A plot of TOT versus injected charge can be seen in Fig. 8.5: as the injected charge increases the TOT shows a linear trend up to a saturation value: the slope of the linear region gives the gain (in units of μs/fC), while the intercept depends on the chosen threshold. Gain and saturation point are checked to ensure they fall within the allowed range.

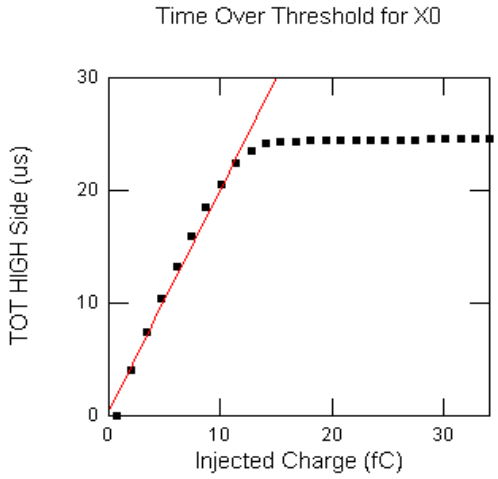

Fig. 8.5 - TOT versus injected charge for a GTFE: the slope of linear fit gives the gain.

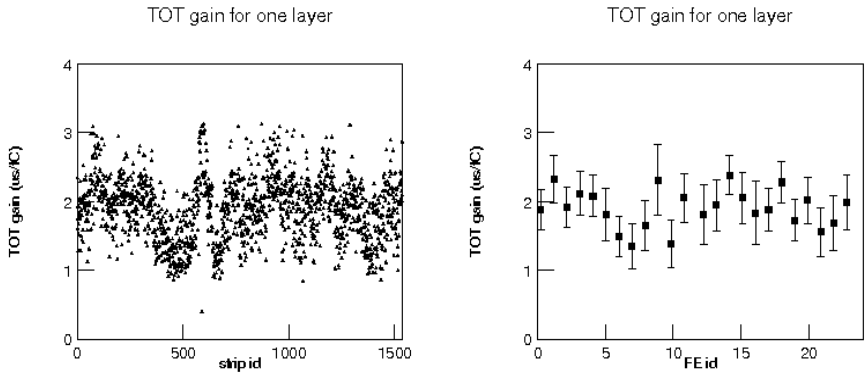

Fig. 8.6 - TOT gain for all 1536 channels in a TKR layer, and average values for the 24 GTFEs.

8.9 Data taking: the stack configuration

When completed trays are checked, it becomes possible to perform a "real" data acquisition, for example with cosmic rays, with all bad channels masked and taking advantage of the self-triggering capabilities.

In principle, this test should reproduce exactly the behavior of the final tower, and should immediately precede the final assembly. A major problem is given by the handling

requirements of the flight trays: they are enclosed in a ESD-safe box, fluxed with nitrogen, with only short connector-saver cables coming out to allow mating the MCMs with the flex cables.

This means that it is not possible to stack directly the trays one on top of each other in the tower configuration and still connect them to the flight cables. Instead of requiring new flex cables with greater length and spacing, tests are performed in the so-called *stack configuration*: a special crate holds the trays in their boxes, with the Y (or X) trays placed on top planes and the X (or Y) trays on the bottom, while the TEM and the PSA are placed in the middle. The trays below the TEM must be placed upside down to avoid having to cross the flex cables.

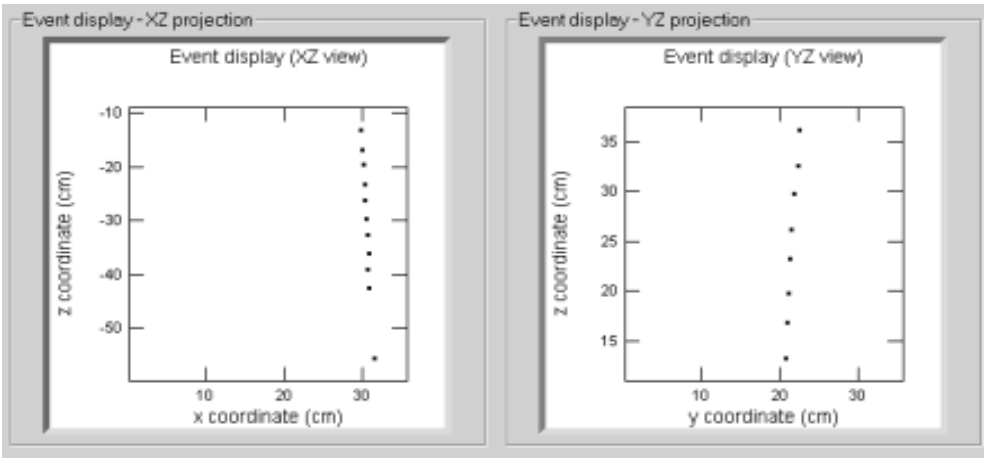

Fig. 8.7 - A cosmic ray event taken trays in the stack configuration.

Usually only a subset of layers are present; to ensure a correct functioning of the *three-in-a-row* trigger, the trigger engine must be manually tweaked setting some planes to be always on. As an example consider the data shown in Fig. 8.7: trays were connected to the TEM in consecutive Y slots on top, and to ensure a correct triggering all X planes were forced to *always ON* in the trigger engine. Similarly, other trays were connected to the TEM in X slots on the bottom, and Y planes were forced on.

8.10 Summary of I&T activities

Acceptance tests and measurements of the performances of TKR electronics were carried out in the Pisa INFN laboratories with flight parts ready for the final assembly. With a first set of trays arranged as a telescope the first events ever were observed using self-triggered flight parts.

The first tower is being assembled and tested in these days in the INFN clean room, and the expertise matured in the activities described here will soon be put forth in the final stages of the LAT integration: putting the towers together and testing the Large Area Telescope itself.

9 Simulation of LAT performances

In this chapter a brief introduction to the simulation of LAT response and to data analysis techniques is given. Requirements on the LAT performances and the validation of the telescope design were carried out with a specific software package. Now a novel software architecture is under development, with major changes with respect to the past tools, and the need arises of validating the results obtained with it.

Software activities carried on in Padova are detailed: efforts focused on the validation of the backbone of the new Monte Carlo simulation package, i.e. the model describing the physical interactions, and on the developement of background rejection techniques, in collaboration with the INFN sections of Trieste and Udine.

9.1 Simulating the LAT performances

Simulated events are of great importance in checking and/or correcting for non-trivial or unforeseen detector or physics effects, as well as comparing detector performance with expectations and ensuring science requirements are met. The LAT design itself is based on detailed Monte Carlo simulations performed in the early stages of the GLAST collaboration. This early LAT simulation has been used to:

- demonstrate a cosmic-ray rejection better than $10^5 : 1$ with high γ-ray efficiency;
- obtain a solid understanding of LAT performance after all triggers and cosmic ray rejection cuts;
- develop reconstruction algorithms and a practical scheme for triggering;
- determine the requirements on the LAT design.

Simulation allows to predict the telescope figures of merit, depending on the incoming photon energy E_γ and angle θ. The influence of the detector design can be assessed, and hardware requirements can be loosened or made stricter when necessary.

The geometric area of a telescope is not the area that must be used to calculate the physical properties of sources in the sky such as flux and surface brightness. The *effective area* (Aeff) depends on geometric area, but also on the conversion probability and reconstruction efficiency. The effective area has units of cm^2: it is the product of geometric area and efficiency (including any filters), which depends on the primary energy and position on the detector.

The *Point Spread Function* (PSF) describes the shape of the image produced by a delta function, i.e. a point source, on the detector. Taking into account the LAT design one can derive the contribution to the intrinsic limitations on the resolution as $\sigma_{ms} = 1.5 \times (1\ \mathrm{GeV})/cp$ mrad due to multiple scattering in a converter plane, $\sigma_p = 2$ mrad due to the silicon strip pitch, and a contribution that depends on the effectiveness of the tracking algorithm [112]. The telescope overall resolution is usually described in terms of the PSF 2-dimensional 68% containment: it is the equivalent of $\sim 1.5\sigma$ (1-dimensional error) for a purely Gaussian response. The non-Gaussian tails are characterized by the 95% containment, which would be 1.6 times the 68% containment for a perfect Gaussian response; the 95%/68% ratio is therefore often quoted.

Parameter	SRD Value
Peak effective area (in range 1-10 GeV)	>8000 cm^2
Energy resolution 100 MeV γ on-axis	10%
Energy resolution 10 GeV γ on-axis	<10%
Energy resolution 10-300 GeV γ on-axis	<20%
Energy resolution 10-300 GeV γ 60°	<6%
PSF 68% 100 MeV γ on-axis	<3.5 deg
PSF 68% 10 GeV γ on-axis	<0.15 deg
PSF 95/68 ratio	<3
PSF 55°/normal ratio	<1.7
Field of View	>2 sr
Background rejection	10^5:1

Tab. 9.1 - Science requirements on LAT performances [1].

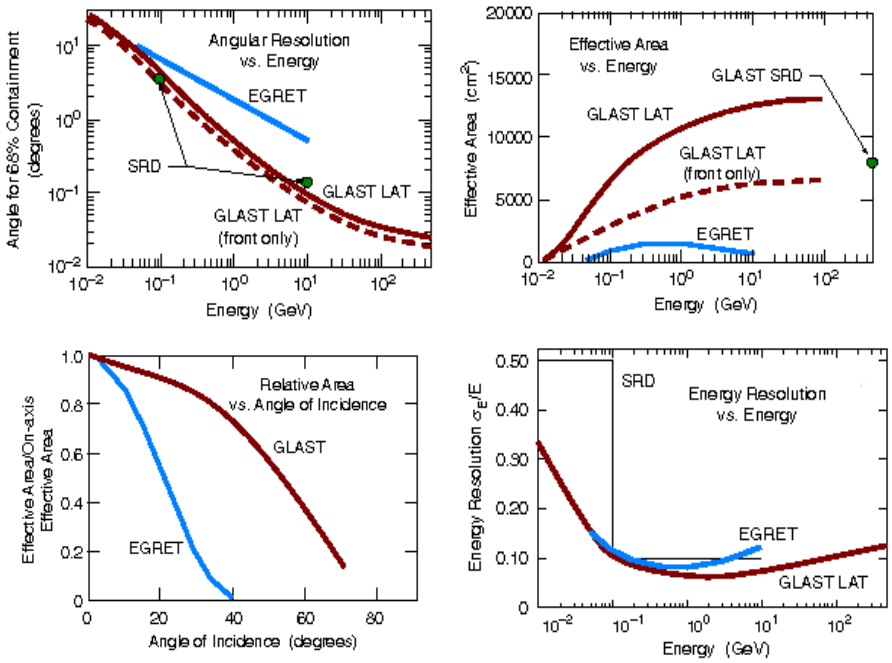

Fig. 9.1 - Preliminary simulations of LAT figures of merit, from [39]; science requirements are shown and EGRET parameters are given as a comparison.

Energy resolution depends strongly on the reconstruction algorithms. Severe complications arise because of the limited mass of the calorimeter; moreover, the highly modular structure of the LAT implies the presence of several gaps (e.g. between towers) that must be kept into account. For low energy γ (below a few hundreds MeV) the biggest correction is given by the energy loss in the tracker converter planes. At higher energies a big part of the EM shower energy leaks out the CAL bottom: if the shower maximum is contained (below $\sim$ 50–100 GeV) the missing energy can be obtained rather easily, being proportional to the energy deposited in the last layer (*last-layer correlation*), else the shower profile must be fitted. The shower transverse developement, function of the Moliere radius, must be calculated to correct for energy losses along edges.

The LAT simulation developed during the instrument design used the GISMO toolkit [113], which incorporates the EGS4 package [114] for electromagnetic particle interactions and the GHEISHA package [115] for hadronic interactions. All mechanical structure, electronics material within the detection volume, the material inherent in the detector elements themselves, detector inefficiencies, cracks and gaps were included in the model. Because γ rays are produced as byproducts of cosmic ray interactions, an approximate description of the spacecraft, solar panels, and the thermal blanket surrounding the LAT was included. After the particle simulation each detector subsystem generated a response that took into account the properties of the real device (including noise, inefficiencies, etc.). The TKR reconstruction was initially done in separate x and y projections. A Kalman filter algorithm [116] was used to fit tracks and generate test statistics while taking multiple scattering into account.

Assuming an average trigger rate in orbit of $\sim$ 5 kHz, a rejecting power of $10^5 : 1$ is necessary being for the scientific objectives to be fulfilled. A factor 100 can be implemented on-board (it is necessary given the limitations on the data downlink): this means that at least another factor 100 is required from ground analysis. The early LAT simulation allowed to demonstrate the possibility of meeting such strict requirements on the background rejection efficiency.

9.2 The new LAT simulation: GLEAM

The primary goals of the reconstruction program described in Sect. 9.1 have been to validate the design and to provide guidance in its optimization. LAT simulation continued to improve substantially and became more sophisticated, leading to further improvements in the LAT performance parameters. Modern software-engineering methods are used in the software design to allow to carry algorithms developed for the reconstruction of simulated data forward into real data analysis tasks such as beam tests, the balloon flight, and finally the flight phase of the mission.

To accomplish these tasks an object-oriented C++ framework called *Gleam* (GLAST LAT Event Analysis Machine) was developed by the GLAST LAT collaboration. A brief description of the framework can be found in [117]. An overall C++ framework manages the particles to be simulated, then a series of algorithms are applied to each of them to get the result of the complete simulation and reconstruction chain.

The structure of the GLAST off-line software is described in Fig. 9.1. An important characteristics is the separation of the packages according to their responsibilities. Most packages has been developed explicitely by the GLAST collaboration for the specific items. *Source generation* is the first algorithm called within the particle loop. Its task is to generate particles according to certain characteristcs. This algorithm must store the information on the temporal and spectral behaviour of the source, as well as on the orbital characteristics of GLAST. A series of default sources are implemented, including source for testing purposes, astrophysical objects and the expected particle and albedo gamma backgrounds. The information generated in this package is put in a transient data store, so that every other piece of code in the framework can use it.

The algorithm which is responsible for generating the interactions of particles with the detector is now based on the GEANT4 MonteCarlo toolkit [118] which is an Object Oriented simulator of the passage of particles through matter. GEANT4 (G4) provides

a complete set of tools for all the domains of detector simulation: geometry, tracking, detector response, run, event and track management, visualization and user interface. A large set of physics processes handle the diverse interactions across a wide energy range, as required by G4 multi-disciplinary nature; for many physics processes a choice of different models is available. Within the Gleam framework the simulation is managed by the *G4Generator* algorithm. The main simulation is controlled by a customized version of the G4 standard `RunManager`.

To implement a detailed *Digitization* of the TKR system a full simulation code has been developed. It takes into account all the main physical processes that take place in a SSD when it is crossed by an ionizing particle [119]. The present version of the code has been written in C++ and the process of energy loss is simulated by GEANT4. The input parameters of the code are the entry and exit points of the particle in a silicon ladder and the energy deposited by the particle, provided by the simulation package. Starting from these parameters, the e-h pairs are generated along the track and are propagated towards the electrodes. The current signals induced on each strip are evaluated and are converted into voltage signals using the transfer function associated to the detector electronics, taking into account the detector noise as well as the noise associated to the electronics. The strips registering a signal over threshold and the TOT are then determined. Simplified version for the signal digitization are provided for the CAL crystals and the ACD panels.

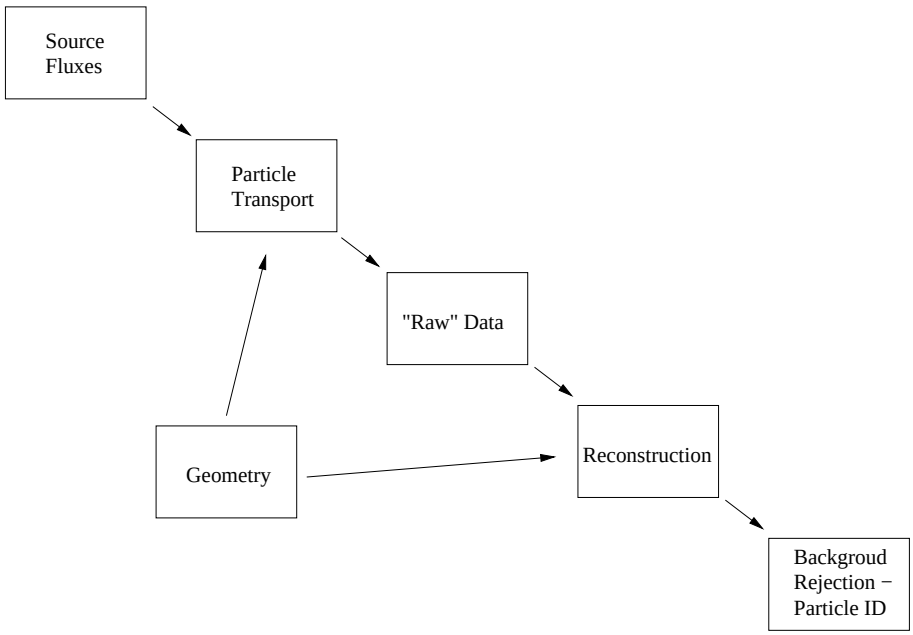

Fig. 9.2 - General scheme for simulation and reconstruction within the GLAST off-line software framework.

The *Reconstruction* package contains the code that reconstructs tracks from hit strips in the LAT tracker. It is organized as a series of algorithms that act successively.

It starts by grouping the hits (silicon strips that registered a passing charged particle) in the TKR into clusters, because adjacent strips can register the passage of the same particle. A pattern recognition algorithm is then applied to associate the clusters into 'tracks', with preference for finding the longest, straightest tracks. The candidate tracks are then fitted via Kalman filtering: this defines the best estimate of the initial direction

of the charged particle. The energy information from the CAL is used to evaluate the scattering angles expected in each tracker plane. Reconstructed tracks are analyzed to define the conversion point of the gamma ray and its initial direction; at higher energies, the positron and electron tracks may not separate at the resolution of the tracker, so the vertex and the estimated initial direction come from analysis of a single track.

The energy deposition in the CAL in general must be corrected to account for partial containment of the showers. The CAL being only 8.5 X_0 thick, even at moderately large inclination angles significant corrections are required, by means of shower profiling and last-layer correlation. The development of the showers in the CAL can be reconstructed (with coarse resolution) owing to the hodoscopic design discussed in Sect. 3.3. Intrinsic fluctuations in energy deposition as showers develop limit the resolution achievable by these techniques.

Finally, the estimated energies and initial directions of the two tracks are used to calculate the energy and direction of the incident γ ray. Other algorithms, applied after the full event reconstruction, take care of production cuts, persistency and preliminary analysis. In particular, the *merit* algorithm creates an output ROOT file that contains variables that allow event analysis without bothering with the full informations about the instrument response. As an example the single strips that fired are not saved, whereas reconstructed tracks and vertexes are. Informations on the primary particle, variables detailing the response of TKR, CAL and ACD, trigger words, etc. are stored.

9.3 Validating the G4 simulation

The correct assesment of LAT resolution, sensitivity and background levels assumes a correct simulation of the interactions between energetic particles and matter. Problems in this sense may derive from the customization required to include a G4 propagation engine into the Gleam framework (see Sect. 9.1) as well as from bugs in the G4 distributions, in the Gleam code, etc. Moreover, G4 has been mainly used by high-energy physicist, and from this point of view the energy range of GLAST is relatively low. Though in the last years the G4 community put forth a huge effort in extending the validity of G4 towards lower energies, the GLAST collaboration felt the need of an independent validation tool. Similar considerations can be applied tio the simulation of hadronic interactions. Validation must be performed each time a new release of the LAT simulation package is released, before making it avalilable to users.

Previous activities in thies field resulted in *GEANT4TEST*, a software package by F. Longo, R. Giannitrapani and T. Burnett. Based on the same approach the *slab* code [120] was developed in Padova, where a cylindrical slab of a set material is placed perpendicular to a pencil beam of selected particles. Secondary particles, their energies and trajectories are scored and saved into a `ROOT` file. Analysis is performed with a set of ROOT macros provided with the *slab* code. A particular effort is taken to compare simulated results both with theoretical models and with experimental data.

As an example in Fig. 9.3 the radial developement of an EM shower is shown. 1 GeV electrons hit axially an aluminum cylinder and the deposited energy is plotted as a function of depth z and radius r; the last point at higher r values is the integral of the energy released beyond that point. Many more examples can be found in [120].

The future validation package must include tests for all EM interactions (pair pro-

duction, compton, photoelectric, bremsstrahlung, MCS, ionisation and δ-ray production, positron annihilation, ...). Tests of relevant hadronic processes must be developed and checked; an example is shown in Fig. 9.4. Currently a new version of the *GEANT4TEST* package is being developed, implementing the `event` structure defined by the experience with the *slab* code, and the macro package defining the tests is undergoing a minor review to fit within this new environment.

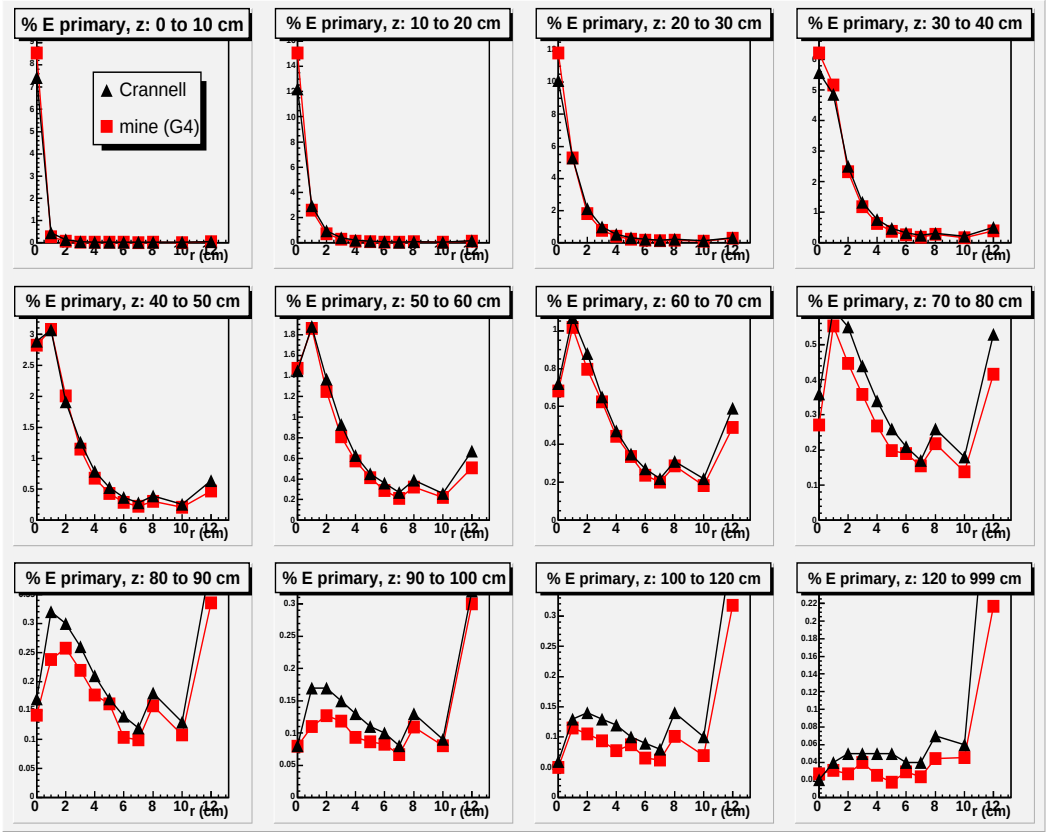

Fig. 9.3 - EM processes: radial EM shower profile, 1 GeV electron in Al; experimental data from [121] (triangles) and G4 simulation (squares); last point is the residual up to $r{=}{+}\infty$.

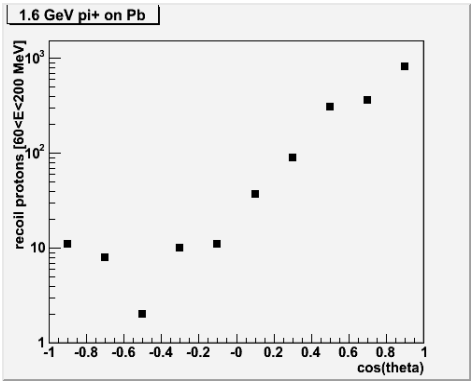

Fig. 9.4 - Hadronic processes: angular distribution of recoil protons from 1.6 GeV pions on Pb.

9.4 Particle ID and background rejection

The production of a "clean" gamma-ray data set is vital. Before downlink a background rejection of a factor ~ 100 should be obtained onboard, after L3T and the *onboard filter*. The first task once the events are transmitted and stored on Earth is to discriminate between γ events and background hits before producing the data file for the off-line (science) analysis: another factor ~ 100 is required. This requirement was met by the earlier software tools, and it is being investigated if this result, repeated with the new software environment, can be improved.

Several paths can be followed to correctly identify signal and noise events from the event variables. It must kept in mind that besides the great rejecting power, the selected procedure must not uncorrectly identify too many signal events as noise, thus reducing the detector sensitivity and effective area. The most traditional way uses a series of *cuts* to find a section in the event parameter space where signal hits are much more abundant that noise hits. As an example look at the `CalCsIRLn` variable plot in Fig. 9.5: it defines the number of radiation lengths between the first hit in the TKR and the energy centroid in the CAL. Simulated events are shown, for which a medium[(1)] energy deposition in the calorimeter was registered. "Good" events correspond to those events for which the *Reconstruction* algorithm has performed a correct estimate of the primary energy (notice that in simulated data we have also all the informations from the Monte Carlo regarding the primary particle). Events above ~ 5 can be safely considered as good, while events below ~ 2 can be regarded as bad. Events in between are not discriminated enough and additional cuts performed on other variables must be investigated.

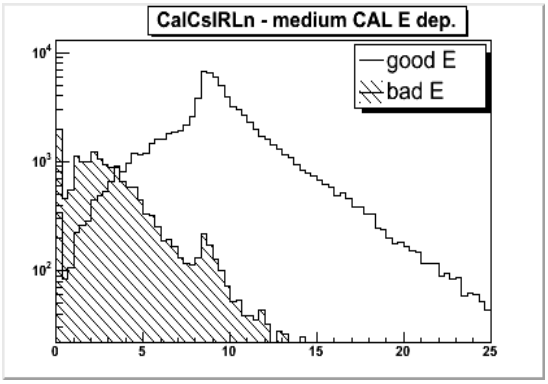

Fig. 9.5 - A highly discriminating variable: radiation lengths from the first hit in TKR and the centroid of energy deposition in CAL.

Currently, the classification of events is implemented using trees [122] trained with simulated data. Trees are obtained by a divide-and-conquer algorithm that recursively partitions the training data set into smaller subsets depending on one variable and its values. An example of a classification tree and its growth is shown in Fig. 9.6: the variable "goodness" is expressed in terms of the remaining parameters, x and y. If the dependent variable is continuous one obtains a *regression tree*; otherwise, if it is discrete one obtains a categorical predictor, a *classification tree* (CT).

(1) – here defined as 350 MeV $<$ Edep $<$ 3.5 GeV.

Once the tree is grown from a training data set, it can be used to predict the modelled variable using the others. Usually the tree is grown from simulated data, where all "hidden" variables are available, and then applied on experimental data. Each event "falls" inside the tree root from above, following its course depending on the values of its many variables, until it reaches a final node: the value corresponding to that "exit" is the predicted variable.

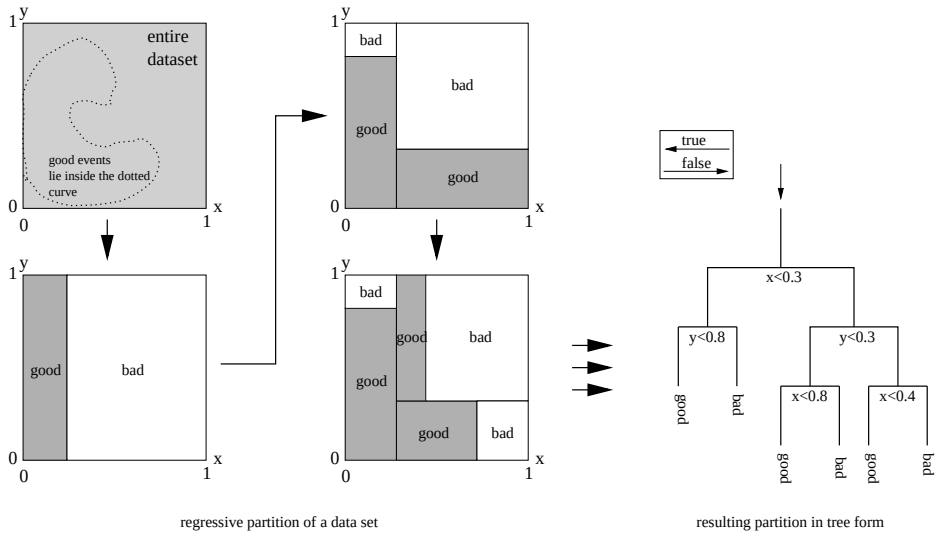

Fig. 9.6 - Example of a classification tree where each event is described by three variables, x, y and "goodness"; events are classified in terms of the latter.

In principle the tree would branch until it models completely the data set it is grown on: with enough splits each events in the data set would have its own end node. The growth of a branch can be terminated when the significance of a split falls below a set value, or when the fraction of the events reaching it is too small. Nonetheless, since the tree is grown from a training data set, when it has reached full structure it usually suffers from over-fitting (i.e. it is "explaining" random correlations in the training data that are not likely to be features of the larger population it will be applied on). This results in poor performance on real life data. Therefore, it has to be *pruned*: once the growth stops and a tree is returned from the partitioning algorithm, some branches are deleted beacuse they fail some user-defined test. Several pruning strategies exist, e.g. *k-fold cross-validation*, *bootstrapping*,... As an example, in k-fold cross-validation data are divided into k subsets of (approximately) equal size. The tree is trained k times, each time leaving out one of the subsets, but using only the omitted subset to compute some sort of error criterion. When bootstrapping, instead of repeatedly analyzing subsets of the data, one repeatedly analizes randomly chosed data subsamples.

In the current implementation, event classification is performed this way:

i) determine if energy is well measured (important for track fit)
ii) choose vertex or single track gamma direction estimate
iii) assess probability that an event is in the PSF core distribution
iv) predict the PSF itself
v) assess probability that an event is really a gamma ray (vs. background)

All steps involve either classification or regression trees. Currently trees are produced with a commercial application for statistical analysis, exported in XML files and loaded in the C++ framework through a conversion package. We are now working on alternative tools and methods, trying to improve the performance of the background rejection algorithm.

9.5 Developing a classification: an example

As an example of the work currently in progress (and of the construction of a predictive tree) we include here a possible implementation of step i, as seen in the last section.

Following the current procedure we define that energy reconstruction is succesfull if:

$$\left|\frac{\texttt{EvtEnergySumOpt} - \texttt{McEnergy}}{\texttt{McEnergy}}\right| < 35\% \tag{9.5.1}$$

where `EvtEnergySumOpt` is the fully reconstructed energy and `McEnergy` is the energy of the primary particle in the simulation.

First, a training dataset is created, writing 200,000 simulated events into a text file as a comma-separated variable list; the variables in the `merit` ntuple pertaining to CAL, TKR, ACD, trigger and reconstructed primary are saved. An additional boolean variable is saved, i.e. the goodness of the CAL energy reconstruction as defined in Eq. 9.4.1.

To improve the algorithm discriminating capabilities, currently events are divided in four bins corresponding to the energy released in the calorimeter; we will now detail the procedure to classify the events with a medium deposition (350 MeV $<$ E $<$ 3.5 GeV). Of the initial 200,000 events, 76,456 are associated with the energy deposition mentioned above. Of these, 29,387 pass the first simple vetoing procedures and are used for this analysis.

Now a classification tree must be grown on these data. We use `R` [123] [124], a freeware environment for statistical computing. Recursive partitioning is possible with the help of the `rpart` package (from the original S-plus version [125]).

A tree is grown, keeping the stopping parameters as loose as possible; the overfitting problem will be solved through a process of post-pruning of the obtained tree. The first resulting trees are shown in Fig. 9.7: each step implies an increase in the number of branches, while the predictive value of the tree increases, as shown by the decreasing stochastical error in the fourth column.

The problem of the tree overfitting the training event set still has to be solved. To do so the cross-validation method is employed: in column 5 an error estimate is obtained through a process of 10-fold cross-validation. It decreases down to a value of 0.550, to increase again after that. One could take the tree corresponding to the minimum $\times$-error, but the cross-validation technique suffers from a fundamental uncertainty: it randomly selects the subsets used in the tests, so repeating the process with a different seed for the random engine would produce (slightly) different results. To solve this the minimum $\times$-error is chosen, its standard deviation is added and the smallest tree whose $\times$-error is smaller than this figure is selected. In our case the minimum error is 0.550 ± 0.010, hence the tree number 5 is selected, as its $\times$-error is 0.559, smaller than $0.560 = (0.550 + 0.010)$.

Root node error: 4630/29387 = 0.15755

n= 29387

step	CP	nsplit	rel error	xerror	xstd
1	0.35507559	0	1.00000	1.00000	0.013489
2	0.03153348	1	0.64492	0.64233	0.011167
3	0.01821454	2	0.61339	0.61037	0.010916
4	0.01403888	5	0.55875	0.60065	0.010838
5	0.00269978	6	0.54471	0.55875	0.010491
6	0.00233261	14	0.52138	0.55443	0.010454
7	0.00183585	21	0.50281	0.55767	0.010482
8	0.00172786	23	0.49914	0.55248	0.010437
9	0.00165587	26	0.49395	0.55248	0.010437
10	0.00161987	29	0.48898	0.55011	0.010417
11	0.00151188	31	0.48575	0.55011	0.010417
12	0.00129590	38	0.47473	0.55464	0.010456
13	0.00115191	39	0.47343	0.55140	0.010428
14	0.00107991	48	0.46263	0.55270	0.010439
15	0.00100792	55	0.45508	0.55400	0.010450
16	0.00097192	61	0.44903	0.55464	0.010456

Fig. 9.7 - Creation of a classification tree: each line details the tree growth step by step.

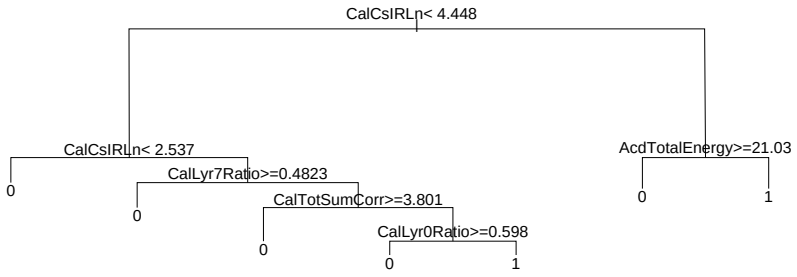

Fig. 9.8 - Pruned tree: on each split the events satisfying the requirement go to the left, ending nodes labeled with a *1* are those corresponding to a good energy reconstruction.

The resulting tree (see Fig. 9.8) is very small: all successive splits in Fig. 9.7 are considered just an overfit of our data sample. As an example of the performed partitioning, the first discrimination is performed on the basis of the `CalCsIRLn` variable: the corresponding distribution was shown in Fig. 9.5.

reconstructed E (Eq. 9.4.1)	CT thinks them good	CT thinks them bad
good (64400 evts)	**62167**	4342
bad (12056 evts)	2233	**7714**

Tab. 9.2 - Results of our classification for medium energy depositions in the CAL: figures in bold correspond to a correct classification.

To test the predicting capabilities of the tree just developed, we take another $\sim 520,000$ simulated events and divide them into those with a good energy reconstruction and those for which the reconstruction fails, using the tree we just prooduced. After the cuts on the deposited energy and the preliminary vetoes $76,456$ events are available for our analysis. The results of the analysis performed using our CT are detailed in Tab. 9.2;

events correctly classified are shown in bold. Results look promising, and are prefectly compatible with results obtained by other authors.

Currently our work focuses on extending the approach above to all energy regimes and to implement all other classifications discussed in Sect. 9.3. The possibility of extending the variable set used to grow the trees is being evaluated.

10 Conclusions

The tracker electronics for the GLAST LAT telescope have been tested in Padova for total-dose and single-event effects, to evaluate the radiation hardness required for satellite-borne operations. No problems are foreseen due to radiation-induced damage for the expected 5-year mission. No destructive failures are expected, while the slow degradation in the performances due to the dose the ASICs will receive from solar and galactic energetic particles remains negligible. Given the success of the TKR validation program, DAQ electronics and COTS components were tested too, with similar results.

LAT flight parts have been tested and their performances verified, and a first tower assembly with certified flight components has been assembled in Pisa. The first cosmic ray events were observed.

As the completion of the LAT approaches, ever increasing attention is being given to the simulation and analysis of LAT data. Validation of some of the physics tools included in the LAT simulation package is carried out in Padova, together with a fine-tuning of the background rejection routines.

Appendix 1: Electromagnetic processes

In this appendix processes giving rise to energetic photons and the spectral signatures observable in astrophysical sources are introduced. Interactions of photons with matter are described: pair production is particularly relevant to the LAT tracker operation, while the development of electromagnetic showers in a medium heavily affects the performances of the LAT calorimeter.

A1.1 Thermal emission

Thermal radiation emanates from a large population of electromagnetic particles (typically electrons) interacting among themselves. At equilibrium the interactions between radiation and matter are so intense that the respective energy densities are bound to be identical.

The spectrum of emitted radiation follows the well-known *black-body* distribution:

$$I(\nu) = \frac{8\pi h\nu^3}{c^3} \frac{1}{e^{h\nu/kT} - 1} \qquad (A1.1)$$

The temperature of the emitting source and the peak wavelength of this distribution are linked by the *Wien law*

$$\lambda_{\max} T \approx 0.29 \text{ cm} \cdot K \qquad (A1.2)$$

for a black-body thermally emitting γ rays peaked around 10 MeV the surface temperature is about 2×10^{10} K.

A1.2 Synchrotron and bremsstrahlung radiation

Both synchrotron and bremsstrahlung radiation are emitted when a charged particle accelerates, thus radiating EM waves. Given the similar origin, EM radiation produced by these two processes share some features:

- emitted power is proportional to the square of the charge and the square of the acceleration;
- photons are emitted in a characteristic dipolar form: there is no emission along the acceleration vector and maximum emission is perpendicular to the acceleration vector;
- emitted radiation is polarized: the electric field vector is parallel to the acceleration vector.

Synchrotron radiation is produced by relativistic particles moving in a magnetic field. More precisely it is the relativistic equivalent of cyclotron radiation, the crucial distinction being time dilation and Doppler beaming effects, due to the large Lorentz factor of the particles involved.

Synchrotron radiation is mostly important in the case of electrons, as they are lighter and thus more easily deviated. Due to the magnetic field B the trajectories of electrons are gyrations of frequency

$$\nu_{\text{gyr}} = \frac{eB}{2\pi\gamma m_e c} \qquad (A1.3)$$

Appendix A1

The acceleration the electron experiments causes the emission of photons peaked at a frequency

$$\nu_S = \frac{3}{2}\gamma^2 \nu_{\rm gyr} \sin(\theta) \qquad (A1.4)$$

where θ is the angle between the particle momentum and the field lines. As the electron gyrates around the field lines, the emitted radiation reaches the observer only when the photon beam is aligned with the line-of-view. Due to this the synchrotron spectrum is a sum of a large number of harmonics of the base cyclotron emission. The summed spectrum is sharply peaked, with maximum emission at $\approx 0.29 \cdot \nu_S$ and with intensity

$$I(\nu) \propto \left(\frac{\nu}{\nu_c}\right)^{\frac{1}{3}} \qquad \text{for } \nu \ll \nu_c \qquad (10.0.1.a)$$

$$I(\nu) \propto \left(\frac{\nu}{\nu_c}\right)^{\frac{1}{2}} e^{-(\nu/\nu_c)} \qquad \text{for } \nu \gg \nu_c \qquad (10.0.1.b)$$

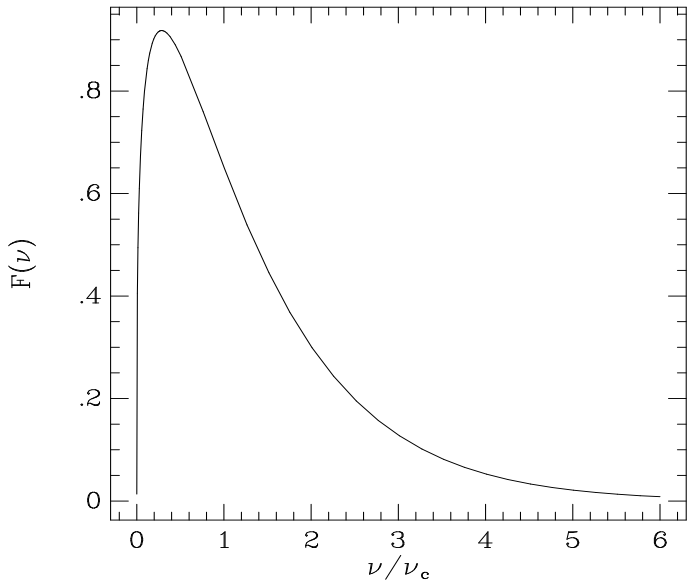

Fig. A1.1 - Synchrotron spectrum, peaked at the characteristic frequency corresponding to $0.29\ \nu_S$.

Energetic electrons or extremely intense magnetic fields can shift this peak energy in the γ range. Candidates for this phenomenon are therefore electrons moving near the surface of neutrons stars, where B can be of the order of 10^{10} G or more. As an estimate, an electron with energy E_e in the presence of a field B would radiate photons of energy

$$E_\gamma \approx 0.05 \left(\frac{E_e}{(\text{TeV})}\right)^2 \left(\frac{B}{(3\mu\text{G})}\right) \qquad eV \qquad (A1.5)$$

In presence of magnetic fields above $\approx 10^{13}$ G relativistic and quantum effects result in a more complex scenario. The magnetic field is so intense that it constrains the particles to move along the field lines. In this case radiation is emitted when the field lines curve: this process is called *magneto-bremsstrahlung* or *synchro-curvature radiation*.

Bremsstrahlung radiation is emitted when a charged particle passes close to an atomic nucleus, experiencing an acceleration which in turn causes the emission of photons. Given that the cross section depends inversely on the square of the particle mass, bremsstrahlung is extremely efficient for light particles, like electrons.

Integrating the bremsstrahlung cross section we have the expression of the total intensity as a function of the photon frequency, of the electron velocity v and of the impact parameter b; we find

$$I(\nu) = \frac{(Ze)^2 e^4 n}{12\pi^3 \varepsilon_0^3 c^3 m_e^2 v_e} \ln\left(\frac{192 v_e}{Z^{1/3} c}\right) \qquad \mathrm{J/cm^2} \tag{A1.6}$$

where n is the atom density in the medium the particle traverses.

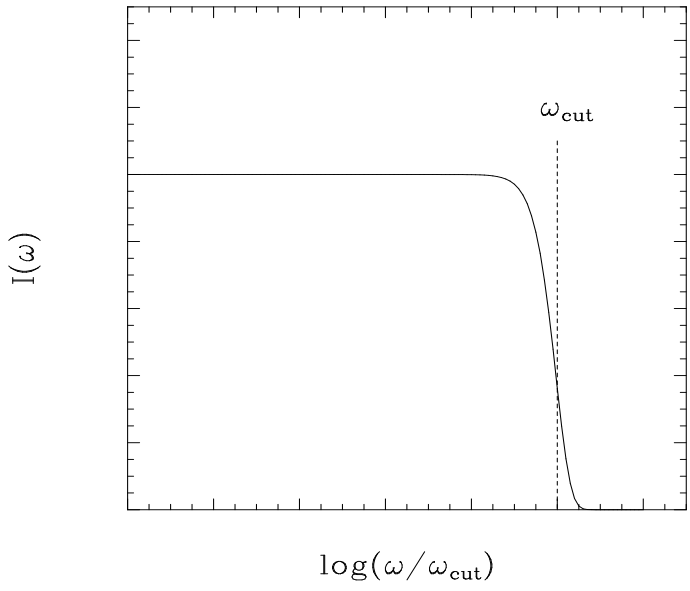

Fig. A1.2 - Typical Bremsstrahlung spectrum.

The spectrum of bremsstrahlung radiation remains flat up to roughly the electron kinetic energy

$$E_k = (\gamma - 1) m_e c^2 \tag{A1.7}$$

when it drops sharply to zero, as all the available kinetic energy of the electron has been transferred to the photon.

At a high energy E, due to relativistic beaming the mean angle of emission is

$$\theta_\gamma = \frac{mc^2}{E} \tag{A1.8}$$

thus, most of the electron energy is released in a narrow cone around the electron momentum vector.

The description above supposes a single electron interacting with a sea of atomic nuclei. In the case of a hot electron-proton plasma, the total emission by all particles is called *thermal bremsstrahlung*. Let T be the plasma temperature, n_e and n_p the densities of electrons and protons respectively; in this case the spectral emissivity per unit volume and time is

$$k_\nu = \frac{1}{3\pi^2}\left(\frac{\pi}{6}\right)^2 \frac{(Ze)^2 e^4}{\varepsilon_0^3 c^3 m_e^2}\sqrt{\frac{m_e}{kT}}\, g(\nu,T) n_p n_e \exp\left(-\frac{h\nu}{kT}\right) \qquad \text{W m}^{-3}\ \text{Hz}^{-1} \qquad (A1.9)$$

where $g(\nu,T)$, the *Gaunt factor*, depends on details of the collision process and on the used approximations, and can be approximated in the γ-ray regime by $(E_\gamma/kT)^{1/2}$.

A1.3 Inverse Compton

In "normal" Compton scattering a photon collides with a (quasi-)free electron and transfers to it a part if its energy. In *inverse Compton scattering* the inverse process happens: a photon interacts with an energetic electron and gains energy in the collision. This process is important in regions with a high density of photons and with the presence of "hot" electrons.

The spectral emissivity of the plasma in the case of isotropic photons of frequency ν_0 and density $N(\nu_0)$ is

$$I_\nu(\nu_0) = \frac{3\sigma_T c}{16\gamma^4}\frac{N(\nu_0)}{\nu_0^2}\nu\left[2\nu\cdot\ln\left(\frac{\nu}{4\gamma^2\nu_0}\right) + \nu + 4\gamma^2\nu_0 - \frac{\nu^2}{2\gamma^2\nu_0}\right] \qquad (A1.10)$$

where σ_T is the Thomson scattering cross section. The typical energy of up-scattered photons rises rapidly with energy:

$$E_\gamma \approx 1.3\left(\frac{E_e}{(\text{TeV})}\right)^2\left(\frac{E_{\gamma,0}}{2\times10^{-4}(\text{eV})}\right) \qquad \text{GeV} \qquad (A1.11)$$

where $E_{\gamma,0}$ is the typical energy of the original photons.

A1.4 Nuclear Transition

As for any other quantum system, the atomic nucleus has specific, quantized energy levels given by the strong force binding the nucleons. These nuclear states have a spacing of the typical order of $\approx$ MeV. Thus, a transition between two nuclear states can release a photon in this range of energies.

Processes leading to nuclear line emissions are, for example, collision between cosmic rays and nuclei of the interstellar gas, or radioactive decays of a freshly synthesized nucleus. The typical ($\beta+$) decay can be expressed as

$$^nX \longrightarrow^{n-1} Y^* + e^+ \longrightarrow^{n-1} Y + \gamma \qquad (A1.12)$$

Some characteristic energy levels, important for γ astronomy, are 4.438 MeV($^{12}C^*$), 6.129 MeV($^{16}O^*$) and 1.809 MeV($^{26}Mg^*$).

A1.5 Decays and Annihilation

Neutral pions, created by strong interactions, decay rapidly into two photons, with an energy distribution peaking at ~ 70 MeV, half the rest mass of the pion. The pion decay bump is then broadened by Doppler shift; for beamed emission (e.g. in jets) the peak is instead Doppler shifted.

Annihilation of particles and antiparticles converts energy into two (or more) photons, emitted back to back and sharing the converted energy, at least in the annihilation rest frame. The most abundant process in astrophysical searches is the electron-antielectron annihilation, but with a released energy of only 511 keV per photon.

A1.6 Photon absorption

The *photoelectric effect* corresponds to the capture of a photon by an atom, followed by the emission of one of its electrons with kinetic energy $E_{k,e} = h\nu - W$, where W is the electron binding energy. The photoelectric cross section falls roughly as

$$\sigma_{\rm ph} \propto Z^5/\nu \qquad (A1.13)$$

and this process is relevant only for photons with less than ≈ 1 MeV.

The *Compton effect* involves the scattering of an electron by an incident photon; the scattered photon has a lower energy and longer wavelength. The angular distribution of the emitted photons is $I \propto (1 + \cos^2\theta)$ at lower energies, while at higher momenta the photons are more beamed. The Compton effect is relevant at best in the range 0.1 – 10 MeV, and the corresponding cross section falls, at high energies, like

$$\sigma_{\rm comp} \propto Z/\nu \qquad (A1.14)$$

The *pair production* mechanism causes the conversion of the incoming photon into a electron-positron pair in the electric field of an atom (required to conserve momentum). The threshold energy for this process is clearly $2m_ec^2$ and therefore the process is relevant for photon energies above a few MeV; the mean production angle of electron (or positron) with energy E is $\theta \sim mc^2/E$. The pair production cross section saturates at energies above some tens of MeV, where it is the dominant interaction mechanism, and in this regime the cross sections is approximately proportional to Z^2 and independent of the frequency:

$$\sigma_{\rm pp} \propto Z^2 \qquad (A1.15)$$

The pair production mechanism is strictly connected to bremsstrahlung, and the cross-sections are similarly related, so that

$$\sigma_{\rm pp} \simeq 7/9 \cdot \sigma_{\rm brem} \qquad (A1.16)$$

A1.7 Ionization

Charged particles moving in a medium lose kinetic energy because they excite or ionize atomic electrons. This process is important especially for particles heavier than the electrons themselves. A detailed analysis of this mechanism leads to the well known *Bethe-Bloch formula* describing energy loss:

$$-\frac{dE}{dx} = \frac{n_e e^4 Z^2}{4\pi\varepsilon_0^2 m_e c^2 \beta^2}\left[\ln\left(\frac{2m_e c^2\beta^2\gamma^2}{I}\right) - \beta^2 - \frac{\delta(\gamma)}{2}\right] \qquad (A1.17)$$

where n_e is the electron density, I is the mean ionization potential and the term $\delta(\gamma)$ is a correction for the so-called density effect.

The amount of energy lost by a charged particle that has traversed a fixed thickness of material will vary due to the statistical nature of its interactions with the individual atoms: the value obtained from Eq. $A1.17$ above is an averaged value. The number of recoil electrons produced with energy greater than E_1 in a thickness x is

$$N(E \geq E_1) = \int_{E_1}^{E_{\max}} \frac{dE}{E^2} \cdot \frac{n_e Z^2 e^4}{8\pi m \beta^2 c^2} x \qquad (A1.18)$$

where $E_{\max}$ is the maximum possible energy transfer. More energetic electrons, capable of producing themselves ions in traversing the medium, are called *delta rays*.

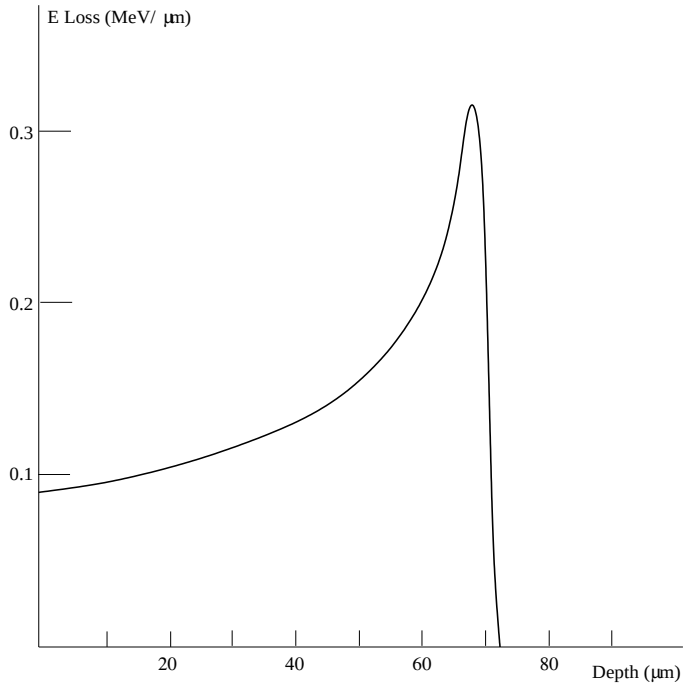

Fig. A1.3 - Energy loss versus depth in silicon for a 10 MeV alpha particle.

A1.8 Electron interactions

Electrons and positrons can lose energy by ionization just like heavier charged particles, and below 10 MeV this mechanism is dominant (see Fig. *A*1.4). At low energies other processes contribute, such as *Møller scattering* (electrons) and *Bhabha scattering* (positrons). From the corresponding cross sections one obtains the energy loss for both processes, given by

$$-\frac{dE}{dx} = \frac{n_e e^4}{8\pi m_e c^2}\left[2\ln\left(\frac{2m_e c^2}{I}\right) + 3\ln\gamma - 1.95\right] \qquad \text{(electrons);} \qquad (A1.19.a)$$

$$= \frac{n_e e^4}{8\pi m_e c^2}\left[2\ln\left(\frac{2m_e c^2}{I}\right) + 4\ln\gamma - 2\right] \qquad \text{(positrons).} \qquad (A1.19.b)$$

The dominant energy loss mechanism for high energy electrons is the production of electromagnetic radiation as a consequence of the accelerations the particles experience. This mechanism is called *bremsstrahlung* when it happens in a straight motion, *cyclotron* or *synchrotron* radiation when it happens in a non-relativistic or relativistic curve. For more details, see above, Sect. *A*1.2.

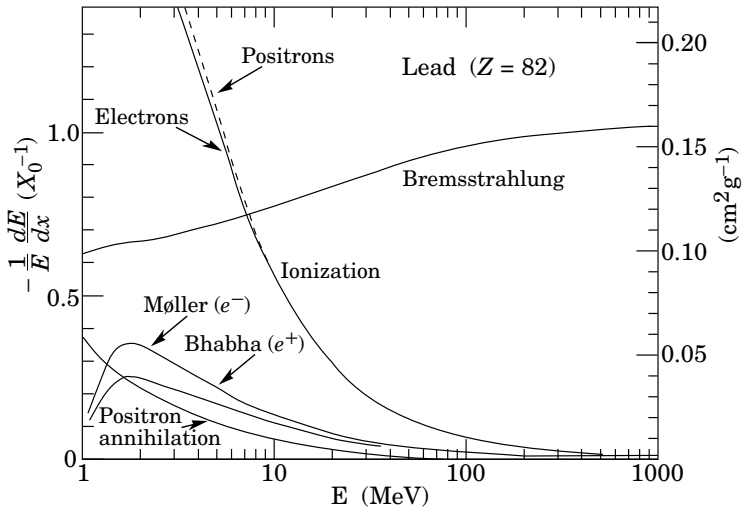

Fig. A1.4 - Fractional energy loss per radiation length in lead as a function of electron or positron energy [126].

A1.9 Multiple scattering

A charged particle traversing a medium will experience many small angle deflections due to various interactions, but mostly because of Coulomb scattering. The usual description of this behavior follows the theory of Molière: the angular distribution of scattered particles is roughly Gaussian, but with large tails, as at larger angles it behaves like Rutherford scattering.

In most cases it is sufficient to model the Gaussian part at smaller angles (comprising 98% of the projected distribution). Defining $\theta_0 = \theta^{\rm rms}_{\rm plane} = \theta^{\rm rms}_{\rm space}/\sqrt{2}$ we can fit the Molière

distribution with

$$\theta_0 = \frac{13.6 \text{ MeV}}{\beta cp} Z\sqrt{x/X_0}[1 + 0.038 \ln(x/X_0)] \qquad (A1.20)$$

where p, βc and Z are momentum, velocity and charge number of the scattered particle.

A1.10 Radiation length and critical energy

To describe electromagnetic interactions it is often convenient to deal with the behavior of an energetic electron with a given material in terms of its *radiation length*, X_0, defined as the mean distance over which a high energy electron loses $(1 - 1/e)$ of its energy due to bremsstrahlung. As an estimate, radiation length varies as

$$X_0 = \frac{716.4 \text{ g/cm}^2 A}{Z(Z+1)\ln(287/\sqrt{Z})} \qquad (A1.21)$$

and

$$X_0 \approx 180A/Z^2 \text{ g/cm}^{-2} \qquad (A1.22)$$

the values obtained by this last formula are accurate within 3% for atoms heavier than He. Values of X_0 for many materials are tabulated and can be retrieved easily (see for example [126]). Due to the intimate connection between bremsstrahlung and pair production (see Eq. $A1.16$ above), the mean distance a high energy photon covers before decaying in a electron-positron pair is $9/7 \cdot X_0$.

An electron loses energy due to bremsstrahlung at a rate roughly proportional to its energy, while ionization energy loss efficiency depends logarithmically to the energy: the energy at which the two loss rates are equal is called *critical energy*, E_c, and an useful approximation is

$$E_c = \frac{800 \text{ MeV}}{Z + 1.2} \qquad (A1.23)$$

A1.11 Electromagnetic cascades

When a high energy electromagnetic particle enters a thick medium, it initiates a process of particle multiplication, as both bremsstrahlung and pair production lead to an increase in the number N of electromagnetic particles. As the cascade evolves, the energy available for each particle decreases as $1/N$ down to the critical energy E_c. At this point ionization and excitations absorb energy without creating more particles and the shower has a typical exponential tail. Defining the scale variables $t = x/X_0$ and $y = E/E_c$ the longitudinal profile of the electromagnetic shower can be written as

$$\frac{dE}{dt} = E_0 b \frac{(bt)^{a-1} e^{-bt}}{\Gamma(a)} \qquad (A1.24)$$

where the maximum $t_{\max}$ occurs at $(a-1)/b$.

While the radiation length is the characteristic scale for the forward development of EM cascades, the lateral profile is described in terms of the *Molière radius*, R_M, defined as

$$R_M = X_0 \cdot \frac{21 \text{ MeV}}{E_c} \qquad (A1.25)$$

and

$$R_M \approx 7A/Z \text{ g/cm}^{-2} \qquad (A1.26)$$

On the average, only the 10% of the particles in the shower lie outside of a cylinder with radius R_M, and only 1% outside $3.5R_M$. The lateral distribution is usually parametrised as a sum of two gaussians, one giving the core and the other the tail, as:

$$f(r) = \frac{2rR^2}{(r^2+R^2)^2} \qquad (A1.27)$$

where $R = R(x/X_0, E)$.

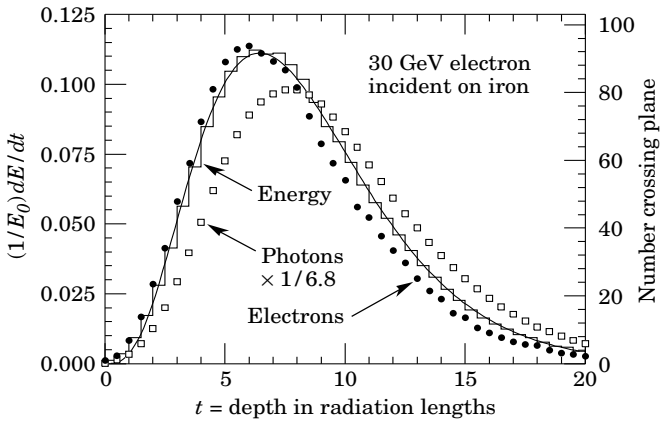

Fig. A1.5 - An EGS4 simulation of the fractional energy deposition per radiation length for a 30 GeV electron-induced cascade in iron [126].

Appendix A1

Appendix 2: The ferrous sulfate dosimeter

In this appendix a detailed description is given of the ferrous sulfate dosimeter we employed in the calibration of the ^{60}Co irradiator we used for total-dose characterization.

A2.1 Preparation of the ferrous sulfate dosimeter

The ferrous sulfate dosimeter, or Fricke dosimeter, consists of an aqueous solution ($1 \cdot 10^{-3} - 5 \cdot 10^{-3}$ M) of ferrous sulfate in 0.4 M sulfuric acid, containing 10^{-3} M NaCl and saturated with air.

Ionizing radiation acts on the water contained in this solution producing H^+ and OH^-; the OH radical then oxidize the ferrous iron to ferric. This process leads to a change in the optical thickness of the solution: comparing it to a reference (non-irradiated) sample, we obtain an estimate of the deposited energy and hence of the delivered dose. The ferrous sulfate dosimeter is discussed in depth in [127]; here we cover the most interesting issues regarding its preparation.

Various methods can be employed for the determination of $G(Fe^{3+})$, and since the 1960s the value has been conclusively established to be 15.5 – 15.6 ions/100 eV for a very wide range of energies (for γ rays and fast electrons). In literature it is shown that the value of $G(Fe^{3+})$ remains constant within 5% for X rays, γ rays and fast electrons in the range 0.03 – 30 MeV.

The oxygen present in the solution affects to a considerable extent the radiolytic transformations. In the absence of oxygen the value of $G(Fe^{3+})$ is found to be 1.9 times lower than in oxygen-containing solutions, due to the decrease in the rate of oxidation of the ferrous ions as the oxygen in the dosimetric system is consumed. This leads to an upper limit for the dose rate to avoid local consumption of oxygen in the irradiated solution; this upper limit is found to be about 10^8 rad/sec.

Organic admixtures affect the yield of Fe^{3+} production, in the sense that $G(Fe^{3+})$ increases sharply, depending on the nature and the structure of organic compounds. This is commonly explained in terms of organic compounds competing with ferrous ions for the OH radicals, producing organic radicals that in turn oxidize ferrous iron in a chain mechanism. This effect can be suppressed by adding chloride ions of the dosimetric solution, as the reaction of Cl^- with OH radicals is much faster than that of organic substances, producing Cl that will oxidize one Fe^{2+} ion the same way as the OH radical would have done and thus not changing the reaction rate. The distilled water available for laboratory use contains traces of organic compounds; it was shown that 10^{-3} M NaCl added to the water suppress the organic admixtures effects within experimental errors. NaCl concentration should not in any case exceed 10^{-2} M to avoid catalytic effects.

$G(Fe^{3+})$ is found to be poorly sensitive to the reagent concentration: the reaction yield is found to be independent on the concentration of ferrous sulfate in the range 10^{-4} – 10^{-2} M. $G(Fe^{3+})$ decreases slightly at higher pH values, but it is fairly constant if H_2SO_4 is added to the dosimetric solution with a concentration within 0.05 and 2.5 M; the commonly employed value is 0.4 M, as proposed in [127].

For the calibration of the ^{60}Co irradiator of the CNR-ISOF laboratory in Legnaro we prepared a standard solution: 11 ml of H_2SO_4 (96% solution), 38 mg of NaCl and 0.22 g of $FeSO_4 \cdot H_2O$ were diluited in 500 ml of bi-distilled water.

Appendix A2

Appendix 3: The SIRAD facility

In this appendix the SIRAD irradiation facility of the Tandem-XTU accelerator at the INFN National laboratories of Legnaro is presented. A more detailed description of the facility can be found in [128], [129].

A3.1 The Tandem accelerator

The Tandem-XTU is an electrostatic Van de Graaff accelerator. The principle at the basis of such an accelerator is shown in Fig. *A*3.1. An ion, emitted from a low energy ion source wherein it is made to pass through a low-electronegativity material such as Cs and acquires an electron, enters the Tandem attracted by the positive Tandem terminal, placed at some high voltage $+V$ (several MV). The ion reaches the terminal where passes through a thin carbon foil with a kinetic energy of $E = q \cdot \Delta V = +V$. In passing through the foil several outer electrons of the ion are stripped away. The ion, having now a charge $+Q$, is repelled by the tandem terminal, and is further accelerated until it leaves the accelerator towards the momentum analyzing magnet and the beam lines.

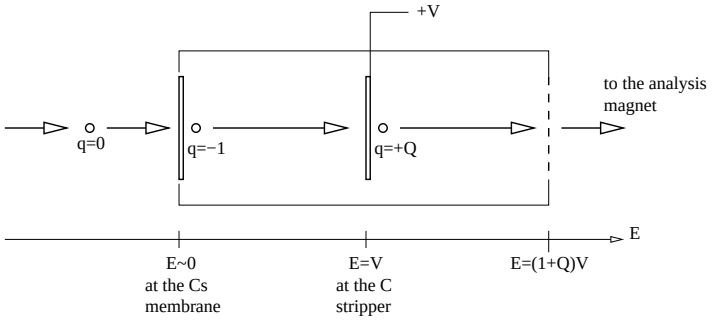

Fig. A3.1 - Schematic of a Van de Graaff accelerator.

The actual configuration of the Tandem-XTU at LNL is shown in Fig. *A*3.2. The ions are obtained ejecting atoms from a lump of the chosen material by means of an electron beam; such ions are then routed into the accelerating cavity. The main difference from the simple schematic in Fig. *A*3.1 is the possibility of adding a second C stripper to increase the ion charge in the final part in order to obtain higher energies. The energy in MeV at the exit of the Tandem is

$$E = E_{\text{in}} + V \times (1 + q_1 \times f + q_2 \times (1 - f)) \qquad (A3.1)$$

where $E_{\text{in}} = 180$ keV is the energy the ion has when it is injected into the Tandem, q_1 and q_2 are the (positive) charges the ion has after the first and second stripper respectively and $f = 0.25$ is the aspect ratio of the stripper acceleration stages. Typical values for the Tandem power V are comprised in the range 11–15 MV. Notice that if the second stripper is not used the formula simplifies into

$$E = E_{\text{in}} + V \times (1 + q_1) \qquad (A3.2)$$

The output ion beam is not monochromatic due to the stochastic fluctuations in the charge states after each stripper. Magnetic momentum analysis is needed to select one particular ion energy; this means that the Tandem operator can change the energy of the

ions delivered to the experimental beam lines simply changing the settings of the analysis magnet.

After the analysis magnet a switching magnet services 3 experimental rooms and 10 beam lines.

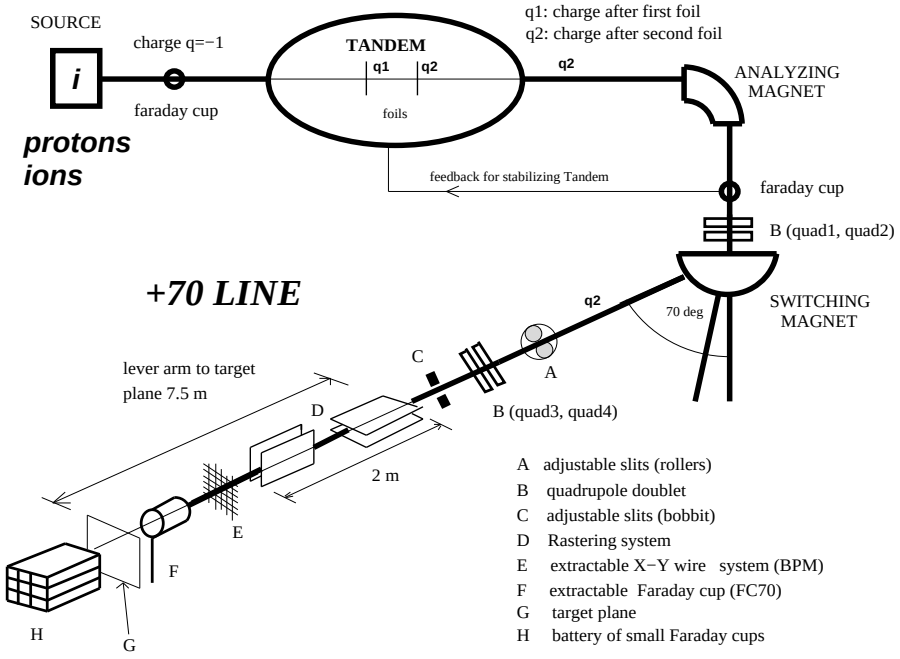

Fig. A3.2 - Schematics of the 15 MV Tandem-XTU at LNL and of the $+70^\circ$ beam line where SIRAD is placed.

A3.2 The SIRAD facility

The SIRAD beam line is located in Experimental Room 1: the heavy shield walls and ceiling allow the use of light ions and protons. The angle the switching magnet has to bend ions to send them down the SIRAD beam line is 70°; this means that a strong limitation on the available ion energies is given by their rigidity, as the magnetic field intensity our bending magnet can provide times the available curvature radius ρ must be greater than the ions' rigidity R:

$$B \cdot \rho = \frac{p}{Q_2 \times 300} = \frac{K}{Q_2 \times 300}\sqrt{\frac{1 + 2 \times A \times 931.5}{K}} \geq R \qquad (A3.3)$$

where p is the ion momentum in MeV/c, K its kinetic energy in MeV, Q_2 the ion charge as it exits the Tandem and 1 amu = 931.5 MeV. The maximum theoretical rigidity at the SIRAD beam line is $\sim$ 1.5 T·m, but we usually consider ions with less than 1.3—1.4 T·m. A list of commonly available ion beams is given in Tab. *A*3.1 for the Tandem operated at 14 MV with both strippers. Other configurations can be used and the corresponding ion energies can be calculated with the `beam` program, the same the Tandem operators use to set the analyzing magnet.

Irradiations are performed in vacuum (better than 8×10^{-6} mbar) to take full advantage of the beam energy. The motor controlled sample holder is 33 cm × 10 cm. The radius

of the beam spot is 3–4 mm when focused; when the beam is defocused the irradiated area beam diagnostics. When heavy ions and low fluxes are used the ion beam is strongly defocused and diodes are placed upstream of the irradiation area to monitor on-line the uniformity; in these conditions the irradiation area is 2×2 cm^2. When high fluxes are used with light ions (i.e. greater than $\sim 10^8/(\text{cm}^2 \cdot \text{s})$ a Faraday cup matrix is placed behind the DUT and the irradiation area can be as wide as 5×5 cm^2. When the beam is focused the use of an electric rastering system ensures that, even in the 5×5 cm^2 setting, the irradiation uniformity can be better than 5%.

Ion Species	Energy (MeV)	q1	q2	Range in Si (μm)	Surface LET in Si (MeV×cm^2/mg)
^{1}H	28.18	1	1	4390	0.02
^{7}Li	56.18	3	3	378	0.37
^{11}B	80.68	4	5	195	1.01
^{12}C	94.68	5	6	171	1.49
^{16}O	108.68	6	7	109	2.85
^{19}F	122.68	7	8	99.3	3.67
^{28}Si	157.68	8	11	61.5	8.59
^{32}S	171.68	9	12	54.4	10.1
^{35}Cl	171.68	9	12	49.1	12.5
^{48}Ti	196.18	10	14	39.3	19.8
^{51}V	196.18	10	14	37.1	21.4
^{58}Ni	220.68	11	16	33.7	28.4
^{63}Cu	220.68	11	16	33.0	30.5
^{74}Ge	231.18	11	17	31.8	35.1
^{79}Br	241.68	11	18	31.3	38.6
^{107}Ag	266.18	12	20	27.6	54.7
^{127}I	276.68	12	21	27.9	61.8
^{197}Au	275.68	13	26	23.4	81.7

Tab. A3.1 - Standard ion beams available at SIRAD; Tandem is set to use two strippers.

The Tandem current is stabilized with a feedback from the analyzed beam current: in principle the higher the current the better the stability. The limitations on the available currents are placed by radioprotection constraints: lighter ions and protons in particular can overcome the Coulomb barrier and produce nuclear reactions, thus activating the materials and producing unstable isotopes with half-lives of a few hours/days.

A3.3 Beam diagnostics and DAQ

As mentioned in the last section, two distinct beam diagnostic methods can be used.

In the case of heavy ions irradiations for SEE studies low fluxes are used (less than $10^5 - 10^6/(\text{cm}^2 \cdot \text{s})$ depending on the ion LET) and silicon PIN diodes can be used to count the impinging ions. A schematic of the irradiation procedure is shown in Fig. *A*3.3: after the selected beam is set, the mobile diodes are placed in the irradiation window, and the beam uniformity is calculated. Moreover, the beam intensity in the irradiation window (2×2 cm^2) is obtained as a linear combination of the readings on the outer, fixed diodes;

the obtained coefficients are recorded. Then, the beam is intercepted, the sample holder is shifted upwards and the DUT is placed in the irradiation window. The beam is enabled and the irradiation begins: the flux on the DUT is calculated from the readings of the four upstream diodes.

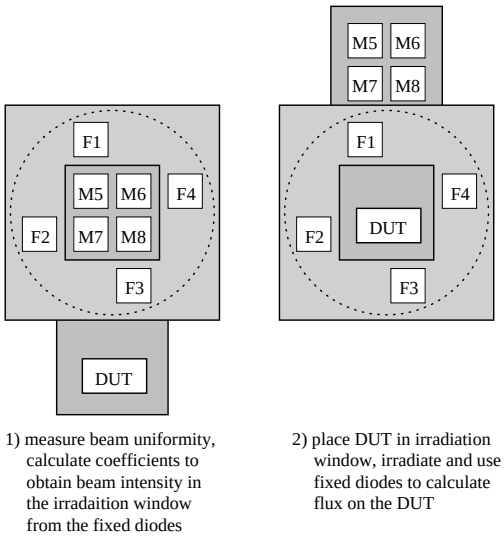

Fig. A3.3 - Beam diagnostic with the fixed and mobile diodes; dotted circle shows the beam area.

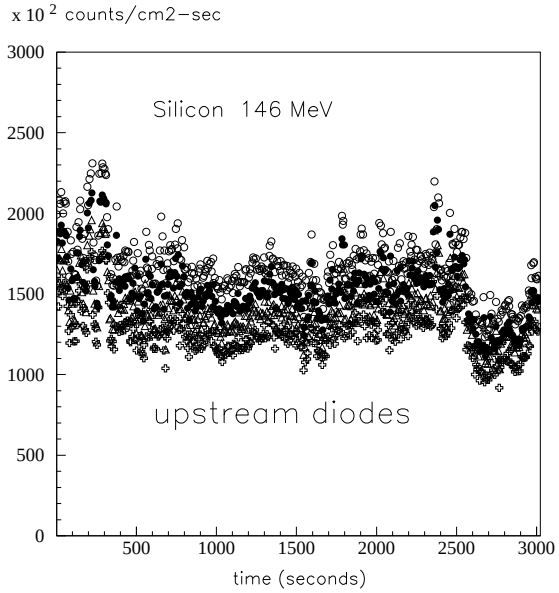

Fig. A3.4 - Typical flux measurement on the four upstream diodes.

Both the diode groups are read out simultaneously by a custom electronic module in which signals are amplified, shaped and discriminated. The threshold usually employed corresponds to an energy loss of 4 MeV in a 300 μm thick Si sample; the electronic chain is linear up to $\sim$ 500 MeV. The shaping time is of the order of 5 μs, allowing for count rates up to 50 kHz. Given the diode dimensions (square, side of $\sim 4-5$ mm) the allowed fluxes are higher, up to $2 \times 10^5/(\mathrm{cm}^2 \cdot \mathrm{s})$. An example of the recorded data for the fixed diodes is shown in Fig *A*3.4.

In the case of light ion irradiation for total dose or displacement damage studies the plaque mounting the fixed diodes is removed: the diodes cannot withstand the delivered dose without being compromised. By using the beam rastering system the irradiated area is now 5×5 cm^2. To monitor the irradiation a set of 3×3 Faraday cups is placed behind the DUT; a sample acquisition is shown in Fig. *A*3.5. For a standard *H* irradiation the proton range in silicon is $\sim$ 4.4 mm (see Tab. *A*3.1) and neglecting the sample holder behind the DUT the energy loss in Si is $\sim 1-2$ MeV in 300 μm. This means that protons pass the DUT and reach the Faraday cup system, allowing a precise measurement of the beam intensity and uniformity. Even in the case of thick DUTs/holders, with some care an arrangement in which at least one cup is not covered can be envisaged so that the beam can be monitored.

Each Faraday cup in this system is read out by grounding it through 100 MΩ resistors and measuring the voltage drop across the resistor with HP34401A digital multimeters, with a sensitivity of 10 pA. A current preamplifier stage can increase the sensitivity to 100 fA with an RMS noise of 25 fA.

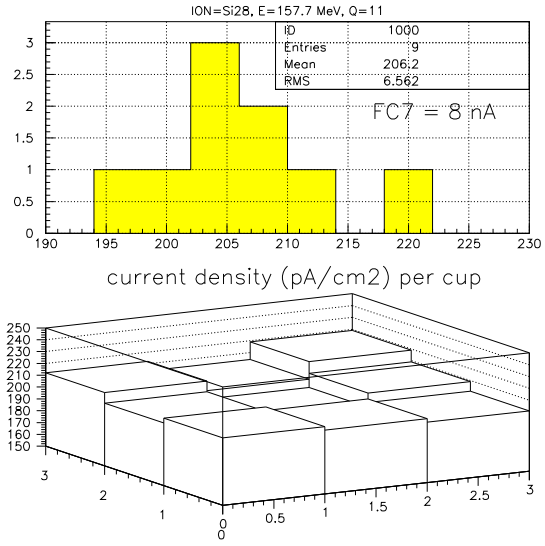

Fig. A3.5 - Current density distribution on the 9 Faraday cups downstream the sample holder; in this case the beam uniformity is $\sim 3\%$.

Appendix A3

Appendix 4: List of Acronyms

ACD	AntiCoincidence Detector
ACT	Air Čerenkov Telescope
AEM	ACD Electronic Module
AGN	Active Galactic Nucleus
ASIC	Application Specific Integrated Circuit
BEA	Base Electronics Assembly
CAL	Calorimeter
CME	Communication Error
COTS	Components Off-The-Shelf
CPU	Central Processing Unit
DAQ	Data Acquisition
EM	ElectroMagnetic (waves)
ESA	European Space Agency
ESD	ElectroStatic Discharge
FIFO	First In, First Out
FREE	ACD Front End Electronics
FWHM	Full Width at Half Maximum
GAFE	GLAST ACD Front-End
GARC	GLAST ACD Readout Control
GCCC	Glast Calorimeter Cable Controller
GCR	Galactic Cosmic Ray
GLEAM	GLAST LAT Event Analysis Machine
GLTC	Glast LVDS Translator Chip
GTCC	Glast Tracker Cable Controller
GTFE	Glast Tracker FrontEnd
GTRC	Glast Tracker Readout Control
GRB	Gamma Ray Burst
HPGe	High Purity Germanium
HVBS	High Voltage Bias Supply
INFN	(Italian) National Institute for Nuclear Physics
IR	InfraRed
KERMA	Kinetic Energy Released in Matter
LSB	Least Significant Bit
LVDS	Low Voltage Differential Signaling
MIP	Minimum Ionizing Particle
MSB	Most Significant Bit
OSS	(NASA) Office of Space Science
PD	PhotoDiode
PMT	PhotoMultiplier Tube
PSB	Power Supply Box
PSD	Pulse Shape Discrimination (technique)
RHA	Radiation Hardness Assurance
SAA	South Atlantic Anomaly
SEE	Single Event Effect

SEFI	Single Event Functionality Interrupt
SEGR	Single Event Gate Rupture
SEL	Single Event Latchup
SEU	Single Event Upset
SIU	Spacecraft interface Unit
SNR	SuperNova Remnant
SPE	Solar Particle Event
SSD	Single Sided Detector
SSR	Spacecraft Solid State Recorder
TEM	Tower Electronic Module
TOT	Time Over Threshold
TKR	Tracker
VLSI	Very Large Scale Integration
WSF	Wavelength Shifter Fiber

Bibliography

[♣]: SLAC GLAST Internal Notes can be accessed through the LATDocs document system, available online at

`http://www-glast.slac.stanford.edu/documents/LATDOCS.htm`

[♠]: Up-to-date NASA/GSFC/OSS GLAST documents can be found in the project Master Controlled Documents List and in the Science Resources list at

`http://glast.gsfc.nasa.gov`

[1]: GLAST Facilities Science Team, *GLAST Science Requirements Document - Final*, July 1999 [♠]

[2]: F. Pacini, *Rotating neutron stars, pulsars, supernovae remnants*, Nature 219, 1968, p.145

[3]: T. Gold, *Rotating neutron stars as the origin of the pulsating radio sources*, Nature 218, 1968, p. 731-732

[4]: F.C. Michel, H. Li, *Electrodynamics of neutron stars*, Phys. Rep. 318, 1999, p. 227-297

[5]: M.G. Baring, *High-Energy Emission from Pulsars: The Polar Cap Scenario*, Adv. Space Res. 33(4), 2004, p. 552-560, astro-ph/0308296

[6]: K.S. Cheng, *High-Energy Radiation from Pulsars: a Three-Dimensional Model Approach*, Adv. Space Res. 33(4), 2004, p. 561-570

[7]: D. J. Thompson et al., *Gamma Radiation from PSR B1055-52*, ApJ 516(1), May 1999, p. 297-306

[8]: J. Kataoka et al., *High-Energy Emission from the TeV Blazar Markarian 501 during Multi-wavelength Observations in 1996*, ApJ 514, March 1999, p. 138-147

[9]: G. Ghisellini, *Gamma Ray Bursts: Some Facts and Ideas*, invited talk at the 25th Johns Hopkins Workshop, Florence, Sep. 2001, astro-ph/0111584

[10]: T. Piran, *Gamma-Ray Bursts and the Fireball Model*, Phys. Rept. 314, 1999, p. 575-667, astro-ph/9810256

[11]: K.S. Cheng, T. Lu, *Gamma-Ray Bursts: Afterglows and Central Engines*, CJAA 1(1), Feb 2001, p. 1-20, astro-ph/0101147

[12]: P. Mészáros, *Theories of Gamma-Ray Bursts*, Annu. Rev. Astron. Astrophys. 40, 2002

[13]: B.L. Dingus, *Observation of the Highest Energy Gamma-Rays from GRBs*, AIP Conf. Proc. 558, 2001, p. 383

[14]: K. Koyama, R. Petre, E. V. Gotthelf, U. Hwang, M. Matsuura, M. Ozaki, S. S. Holt, *Evidence for shock acceleration of high-energy electrons in the supernova remnant SN1006*, Nature 378, Nov. 1995, p. 255

[15]: G.E. Allen, J.W. Keohane, E.V. Gotthelf, R. Petre, K. Jahoda, *Evidence of X-ray synchrotron emission from electrons accelerated to 40 TeV in the supernova remnant Cassiopeia A*, ApJ 487, Sept. 1997, p. L97-L100

[16]: S.D. Hunter et al., *EGRET observations of the diffuse gamma-ray emission from the galactic plane*, ApJ 481, May 1997, p. 205-240

[17]: M. Pohl, J.A. Esposito, *Electron acceleration in supernova remnants and diffuse gamma rays above 1 GeV*, ApJ 507, Nov. 1998, p. 327-338

[18]: F.A. Aharonian et al., *High-energy particle acceleration in the shell of a supernova remnant*, Nature 432, Nov. 2004, p. 75-77

[19]: J.F. Ormes, S. Digel, I.V. Moskalenko, A. Moiseev, R. Williamson, *The origin of cosmic rays: what can GLAST say?*, presented at "The Acceleration and Transport of Energetic Particles Observed in the Heliosphere", ACE-2000 Symposium

[20]: A. Morselli, *Dark Matter search with gamma rays: the experiments EGRET and GLAST*, Int. Journal of Modern Physics A17, 2002, p. 1829–1840

[21]: H.A. Mayer-Hasselwander et al., *High-energy gamma-ray emission from the Galactic Center*, Astron. Astrophys. 335, 1998, p. 161-172

[22]: L. Bergström, P. Ullio, J. Buckley, *Observability of gamma rays from dark matter neutralino annihilations in the Milky Way halo*, Astropart.Phys. 9, 1998, p. 137-162

[23]: S. Peirani, R. Mohayaee, J. A. de Freitas Pacheco, *Indirect search for dark matter: Prospects for GLAST*, Phys. Rev. D 70, Aug. 2004

[24]: M.F. Cawley, T.C. Weeks, *Instrumentation for Very High Energy Gamma-Ray Astronomy*, Exper. Astr. 6, 1995, p. 7-42

[25]: T.C.Weeks et al., *Observation of TeV gamma rays from the Crab nebula using the atmospheric Cerenkov imaging technique*, APJ 342, Jul. 1989, p. 379-395

[26]: S. M. Derdeyn, C. H. Ehrmann, C. E. Fichtel, D. A. Kniffen, R. W. Ross, *SAS-B digitized spark chamber gamma ray telescope*, Nucl. Instr. Meth. 98(3), Feb. 1972, p 557-566

[27]: W.L. Kraushaar, G.W.Clark, G.P.Garmire, R. Borken, P. Higbie, C. Leong, T. Thorsos, *High-Energy Cosmic Gamma-Ray Observations from the OSO-3 Satellite*, ApJ 177(2), Oct. 1972, p. 341-363

[28]: C.E. Fichtel, R.C. Hartman, D.A. Kniffen, D.J. Thompson, G.F. Bignami, H. Ögelman, M.E. Özel, T. Tümer, *High-energy gamma-ray results from the second small astronomy satellite*, ApJ 198, May 1975, p. 163-182

[29]: G. Bignami, G. Boella, J.J. Burger, B.G. Taylor, P. Keirle, J.A. Paul, H.A. Mayer-Hasselwander, E. Pfeffermann, L. Scarsi, B.N. Swanenburg, *The COS-B experiment for gamma-ray astronomy*, Space Sci. Instr., 1, Aug. 1975, p. 245-268

[30]: K. Bennett, *COS-B: the highlights*, Nucl. Phys. B 14B (Proc. Suppl.), 1990, p. 23–34

[31]: B.N. Swanenburg et al., *Second COS-B Catalog of High-Energy Gamma-Ray Sources*, ApJ 234, Jan. 1981, p. L69-L73

[32]: I.A. Grenier, W. Hermsen, J. Clear, *High energy gamma rays from the VELA pulsar – long-term variability and energy distribution*, Astron. Astroph. 204, Oct. 1988, p. 117–132

[33]: The NASA's HEASARC COS-B Archive, available online at `http://heasarc.gsfc.nasa.gov/docs/cosb/cosb.htm`

[34]: G. Kanbach, D.L. Bertsch, C.E. Fichtel, R.C. Hartman, S.D. Hunter, D.A. Kniffen, B.W. Hughlock, A. Favale, R. Hofstadter, E.B. Hughes, *The project EGRET (Energetic Gamma-Ray Experiment Telescope) on NASA's Gamma-Ray Observatory (GRO)*, Sp. Sci. Rev. 49, no. 1-2, 1988, p. 69-84

[35]: J.A. Esposito et al., *In-Flight Calibration of EGRET on the Compton Gamma-Ray Observatory*, ApJ Suppl. 123(1), Jul. 1999, p. 203-217

[36]: R.C. Hartman et al., *The Third EGRET Catalog of High-Energy Gamma-Ray Sources*, ApJ Suppl. 123, Jul. 1999, p. 79–202

[37]: NASA GRAPWG, *Report of the Gamma Ray Astronomy Program Working Group 1996-2010*, April 1997 [♠]

[38]: NASA Office of Space Science, *Gamma-Ray Large Area Space Telescope Flight Investigations*, AO 99-OSS-03, August 1999 [♠]

[39]: GLAST LAT Flight Investigation, *Response to AO 99-OSS-03*, November 1999 [♠]

[40]: *Recommended priorities for NASA's gamma-ray astronomy program*, GRAPWG committee final report, June 1999, `http://universe.gsfc.nasa.gov/grapwg.html` [♠]

[41]: G. Lichti, M.S. Briggs, R. Diehl, G.J. Fishman, R.M. Kippen, C. Kouveliotou, C.A. Meegan, W.S. Paciesas, R.S. Preece, V. Schoenfelder, A. von Kienlin, *GBM - a Gamma-Ray Burst Monitor for GLAST*, Proc. SPIE 4851, Mar. 2003, p. 1180-1187

[42]: D. A. Sheppard, A. Ruitberg, R. Hartman, R. Baker, G. Unger, *GLAST Large Area Telescope (LAT) Anti-Coincidence Detector (ACD)*, GLAST Technical Note, ACD-PROC-000051 [♣]

[43]: A. Moiseev et al., *Anticoincidence Detector for GLAST*, astro-ph/9912138

[44]: D.J. Thomson et al., *Calibration of the Energetic Gamma-Ray Experiment Telescope (EGRET) for the Compton Gamma-Ray Observatory*, ApJS 86, p. 629, 1993

[45]: W.N. Johnson, J.E. Grove, B.F. Phlips, J. Ampe, S. Singh, E. Ponslet, *The construction and performance of the CsI hodoscopic calorimeter for the GLAST beam test engineering module*, IEEE Trans. Nucl. Sci. 48(4) , Aug. 2001, p. 1182 – 1189

[46]: H. F.-W. Sadrozinski, *GLAST LAT Silicon Detector Specification*, GLAST Technical Note, LAT-DS-00011 [♣]

[47]: L. Latronico, *Quality control on the silicon sensors of the GLAST Tracker*, 6th International Conference on Large Scale Applications and Radiation Hardness of Semiconductor Detectors, Firenze, October 2003

[48]: D. Nelson and R. Johnson, *GLAST LAT Conceptual Design and Specification of the GTFE ASIC*, GLAST Technical Note, LAT-SS-00169 [♣]

[49]: R.P. Johnson, P. Poplevin, H. F.-W. Sadrozinski, E.N. Spencer, *An Amplifier-Discriminator Chip for the GLAST Silicon-Strip Tracker*, IEEE Trans. Nucl. Sci. 45 (3), June 1998 p.927-930

[50]: I. Kipnis et al., *A time-over-threshold machine: the readout integrated circuit for the BABAR Silicon Vertex Tracker*, IEEE Trans. Nucl. Sci. 44 (3), June 1997, p. 289-297

[51]: J. Antos et al., *The SVX II silicon vertex detector upgrade at CDF*, Nucl. Instr. Meth., A360, 1995, p. 118

[52]: J. Olsen, *GLAST LAT Conceptual Design of the Glast Tracker Readout Controller Electronics (GTRC) ASIC*, GLAST Technical Note, LAT-SS-00170 [♣]

[53]: L. Sapozhnikov, *GLAST Tracker Cable Controller ASIC, Specification and ICD*, GLAST Technical Note LAT-TD-01550 [♣]

[54]: L. Sapozhnikov, *GLAST Calorimeter Cable Controller ASIC ICD*, GLAST Technical Note LAT-TD-1549 [♣]

[55]: M. Freytag, O. Milgrome, *Specification and ICD, GLAST LVDS Translator Chip (GLTC3)*, GLAST Technical Note, LAT-TD-3742 [♣]

[56]: E.G. Stassinopoulos, J.P. Raymond, *The Space Radiation Environment for Electronics*, Proc. IEEE 76 (11), November 1988, p. 1423-1442

[57]: J.L Barth, C.S. Dyer, E.G. Stassinopoulos, *Space, atmospheric, and terrestrial radiation environments*, IEEE Trans. Nucl. Sci. 50(3), Jun 2003, p. 466-482

[58]: L.J. Gleeson, W.I. Axford, *Solar Modulation of Galactic Cosmic Rays*, ApJ 154, Dec. 1968, p. 1011–1026

[59]: M.S. Longair, *High Energy Astrophysics*, Cambridge University Press

[60]: K.R. Lang, *The Cambridge Encyclopedia of the Sun*, Cambridge University Press, 2001

[61]: B.F. James, O.W. Norton, M.B. Alexander, *The Natural Space Environment: Effects on Spacecraft*, NASA Reference Publication 1350

[62]: J.I. Vette, *The space radiation environment*, IEEE Trans. Nucl. Sci. 12, Oct. 1965, p. 1-17

[63]: D.M. Sawyer, J.I. Vette, *AP-8 trapped proton environment for solar maximum and solar minimum*, NASA/GSFC, NSSDC/ WDC-A-R&S, 76-06, Dec. 1976

[64]: J.I. Vette, *The AE-8 trapped electron model environment*, NASA/GSFC, NSSDC/ WDC-A-R&S, 91-24, Nov. 1991

[65]: M.S. Gussenhoven, E.G. Mullen, D.H. Brautigan, *Improved understanding of the Earth's radiation belts from the CRRES satellite*, IEEE Trans. Nucl. Sci. 43, Apr. 1996, p. 353-368

[66]: European Cooperation for Space Standardization (ECSS), *System Engineering: Space Environment*, standard E-10-04A, ESA publications, Jan 2000

[67]: A.J. Tylka, J.H. Adams, Jr., P.R. Boberg, B. Brownstein, W.F. Dietrich, E.O. Flueckiger, E.L. Petersen, M.A. Shea, D.F. Smart, E. C. Smith, *CREME96: A Revision of the Cosmic Ray Effects on Micro-Electronics Code*, IEEE Transactions on Nuclear Science, 44, 1997, p. 2150-2160

[68]: J.H. Adams, *Cosmic Ray Effects on Microelectronics, Part IV*, NRL Memorandum Report 5901, Naval Research Laboratory, 1986

[69]: P. Michelson and N. Gehrels, *GLAST System Specifications*, 433-SPEC-001 [♠]

[70]: S. Verma, *High-energy electrons and emission of the omnidirectional synchrotron radiation in radio frequency and x-ray regions*, Astronomical Journal 72, Sep. 1967, p. 834–883

[71]: E.C. Ray, *Re-Entrant Cosmic-Ray Albedo*, Journal of Geophysical Research 67, Aug. 1962, p. 3289

[72]: S.C.C. Ting, *The Alpha Magnetic Spectrometer (AMS)*, Proceedings of the Symposium "Highlights in X-ray Astronomy", MPE report 272, 1999, p. 120–126

[73]: S.W. Barwick, *The energy spectra and relative abundances of electrons and positrons in the galactic cosmic radiation*, ApJ 498, May 1998, p. 779–789

[74]: GLAST Science Instrument - Spacecraft Interface Requirements Document, SI-SC IRD [♠]

[75]: A. Holmes-Siedle, L. Adams, *Handbook of Radiation Effects*, Oxford university Press, 1993

[76]: V.A.J. Van Lint, *Mechanisms of Radiation Effects in Electronic Materials*, Wiley and Sons, 1980

[77]: Y. Shi et al., *A Numerical Study of Cluster Center Formation in Neutron Irradiated Silicon*, Journal of Applied Physics 67(I), 1990

[78]: S. Yoshida et al., *Heavy Ion Irradiation on Silicon Strip Sensors for GLAST*, IEEE Trans. Nucl. Sci. 49(4), Aug. 2002 p. 1756-1762

[79]: J.M. Benedetto, H.E. Boesch, *The relationship between ^{60}Co and 10 keV X-ray damage in MOS devices*, IEEE Trans. Nucl. Sci. NS-33, Dec. 1986, p. 1318-1323

[80]: T.P. Ma et al., *Ionizing radiation Effects in Electronic materials*, Wiley & Sons, 1980

[81]: T.R. Oldham, *Ionizing radiation Effects in MOS Oxides*, World Scientific, 1999

[82]: E.L. Petersen, J.C. Pickel, J,H, Adams, E.C. Smith, *Rate Prediction for Single Event Effects – a Critique*, IEEE Trans. Nucl. Sci,. 39 (6), December 1988, p. 1577-1599

[83]: P.E. Dodd, L.W. Massengil, *Basic mechanisms and modeling of single-event upsets*, IEEE. Trans. Nucl. Sci. 50(3), Jun. 2003, p. 583-602

[84]: S.-W. Fu, A.M. Mohsen, T.C. May, *Alpha-particle induced charge collection measurements and the effectiveness of a novel p-well protection barrier on VLSI memories*, IEEE Trans. Electron. Devices 32, Feb. 1995, p. 49-54

[85]: O. Musseau, *Single event effects in SOI technologies and devices*, IEEE Trans. Nucl. Sci. 43, Feb. 1996, p. 603-613

[86]: L.R. Rockett, *An SEU-hardened CMOS Data Latch Design*, IEEE Trans. Nucl. Sci. 35 (6), December 1988, p. 1682-1687

[87]: R. Koga, S.H. Penzin, K.B. Crawford, W.R. Crain, *Single event functional interrupt (SEFI) sensitivity in microcircuits*, Proceedings of the 4th RADECS conference, 1997, p. 311-318

[88]: A.H. Johnston, B.W. Hughlock, *Latchup in CMOS from single particles*, IEEE Trans. Nucl. Sci. 37, 1990, p. 1886-1893

[89]: F. Sexton, *Destructive single-event effects in semiconductor devices and ICs*, IEEE Trans. Nucl. Sci. 50(3), Jun. 2003, p. 603-621

[90]: L.S. Smith, D.K. Nichols, J.R. Cross, W.E. Price, *Temperature and Epi Thickness Dependence of the Heavy Ion Induced Latchup Threshold for a CMOS/EPI 16k Static RAM*, IEEE Trans. Nucl. Sci. 34 (6) , December 1987, p. 1800-1802

[91]: J.V. Osborn, D.C. Mayer, R.C. Lacoe, S.C. Moss and S.D. La Lumondiere, *Single Event Latchup Characteristics of Three Commercial CMOS Processes*, Proceedings of the 7th NASA Symposium on VLSI Design, 1998

[92]: D.M. Fleetwood, *Total dose radiation hardness assurance*, IEEE Trans. Nucl. Sci. 50(3), Jun. 2003, p. 552-564

[93]: Standard guide for ionizing radiation (total dose) effects testing of semiconductor devices, American Society for Testing and Materials (ASTM) guide F1892-98, Nov. 1998

[94]: Test method standard: microcircuits, US Dept. of Defense military standard MIL-STD-883E, 1994

[95]: K. Kerris, S.G. Gorbics, *Experimental determination of the low-energy spectral component of Co-60 sources*, IEEE Trans. Nucl. Sci. 32, 1985, p. 4356

[96]: T.C Zietlow, *Dose enhancement effects in a Sheperd model 81-22 Cobalt-60 irradiatior*, IEEE Trans. Nucl. Sci. 34(3), Jun. 1987, p. 662–666

[97]: J. H. Hubbell and S. M. Seltzer, *Tables of X-Ray Mass Attenuation Coefficients and Mass Energy-Absorption Coefficients*, NISTIR 5632. Available online: http://physics.nist.gov/xaamdi

[98]: H. Fricke and S. Morse, *The chemical action of roentgen rays on dilute ferrosulphate solutions as a measure of dose*, Am. J. Roent. Rad. Th., Vol. 18, Pag. 430-2, 1927

[99]: R. Rando, A. Bangert, D. Bisello, A. Candelori, P. Giubilato, M. Hirayama, R. Johnson, H. F.-W. Sadrozinski, M. Sugizaki, J. Wyss, M. Ziegler, *Radiation Testing of GLAST LAT Tracker ASICs*, IEEE Trans. Nucl. Sci. 51(3), June 2004, p. 1067 - 1073

[100]: R. Rando, H. Sadrozinski, *Radiation Tests of GLAST LAT Electronic Components at LNL*, GLAST Technical Note, LAT-PS-01059 [♣]

[101]: R. Rando, H. Sadrozinski, *Radiation Test Plan for the GLAST LAT TKR ASICs*, GLAST Technical Note, LAT-PS-01325 [♣]

[102]: E.J. Daly, A.Hilgers, G. Drolshagen, H.D.R. Evans, *Space Environment Analysis: Experience and Trends*, ESA 1996 Symposium on Environment Modeling for Space-based Applications, Sept. 18-20, 1996

[103]: M. Sugizaki, M. Hirayama, R. P. Johnson, H. F.-W. Sadrozinski, L. Latronoco, N. Lumb, G. Spandre, J. Wyss, A. Kaminsky, I. Stavitski, *SEE test of the LAT Tracker Front End ASIC*, GLAST Technical Note, LAT-TD-00333 [♣]

[104]: Texas A&M University Cyclotron Institute, MS #3366, College Station TX 77843-3366, online at `http://cyclotron.tamu.edu`

[105]: T. Handa, T. Oshugi, H. F.-W. Sadrozinski, A. Brez, *Results from the testing of the GLAST LAT SSD prototypes*, GLAST Technical Note, LAT-TD-00086 [♣]

[106]: S. Yoshida, K. Yamanaka, T. Ohsugi, H. Masuda, T. Mizuno, Y. Fukazawa, Y. Iwata, T. Murakami, H. F.-W. Sadrozinski, K. Yamamura, K. Yamamoto, K. Sato, *Heavy Ion Irradiation on Silicon Strip Sensors for GLAST*, IEEE Trans. Nucl. Sci. 49(4), Aug. 2002, p. 1756–1762

[107]: R. Rando, L. Sapozhnikov, A, Bangert, H. F.-W. Sadrozinski, *Results from the Legnaro SEE Test of LAT DAQ Flight ASICs*, GLAST Technical Note, LAT-TD-2498 [♣]

[108]: R. Rando, H. F.-W. Sadrozinski, *TID Radiation Test Plan for the GLAST LAT DAQ ASICs*, GLAST Technical Note, LAT-TD-4677 [♣]

[109]: R. Rando, H. F.-W. Sadrozinski, L. Sapozhnikov, *Results from the September 2004 TID Tests of LAT DAQ Flight GTCC & GCCC at LNL*, GLAST Technical Note, LAT-TD-05188 [♣]

[110]: M. Auric, H. F.-W. Sadrozinski, *TID tests of 3 MAXIM DC-DC converters*, GLAST Technical Note, LAT-TD-02225 [♣]

[111]: R. Rando, H. F.-W. Sadrozinski, Jozsef Ludvig, *Latch-up Test of 3 MAXIM DC-DC Converters*, GLAST Technical Note, LAT-TD-02234 [♣]

[112]: T. Burnett, *LAT Reconstruction (and simulation)*, presented at the GLAST Users Committee (GUC) Meeting, 23 Oct. 2003, see the GUC resources in the SSC section at [♠]

[113]: W.B. Atwood, *GISMO: An Object-Oriented Program for High-Energy Physics Event Simulation and Reconstruction*, Int. Journal of Mod. Phys. C3, p. 459

[114]: W.R. Nelson, H.Hirayama, D.W.O. Rodgers, *The EGS4 Code System*, Tech. Report 265, SLAC & Stanford University, 1985

[115]: H.C. Fesefeldt, *Simulation of hadronic showers, physics ans applicaions*, GHEISHA program, Technical Report PITHA 05-02, RWTH Aachen Physikzentrum, 1985

[116]: R. Frühwirth, *Application of Kalman filtering to track and vertex fitting*, Nucl. instr. Meth. A262, p. 444–450

[117]: P.Boinee et al., *Gleam: the GLAST Large Area Telescope simulation framework*, in *Science with the New Generation of High Energy Gamma-ray Experiments. Between Astrophysics and Astroparticle Physics*, 2003, eds. S. Ciprini, A. De Angelis, P. Lubrano, O. Mansutti, Forum Editrice Universitaria, Udine, *astro-ph/0308120*

[118]: S. Agostinelli et al., *GEANT4 - a simulation toolkit*, Nucl. Instr. Meth. A 506(3), Jul. 2003, P. 250–303

[119]: M. Brigida, F. Gargano, N. Giglietto, F. Loparco, M. N. Mazziotta, *Signal simulation in Silicon Strip Detectors and Digit package development*, GLAST Technical Note, LAT-TD-1058 [♣]

[120]: The SLAB code for G4 validation, `http://sirad.pd.infn.it/glast/ground_sw/slabs.html`

[121]: C. J. Crannell, H. Crannell, R. R. Whitney, and H. D. Zeman, *Electron-Induced Cascade Showers in Water and Aluminum*, Phys. Rev. 184(2), 1969, p. 426–431

[122]: L. Breiman, J. Freidman, R. Olshen, C. Stone, *Classification and regression trees*, Wadsworth, 1984

[123]: R Development Core Team, *R: A language and environment for statistical computing*, ISBN 3-900051-00-3, R Foundation for Statistical Computing, online: `http://www.R-project.org`

[124]: P. Dalgaard, *Introductory statistics with R*, Springer, 2002

[125]: T. Therneau, B. Atkinson, *rpart3 for S-Plus 6.0*, S-Plus extensions, Mayo Foundation for Medical Education and Research, Division of Biostatistics, online : `http://www.mayo.edu/hsr/Sfunc.html`

[126]: K. Hagiwara et al., *Particle Data Book*, Phys. Rev. D 66, 010001 (2002)

[127]: I.V. Vereshchinskii, A.K. Pikaev, *Introduction to Radiation Chemistry*, Israel Program for Scientific Translations, 1964

[128]: J. Wyss, D. Bisello, D. Pantano, *SIRAD: an irradiation facility at the LNL Tandem accelerator for radiation damage studies on semiconductor detectors and electronic devices and systems*, Nucl. Instr. Meth. A 462, 2001, p. 426-434

[129]: D.Bisello, A. Candelori, P. Giubilato, A. Kaminski, D. Pantano, R. Rando, M. Tessaro, J. Wyss, *The SIRAD irradiation facility for radiation damage studies induced by high energy ions*, Rad. Phys. Chem. 71, 2004, p. 717-719

Index